Northumbria Research Link

Citation: Marquez Prieto, Jose (2016) Development of Cu2ZnSnSe4 and Cu2SnS3 based absorbers by PVD processes. Doctoral thesis, Northumbria University.

DEVELOPMENT OF $Cu_2ZnSnSe_4$ and Cu_2SnS_3 BASED ABSORBERS BY PVD PROCESSES

J MÁRQUEZ PRIETO

PhD

2016

Development of $Cu_2ZnSnSe_4$ and Cu_2SnS_3 Based Absorbers by PVD Processes

J Márquez Prieto

A thesis submitted in partial fulfilment of the
requirements of the University of Northumbria
at Newcastle for the degree of Doctor of
Philosophy

Research undertaken in the Faculty of
Engineering and Environment

April 2016

Abstract

Kesterite thin film solar cells are one of the most promising technologies for the future thin film PV market. The term “kesterite” refers to the crystal structure that the $Cu_2ZnSn(S,Se)_4$ compound adopts.

This thesis discusses the study of the formation of the pure selenide of the kesterite compound $Cu_2ZnSnSe_4$ (CZTSe) as an absorber layer. The layers were produced by a 2-stage physical vapour deposition (PVD) of Cu-Zn-Sn precursor films by sputtering followed by a reactive conversion step in the presence of Se. Solar cells have been fabricated with the absorbers produced.

The research explored the evolution of phases during the formation of CZTSe and the influence of the absorber composition on its optical and microstructural properties. In addition, the work involved: optimisation of the CZTSe synthesis process, studying the influence of the Se source, the role of temperature of the conversion process, the role of ramping rate and the ambient pressure, and the role of these for maximising device performance.

From the study of the evolution of phases it was concluded that CZTSe can be formed from Cu-Zn-Sn precursors over a wide range of temperatures (380-550 ^{o}C). The formation of the ternary compound Cu_2SnSe_3 (CTSe) from Cu-Sn precursors using the same synthesis approach was also demonstrated. Whilst this material was considered unsuitable as a solar PV absorber layer due to its low bandgap, the pure sulphide ternary phase Cu_2SnS_3 (CTS) was considered more suitable and was synthesised using a single step co-evaporation PVD method. A device with an efficiency of 1.8% demonstrated the possibility of using this earth abundant compound for thin film PV.

A combination of X-ray diffraction and Raman spectroscopy studies demonstrated that CZTSe films with very Cu-poor and Zn-rich compositions led to a high population of the beneficial V_{Cu} + Zn_{Cu} defect clusters, and CZTSe phase domains with a less disordered kesterite type structure. This led to devices with efficiencies over 8% and V_{OC} values greater than those of the current world record CZTSe solar cells. The research of this thesis provides a combination of practical and fundamental knowledge that could become a key towards minimising the efficiency gap between kesterites and their commercialised chalcogenide predecessors: CdTe and $Cu(In,Ga)Se_2$.

Contents

Acknowledgements

The work of this thesis has been possible thanks to funding from the 7th Framework programme of the European Commission (FP7/2007-2013), with a Marie Curie Fellowship within the Initial Training Network (ITN) project "KESTCELLS" under grant agreement nº316488.

The last three years of learning and research have been wholly enjoyable. I cannot imagine a better learning and training opportunity than the KESTCELLS project, which it has been a pleasure of being part of. During this project I have received the invaluable help of several people and I would like to express my gratitude to them.

First and foremost, I owe my deepest gratitude to my principal supervisor Assoc. Prof. Ian Forbes for selecting me to develop this work. He deserves significantly more gratitude that what I could describe in these lines for his guidance and constant support in this project and also in life.

I am also extremely grateful to my supervisor Prof. Nicola Pearsall who has been always available for any help that I have required. I had the pleasure to enjoy her supervision which it has been full of support, serenity, efficiency and wisdom. I am also very thankful for all the time that she put in reading and correcting my manuscripts, abstracts, presentations and in particular this thesis.

I would like to thank Dr. Pietro Maiello for all the lab training at Northumbria University and for his help in solving any technical issue that we faced in the lab. I also thank my colleagues Samantha and Mehrnoush for her company during the last year of this project.

I am very thankful to Dr. Yaroslav Romanyuk and Prof. Ayodhya Tiwari for accepting me in EMPA to do part of my research, where I developed my skills from their expertise in device understanding and processing. I also need to thank Melanie Werner, Carolin Sutter-Fella, Harald Hagendorfer and especially my colleague Stefan Haass for their help in the lab, fantastic discussions and friendship.

I would also like to thank Prof. Susan Schorr for receiving me in her group at the Helmholtz-Zentrum Berlin (HZB). This secondment gave me the opportunity of developing my skills in X-ray diffraction analysis. I am especially thankful to René Gunder and Dr. Galina Gurieva who spent several hours discussing and training me in data refinement and microstructural analysis. I am also very thankful to Elisa Valle Ríos for helping with measurements, data sharing, discussions, and for her happiness and friendship.

I am very thankful to Dr. Thomas Unold and his group members for accepting me during my secondment in HZB. I am especially thankful to Dr. Sergej Levcenko for sharing his expertise and knowledge helping with several measurements like EQE, Raman, PL, IV-T, C-V and many more. Many thanks go to Dr. Iver Lauermann and my friend Tetiana Olar who dedicated large amount of time in helping me to access the synchrotron radiation source BESSY II.

I would like to congratulate Dr. Edgardo Saucedo, Dr. Jose Miguel Sanjuan and Dr. Francisco Hernandez from IREC in Barcelona for an excellent coordination of the KESTCELLS project. In my opinion, it could not have been conducted in a better way. I would like to thank them for their help with any query that I have had during this project.

I need to express my gratitude again to Dr. Edgardo Saucedo and all the group members of the IREC's Solar Energy Materials and Systems Group for welcoming me in their lab for a couple of weeks, even if we were not very successful making CTS solar cells! I especially need to thank my friend Markus Neuschitzer who provided me with accommodation during this period. I had the pleasure of sharing several months of this project with him, full of great discussions, experiments and great fun! My gratitude also extends to Dr. Mirjana Dimitrievska and Dr. Victor Izquierdo for performing Raman measurements on my samples at IREC.

I am very thankful to Prof. Charlotte Platzer Björkman, Dr. Jonathan Scragg and my friend Yi Ren from the Ångström Solar Center at Uppsala University for performing XRF and Raman measurements on my samples and also for providing Molybdenum substrates for some of my experiments.

I had a fantastic time at the company NEXCIS in La Rousset thanks to Dr. Thomas Goislard for his help and supervision during my secondment with them. I am very thankful to Laura Vauche, Monika Arasimowicz, Dario Cozza and Lisa Risch for fruitful discussions and for the great time we had in Aix!

Furthermore, I would like to thank Assoc. Prof. David Lane from Cranfield University and Dr. Raquel Caballero from the Autonomous University of Madrid for accepting to be my examiners. Thank you very much for your time and consideration.

I would like to express my gratitude to the people I met in Newcastle for being fantastic and for making me enjoy my time in the North East including my great friends (Edu, Elena, Joaquín, Irene, Sera, Raúl, Tom, Charlie, Joe, Fab and Gemma), the Highbury 17 people (Uli, Matt, Tom, Laura and Claudia), and all my friends from the football team (NCLC)!

Last but not least, I would like to thank my sisters and especially my parents for their love and unconditional support.

Thank you very much.

List of abbreviations

AM 1.5	Air Mass 1.5 Solar Spectrum
AZO	Aluminium Doped Zinc Oxide
BBXRD	Bragg-Brentano X-ray Diffraction
CIGS	$Cu(In,Ga)Se_2$
CIS	$CuInSe_2$
CTS	Cu_2SnS_3
CTSe	Cu_2SnSe_3
CZT	Cu-Zn-Sn Precursor
CZTS	Cu_2ZnSnS_4
CZTSe	$Cu_2ZnSnSe_4$
CZTSSe	$Cu_2ZnSn(S,Se)_4$
EDX/EDS	Energy-dispersive X-ray Spectroscopy
Eff	Efficiency of a Solar Cell
EMPA	Swiss Federal Laboratories for Materials Science and Technology
EQE/IQE	External Quantum Efficiency/Internal Quantum Efficiency
FWHM	Full With at Half Maximum
GDOES	Glow Discharge Optical Emission Spectrometry
GIXRD	Grazing Incidence X-ray diffraction
HZB	Helmholtz Zentrum Berlin
ICP-MS	Inductively Coupled Plasma Mass Spectroscopy
ICSD	Inorganic Crystal Structure Database
IEA	International Energy Agency
IMEC	Interuniversity Microelectronics Centre
IRDEP	Institute of Research and Development on Photovoltaic Energy
IREC	Catalonia Institute for Energy Research
iZnO	Intrinsic Zinc Oxide
KIST	Korea Institute of Science and Technology
MIT	Massachusetts Institute of Technology
NREL	National Renewable Energy Laboratory
PL	Photoluminescence
PLE	Photoluminescence Excitation
PV	Photovoltaic

PVD	Physical Vapour Deposition
PVPS	Photovoltaic Power Systems Programme
QNR	Quasi Neutral Region
RF	Radio Frequency
RTP	Rapid Thermal Process/Processor
SCR	Space Charge Region
SEM	Scanning Electron Microscopy/Microscope
SLG	Soda Lime Glass
SRH	Shockley-Read-Hall
TCO	Transparent Conductive Oxide
XRD	X-ray Diffraction
XRF	X-ray Fluorescence

Declaration

I declare that the work contained in this thesis has not been submitted for any other award and that it is all my own work. I also confirm that this work fully acknowledges opinions, ideas and contributions from the work of others. The work was carried out within the frame of the KESTCELLS project funded by the 7th Framework of the European Commission under grant agreement nº316488.

I declare that the Word Count of this Thesis is 39763 words

Name: José A. Márquez Prieto

Signature:

Date: 7th August, 2016

1 Introduction

Solar PV is an elegant technology involving the conversion of sunlight into electricity using an electronic device called solar cell. It is also one of the fastest growing renewable energy technologies. It has been predicted that 0.4TW will have been deployed by the end of 2016 and this number is expected to increase by an order of magnitude by 2050.

The photovoltaic effect was discovered by Edmund Becquerel in 1839 [1]. In 1876, Adams and Day observed the photovoltaic effect in solidified selenium [2].The first solar cell using diffused junction Si based device was fabricated in the Bell laboratories in the 1954 [3].

According to the 2015 International Energy Agency (IEA) Photovoltaic Power Systems Programme (PVPS) report 1.1% of the world’s electricity was produced by PV systems and from 2010 to 2014 the installed capacity from PV increased from 40 to 180 GW [4]. With this data it is safe to say that the PV market is healthy and it is expected to keep on growing.

This thesis is focused on kesterites thin films and their potential to be used in photovoltaic systems. The compound studied in this thesis is $Cu_2ZnSnSe_4$ (CZTSe) derived from the natural compound $Cu_2Fe_{1-x}Zn_xSnS_4$ which crystallizes in the kesterite type structure and gives the name to the photovoltaic (PV) technology and research community. CZTSe, along with the compounds from its family such as the pure sulfide Cu_2ZnSnS_4 (CZTS) and the solid solution $Cu_2ZnSn(S,Se)_4$ (CZTSSe) have been developed in the last decade as an alternative compounds to cadmium telluride (CdTe) and copper indium gallium (di)selenide (CIGS) that are already commercialized [5].

1.1 Thin film solar cells: towards sustainable photovoltaics

Thin film photovoltaic devices use a light absorbing layer which is capable of absorbing a large number of photons in the solar spectrum with wavelengths shorter than near-infra red. These layers are just a few μm thick, in contrast to the classical Crystalline Si (c-Si) technology which needs material thicknesses of hundreds of microns due to its lower absorption coefficient (α) because of its indirect bandgap. This provides the thin film technologies with a great potential to reduce costs compared to c-Si. According to the MIT report “The Future of Solar Energy”, c-Si accounted for more than 90% of the global module production capacity in 2014 [6]. Some other advantages of thin film technologies such as CdTe or CIGS are their potential to be produced in flexible and light substrates such as polyamide [7, 8], and various metal foils [9]. Thin film technologies also require less energy to manufacture, which makes the fabrication a more sustainable process. In addition, the thin film technologies provide aesthetical alternatives for building integration in comparison to the classical commercialized c-Si based modules.

1.2 Kesterites as earth abundant thin film photovoltaics?

It has been commonly identified in many research articles that kesterite solar cells are semiconductors made out of earth abundant elements [10-13]. This is true for the pure sulphur variety of the kesterite compounds CZTS and also for the ternary Cu_2SnS_3 (CTS). However, Se-containing kesterite absorber layers have, in general, resulted in devices with greater efficiencies than those based on CZTS [14-16]. This led groups to produce devices with a high concentration of Se, therefore, it cannot be stated anymore that the absorber layers are fully fabricated out of earth abundant elements.

To make kesterite solar cells competitive at industrial level against the already commercialised CdTe and CIGS technologies, the fabrication of at least 19% efficient kesterite solar cells at laboratory scale is required [17].

The prospects for the deployment of large-scale PV for CdTe and CIGS technologies can potentially be limited by the materials availability, in particular, by the availability of Te, In, Ga and Se. From these elements, Te has been identified as the most critical one when the estimations of production are taken into account [6]. In a less critical case, it is also important to point out that even in Si technologies could have material limitations. In this case, the production of Ag could be problematic since it is used for the contacts [6].

It is therefore possible to conclude that from the thin film technologies, kesterites have significantly lower material limitations than CIGS due to the replacement of In and Ga by Zn and Sn. In addition to this, a greater spectrum of efficient PV technologies, fabricated with more abundant elements, would help to cover the total PV demand reducing risks in materials availability. For example, according to the MIT report “The future of Solar Energy”, supplying 5% of the world electricity demand with CdTe would require directing the entire world production of Te to PV applications [6]. The materials implications for the deployment of PV technologies have also been covered by Forbes and Peter, where they also conclude that the currently commercialized technologies CIGS and CdTe based on scarce elements such as In and Te might be ultimately limited by the availability of raw materials if the current increase in installation rate continues [18].

Although it has been clarified that if the absorbers are Se-containing they cannot be considered fully as earth abundant semiconductors. Selenium is obtained principally as a by-product of copper production, is also abundant in coal, especially high-sulfur coal, and is enriched in coal ash by an order of magnitude. Selenium’s relative abundance in copper and the potential for selenium recovery from coal make it unlikely that the availability of this element would act as the limiting constraint on large-scale Se-containing thin films deployment [6].

In general, from the materials usage point of view for the future deployment of the whole family of PV technologies, the research in kesterites and derived materials such as CTS is clearly justified.

1.3 The scope of this thesis

The interest in researching in kesterite thin film solar cells and related compounds should keep on increasing to ensure a more sustainable deployment of the PV technologies. In order to do so, this project started as a continuation of the previous work elaborated at Northumbria University where a 3.2 % efficient CZTSe solar cell was reported in 2009 [19]. Since kesterites are an emerging PV technology, the main goal of this thesis is not limited just to improve the previous device performances reported by the laboratory at Northumbria University and other groups. This work also aims to contribute to increasing the fundamental knowledge of the kesterite properties and their correlation to their fabrication conditions. This project aims to develop a synthesis process with already successfully industrialised physical vapour deposition (PVD) techniques used for the production of the already commercialised CIGS technology. Along with the development and understanding of the growth process, the fundamental properties of the CZTSe related to its composition and defect chemistry are also explored and compared to other theoretical and fundamental results reported in literature.

In general, the objective of this work was to provide a major contribution to the knowledge about the compound $Cu_2ZnSnSe_4$ and its formation for its use in thin film PV devices. The specific goals of this project can be summarised as:

- Synthesis and fabrication of CZTSe thin films with a potentially scalable method: sputtering of Cu-Zn-Sn metallic precursors followed by a reactive annealing step for the incorporation of Se and the optimisation of this process.
- Study of the phase evolution and formation of CZTSe by the synthesis approach described in this thesis.
- Study of the influence of the composition of the CZTSe absorber layers in its microstructural and optical properties
- Demonstration of the use of CZTSe absorbers in thin film PV devices and assessment of the conditions for maximising its performance.

1.4 The structure of the thesis

Chapter 2 presents an introduction to the history of the research in CZTSe and CTS for its application in PV technologies as part of the larger family of Cu chalcogenide materials for thin film solar cells. It provides a brief literature review of some general aspects of the kesterite community and also provides an insight of the integration of the CZTSe and CTS absorber layers into a PV device and its operation. Chapters 3 and 4 describe the fabrication and characterisation methods used in this project respectively. Theoretical background is also provided, particularly for the most relevant characterisation techniques discussed in this thesis.

The results and discussion from this study are presented in chapters 5,6,7,8 and 9. The chapters are composed of a specific introduction and motivation section to put the research developed into context. A section explaining the specific experimental details of the chapter follows the motivation section. At the core of each chapter are the results and discussion sections which are followed by a summary of the main conclusions of each chapter.

Chapter 5 aims to assess the formation of CZTSe via the study of the selenisation of Cu-Zn-Sn and the copper alloys Cu-Zn and Cu-Sn at different temperatures. A critical analysis of the phases identified in the formation process and a comparison with the data reported in the literature for a similar fabrication process is presented in this chapter. A critical assessment of the potential limitations of the current synthesis process of CZTSe used for the samples of chapters 5 and 6 is also discussed.

Chapter 6 deals with the influence of the composition of the Cu-Zn-Sn metallic precursor on the microstructure of the CZTSe absorber layers. In particular, the variations in composition studied are related to the formation of films with *Cu-rich* (Cu/Zn+Sn>1), *stoichiometric* related to the formula of the compound $Cu_2ZnSnSe_4$ (Cu/Zn+Sn~1) and *Cu-poor* (Cu/Zn+Sn<1) material. Particular emphasis is put in this chapter on the influence of the composition on the microstructure, morphology and defects.

Chapter 7 studies the influence of the Cu content in the CZTSe films but narrowing the range to Cu-poor absorbers, which is the range of composition producing the most efficient kesterite devices as it has been reported in the literature. Significant changes in the selenisation process were implemented in the synthesis of the samples of this chapter with respect to the fabrication method used in chapters 5 and 6. PV devices have been fabricated from these absorbers and their properties are also discussed.

Chapter 8 deals with a revision of the selenisation parameters after the implementation of the changes presented for the synthesis of the CZTSe asborbers studied in chapter 7. In this chapter, the influence of the maximum temperature in the selenisation stage is studied. The structural and optical properties of the absorbers produced are studied and correlated to the behaviour of the devices fabricated.

Chapter 9 presents the fabrication of CTS absorbers and devices by a single step coevaporation method. The interest in the use of CTS as an absorber layer was developed during the phase evolution study discussed in chapter 5. There, the synthesis of the pure selenide version of this ternary compound Cu_2SnSe_3 (CTSe) is presented. The properties of the CTS solar cells fabricated with this compound are discussed as well as the potential of this novel earth abundant semiconductor for PV technologies.

Chapter 10 summarises the work presented in this thesis, highlighting the most important conclusions and discussing the future prospects of kesterite and related materials, in particular CZTSe and CTS.

1.5 Thesis contributions

The work presented in this thesis was carried out by the author with the exceptions that have been clarified in chapter 3 in any fabrication stage, or in chapter 4 in any characterisation done. Appropriate acknowledgements are specified when assistance for any processing or characterisation technique was required.

The evaluation of all results was carried out by the author with the following exceptions:

- The PL measurements and analysis shown in chapter 8, section 8.3.5 were performed by Dr. Michael Yakushev from the University of Strathclyde at Glasgow. Prof. R.W. Martin, Prof. A.V. Mudryi , Prof. J. Krustok and Dr. P.R.

Edwards also contributed to the analysis that is described in detail in reference [20].

- The PLE plots and analysis were performed by the group lead by Professor A. Mudryi from the Material Research Centre of the National Academy of Sciences of Belarus. V.D. Zhivulko and O.M. Borodavchenko also contributed to this work.

Comments and ideas regarding the analysis of the results were received by the co-authors of the publications specified at the beginning of each chapter and also in the following section of this chapter.

1.6 Publications in peer-review journals

1. **J. Marquez-Prieto**, I. Forbes, Evolution of phases in two-stage vacuum processed thin film $Cu_2ZnSnSe_4$ absorber layers, Materials Research Innovations, 18 (2014) 515-518.

2. **J. Marquez-Prieto**, Y. Ren, R.W. Miles, N. Pearsall, I. Forbes, The influence of precursor Cu content and two-stage processing conditions on the microstructure of $Cu_2ZnSnSe_4$, Thin Solid Films, 582 (2015) 220-223.

3. **J. Márquez**, M. Neuschitzer, M. Dimitrievska, R. Gunder, S. Haass, M. Werner, Y.E. Romanyuk, S. Schorr, N.M. Pearsall, I. Forbes, Systematic compositional changes and their influence on lattice and optoelectronic properties of $Cu_2ZnSnSe_4$ kesterite solar cells, Solar Energy Materials and Solar Cells, 144 (2016) 579-585.

4. M.V. Yakushev, **J. Marquez-Prieto**, I. Forbes, P.R. Edwards, V.D. Zhivulko, A.V. Mudryi, J. Krustok, R.W. Martin, Radiative recombination in

$Cu_2ZnSnSe_4$ thin films with Cu deficiency and Zn excess, Journal of Physics D: Applied Physics, 48 (2015) 425109.

5. M. Neuschitzer, K. Lienau, M. Guc, L. Calvo-Barrio, S. Haass, **J. Marquez-Prieto**, Y. Sanchez, M. Espindola-Rodriguez, Y. Romanyuk, A. Perez-Rodriguez, V. Izquierdo-Roca, E. Saucedo, Towards high performance Cd-free CZTSe solar cells with a ZnS(O,OH) buffer layer: the influence of thiourea concentration on chemical bath deposition, Journal of Physics D: Applied Physics, 49 (2016) 125602.
6. **J.A. Marquez Prieto**, S. Levcenko, J. Just, H. Hampel, I. Forbes, N.M. Pearsall, T. Unold, Earth abundant thin film solar cells from co-evaporated Cu_2SnS_3 absorber layers, Journal of Alloys and Compounds, 689 (2016) 182-186.
7. **J. Márquez-Prieto**, M. V. Yakushev, I. Forbes, J. Krustok, P. R. Edwards, V. D. Zhivulko*, et al.*, "Impact of the selenisation temperature on the structural and optical properties of CZTSe absorbers," *Solar Energy Materials and Solar Cells,* vol. 152, pp. 42-50 (2016)
8. M. Neuschitzer, **J.A. Marquez-Prieto**, S. Giraldo, M. Dimitrievska, M. Placidi, I. Forbes, V. Izquierdo-Roca, A. Pérez-Rodriguez, E. Saucedo, Voc boosting and grain growth enhancing Ge-doping strategy for $Cu_2ZnSnSe_4$ photovoltaic absorbers. The Journal of Physical Chemistry C, 120 (2016) 9661-9670.

2 Background

This chapter introduces the history of kesterite solar cells and describes the development of the technology as part of a bigger family; the Cu chalcogenide thin films solar cells. An overview about the history of the crystallographic findings related to kesterite is described. Then, a summary of the synthesis methods of kesterite thin films is also presented. Special emphasis is put on the defect chemistry history of the kesterites, as these studies have been very relevant for the development of this thesis. Finally, the integration of the CZTSe absorber layers in a device structure is described as well as a brief introduction to the physics behind the operation of the solar cells.

2.1 Cu-chalcogenide based absorber layers for thin film solar cells

2.1.1 Cu_2S

The first of the Cu chalcogenide material to be used as an absorber in solar cells was Cu_2S. A priori, Cu_2S is an ideal candidate as an absorber for thin film solar cells. It has a direct bandgap of 1.2 eV, high absorption coefficient and it is formed from earth abundant elements [21]. In the early 80's, 10% efficient solar cells were already reported using $Cd_{1-x}Zn_xS$ buffer layers [22]. However, over a period of weeks, ambient exposure induced oxidation and Cu diffusion from CuS into the CdS buffer layer. This resulted in the degradation of the devices due to the formation of a highly doped $Cu_{2-x}S$ phase [23]. This problem was never solved and the research in this material declined. This fact prompted the community to start researching other alternative materials.

2.1.2 CuInSe$_2$ (CIS) and Cu(In,Ga)Se$_2$ (CIGS)

CIS started to gain interest as an alternative to Cu_2S, and in 1976 there were already reports of thin film solar cells with efficiencies up to 5% reported by Kazmerski et al [24]. With the aim of increasing the bandgap of CIS, Ga was introduced in the crystal structure of the absorber layers for this purpose, this idea being the origin of CIGS. Currently, over 22% efficient solar cells at laboratory scale can be produced [25]. This has been possible by the introduction of Ga along with several important breakthroughs in the development of the synthesis process. The development of two and three stage processes allowing different diffusion of the elements composing the absorber layer and allowed groups to create bandgap gradients. This minimised the recombination processes in the solar cells. Increases in the understanding of the role of Na [26-29] and K [8] led the community to break the barrier of 20% efficiency CIGS solar cells [8, 30].

2.1.3 CZTSSe

The previous development of CIGS, led to a rapid increase in the efficiencies of CZTSSe devices basically by adopting the same device architecture and strategies that were learnt in the previous technology. In 1988, Nakazawa and Ito demonstrated for the first time a photovoltaic effect in a CZTS heterodiode [31]. Almost ten years later, in 1997, Friedlmeier at el. demonstrated 2.3% CZTS and 0.5% CZTSe devices using a CdS/ZnO window layer [32]. In 1999 Katagiri et al. reported a 2.6% CZTS device by the evaporation of Cu-Sn-ZnS precursors followed by a sulphurisation process [33]. Further optimisation of the sulphurisation process increased the performance of the CZTS devices in Katagiri's group up to 6.7%. For doing so, they used an in line sulphurisation-cosputtering system from Cu, SnS and

ZnS targets as shown in a review published in 2009 [34]. In the same year, the group at Northumbria University developed CZTSe solar cells with efficiencies up to 3.2%, this being the world record for the pure selenide version of the kesterite family at that time [19]. The addition of a selenisation step to a solution process precursor containing sulphur and the metals introduced an important breakthrough in the efficiency gain of the technology by the IBM group, reporting a 9.7% efficient CZTSSe solar cell in 2010 [12]. Since then, the IBM group has been leading the record charts of kesterites and they currently hold the world record with devices with efficiencies up to 12.6% [35].

A careful control of the composition has been demonstrated to be a key towards high performing kesterites. The control of the formation of secondary phases in the absorber layer and its defect chemistry is crucial and guided the community to conclude that the composition of CZTSSe should be slightly Cu poor and Zn rich in order to achieve high performing devices [11, 14, 36] . The secondary phases role and formation and the defect chemistry in CZTSSe are reviewed in section 2.2 of this chapter and are a major topic in this thesis.

A great control in the defects of the kesterites and the secondary phases formed in the absorber layers has been developed in the last years. However, if similar efficiencies to CIGS are to be achieved for the commercialisation of the technology, the strategies that led CIGS to increase the lab scale efficiencies over 20% should be understood and studied for kesterites. These strategies include:

- Control of doping (via controlled addition of Na and/or K)
- Fabrication of absorbers with graded bandgap to minimise losses due to recombination.
- Interface engineering to improve the band alignment in the solar cells.

- Development of post deposition treatments (PDT).

The potential effects of the implementation of these strategies in kesterite based devices will be discussed in chapter 10.

2.1.4 CTS

Along with the development of CZTS based solar cells, devices based in the ternary compound Cu_2SnS_3 have been fabricated by several groups. This was encouraged by the fact that similar fabrication routes used for kesterites could also be used for this material [37-47]. The first solar cell using CTS as an absorber layer was reported in 1987 [48]. Until 2012, few reports could be found in literature regarding CTS based solar cells. Along with the rapid progress in kesterite devices, in 2012 several publications started to report CTS solar cells. In this year, Berg et al. reported a 0.5% efficient device [47] and Koike et al. reported a 2.8% solar cell [49], both being prepared using electrodeposited precursors. Devices with efficiencies up to 4% have already been reported [40]. Introducing Ge in the absorber led Umehara et al to report a promising solar cell with an efficiency of 6% with an absorber composition of $Cu_2Sn_{0.83}Ge_{0.17}S_3$ [50]. CTS absorbers have been reported to have bandgaps between 0.9 eV and 1.35 eV, making the material suitable for single junction PV [47, 51]. CTS have been found to crystallise in different structures, including monoclinc, tetragonal and cubic [52]. Its Se counter-part, Cu_2SnSe_3 (CTSe), has also been found to crystallise in the monoclinic system [53]. However, its low bandgap of around 0.5 eV makes it difficult to use the material as an absorber for single junction PV [54].

The results regarding the CTS material and solar cells processed in this thesis are described in detail in chapter 9, where a more detailed introduction to the properties of this material will be provided.

2.2 The crystal structure of CZTSe, secondary phases and defect chemistry.

2.2.1 The crystal structure of CZT(S,Se)

CZTSSe materials are derived from the substitution of two atoms of In in CIS by one atom of Zn and one atom of Sn. This substitution gives CZTSSe similar properties to its predecessor. CZTSSe materials are also known as kesterites, which comes from the crystal structure that $A_2^I B^{II} C^{IV} X_4^{VI}$ (A=Cu; B= Zn or Fe; C= Sn; X= S or Se) type compounds adopt in nature ($Cu_2(Zn,Fe)SnS_4$) [55]. These type of compounds can also adopt another tetragonal type structure called stannite [56]. Both, the kesterite and stannite structures have a closed cubic-packed array of anions with the cations occupying half of the tetrahedral voids [55]. The difference in the symmetry of the structures arises from the different distributions of the cations in the unit cell, as represented in figure 2.1. The difference in the kesterite and stannite type crystal structures was accurately described by Schorr [55]: “The kesterite type structure is characterized by alternating cation layers of CuSn, CuZn, CuSn and CuZn at z= 0, 1/4, 1/2 and 3/4 respectively. Thus one copper occupies the 2a (0,0,0) position with zinc and the remaining copper ordered at 2c (0,1/2,1/4) and 2d (0,1/2,3/4) resulting in the space group $I\bar{4}$. On the other hand, in the stannite type structure ZnSn layers alternate with Cu_2 layers. The structure is consistent with the symmetry of the space group $I\bar{4}2m$, with the divalent cation located at the origin (2a) and the monovalent cation at the 4d position (0,1/2,1/4). Sn is located at the 2b site (0,0,1/2) in both structures. The anions lie on the (110) mirror plane at 8i (x,x,z) for the stannite type and 8g (x,y,z) for the kesterite type structure."

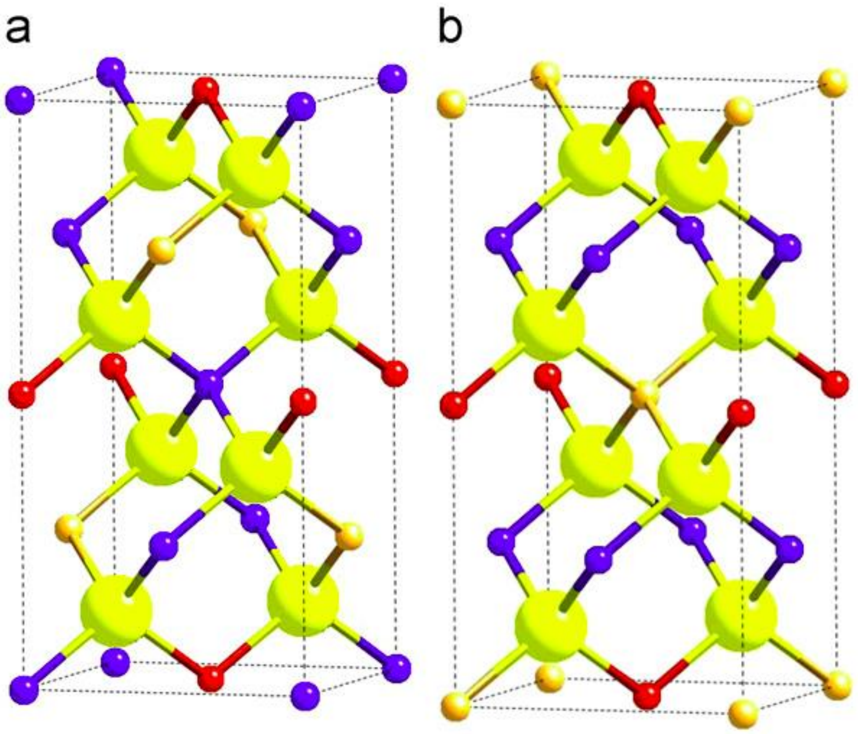

Figure 2.1 Unit cell representations of the kesterite type structure (a) and stannite type structure (b). Cu atoms are represented in blue, Zn atoms in yellow and Sn atoms in red. The big light yellow spheres represent the anions. This figure is adapted from [55].

In the same manuscript, Schorr reported that CZTS and CZTSe both crystallised in the kesterite type structure in a neutron diffraction study [55]. This was in agreement with first principle calculations [57]. The kesterite type structure, is defined in figure 2.1. In its ideal case, the structure has the Cu and Zn atoms at z=1/4 and 3/4 located in the 2c and 2d positions respectively. It could also occur that these atoms are interchanging their positions, forming the antisite defects Cu_{Zn} and Zn_{Cu} [55]. When there is random distribution of Cu and Zn atoms in the Cu-Zn (001) planes, then the unit cell is of greater symmetry ($I\bar{4}2m$) and it is also known as the kesterite disorder structure [58]. It is normal to think that the synthesised kesterites are neither fully ordered nor fully disordered, and several reports in literature support this [55, 58-60]. Understanding the influence of disorder in the crystal structure has attracted the attention of the community in the last years. Several studies concluded that different levels of disorder affected some properties of the material, for example the bandgap [58, 60, 61]. The effect of compositional changes on the order-disorder kesterite phenomenon is discussed in chapter 7.

2.2.2 Secondary phases and the pseudo-ternary phase diagram

The narrow phase stability of CZTSe implies that formation of secondary phases either in the growth or in post-growth processes is very likely to occur [11]. Therefore, understanding the formation of the growth of the secondary phases associated to the composition of the CZTSe absorbers and the processing conditions is a key to improve the synthesis routes towards higher quality absorber layers.

The compositional limits of the phases are normally defined in the phase diagrams. The phase diagram of CZTSe was published by Dudchak et al. [62] and it is shown in figure 2.2. At this point is important to describe some characteristics of this phase diagram to define under which limitations it can be used. First of all, it is an isothermal section at 400 ºC, so it is valid just at temperatures around this value, since the deviations of the diagram at higher and lower temperatures are uncertain. There should also be enough Se to form Cu_2Se, ZnSe and $SnSe_2$ so the total amount of Se in the bulk should not deviate too much from 50 at%. It is not valid for rapid thermal processing, since the diagrams show the most stable phases (equilibrium) for given conditions. In this thesis, particularly in chapters 5, 6 and 7 this phase diagram has been used. According to the limitations stated above for the use of the pseudo-ternary phase diagram of CZTSe, the use of the figure has been limited for qualitative purposes. The aim of the use of this diagram is to orientate the reader about variations in compositions and for non-quantitative predictions of potential secondary phases.

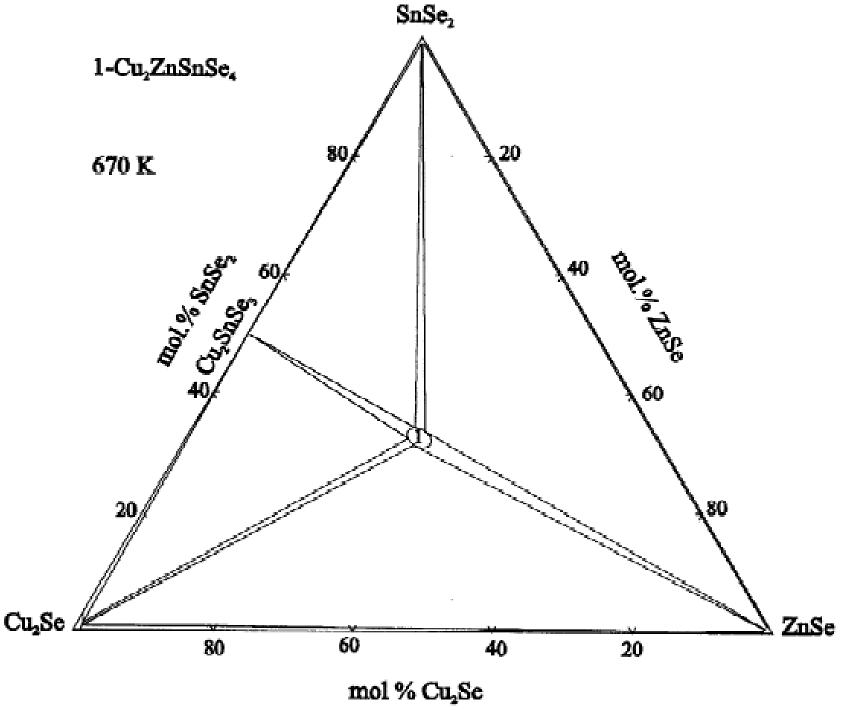

Figure 2.2 Pseudo-ternary phase diagram Cu_2Se-ZnSe-$SnSe_2$ at 397 ºC. Image from [62].

For the case of CZTSe, the presence of secondary phases has been demonstrated to have a detrimental effect on the device performance. Cu_2SnSe_3 is the most detrimental due to its low bandgap of 0.5 eV [36]. The highly resistive ZnSe phase is very likely to also reduce the solar cell performance and Sn-Se binary phases have been found to induce shunting paths in the CZTSe solar cells [63-65].

2.2.3 Defects in CZT(S,Se)

Defects in the lattice of CZT(S,Se) define the optoelectronic properties of the material, and therefore there is interest in understanding their nature and exploring ways to identifying them.

A large variety of defects have been theoretically calculated for kesterites and some of them have also been experimentally observed. These defects can appear as vacancies (V_{Cu}, V_{Se}…), interstitials (Cu_i, Zn_i, Se_i …), antisites (Cu_{Zn}, Sn_{Cu}, Cu_{Sn}, Zn_{Cu}…) and charged-compensated defect clusters (V_{Cu}+Zn_{Cu}, Zn_{Sn}+2Zn_{Cu}…). These defects can be either beneficial or detrimental, depending on their concentration and the position of the energy level that their presence can induce. For example, selenium vacancies can act as a donor by introducing an energy level in the middle of the band gap of CZTSe [11]. This level can become an active recombination centre and is thus detrimental for the solar cell performance. The potential of defects to be formed can be predicted by theoretical calculations. It has been calculated that the Cu_{Zn} antisite has the lowest formation energy of the intrinsic defects in kesterite-type compounds [11]. Another acceptor defect with low formation energy in kesterites is the Cu vacancy [11]. All these acceptor defects can be present in high concentrations and they contribute to an increase in the hole concentration in the CZTSe and are primarily responsible for the intrinsic p-type conductivity of the material. Considering that multiple types of defects can be formed in these quaternary compounds, self-compensated defect clusters can also be formed as a consequence of atomic substitutions that mantain charge neutrality (acceptor-donor combinations). These clusters, do not then contribute to the hole concentration in

CZTSe. It has been calculated that the formation energy of these complexes is lower than the relative sum of the isolated ones [11, 66]. The defect cluster with the lowest formation energy is the Cu_{Zn} +Zn_{Cu} cluster which is formed from the lowest-energy acceptor and donor defects respectively. As mentioned in the previous sub-section, these defects are responsible for the partial disorder of the kesterite type-structure and can be found in high density [11, 55, 66, 67]. Lafond et al. described important atomic substitutions keeping the charge balance for non-stoichiometric CZT(S,Se), for Cu-poor, and also for Cu-rich regions [68]:

For the Cu-poor Zn-rich region

$2Cu^{+} \rightarrow Zn_{Cu}^{2+} + V_{Cu}$(A-type)

$2Cu^{+} + Sn^{4^{+}} \rightarrow 2Zn_{Cu}^{2+} + Zn_{Sn}^{2+}$ (B-type)

For the Cu-rich and Zn-poor region

$3Zn^{2^{+}} \rightarrow 2Cu_{Zn}^{+} + Sn_{Zn}^{4+}$ (C-type)

$Zn^{2^{+}} \rightarrow Cu_{Zn}^{+} + Cu_{i}^{+}$ (D-type)

These substitutions are associated with compositional lines in the ternary phase diagram [68] and are represented in figure 2.3. These defect lines can also be represented in a diagram with the Zn/Sn and Cu/(Zn+Sn) ratio which are commonly used to described the composition of the CZT(S,Se) films. This is shown in figure 2.4. These two figures have been used for an initial assessment of the possible defect clusters that can be presented in the material synthesized for this thesis.

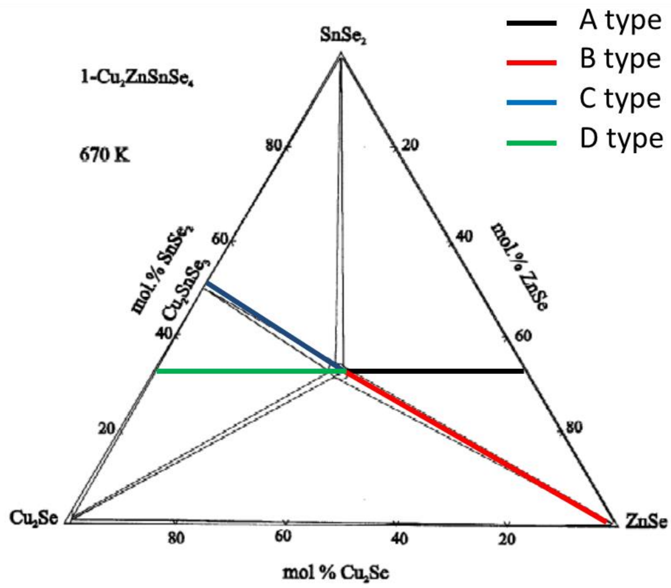

Figure 2.3 Pseudo-ternary phase diagram Cu_2Se-ZnSe-$SnSe_2$ showing the compositional lines associated to the charged compensated defined as A type (black), B type (red), C type (blue) and D type (green) described in the text. Adapted from [62].

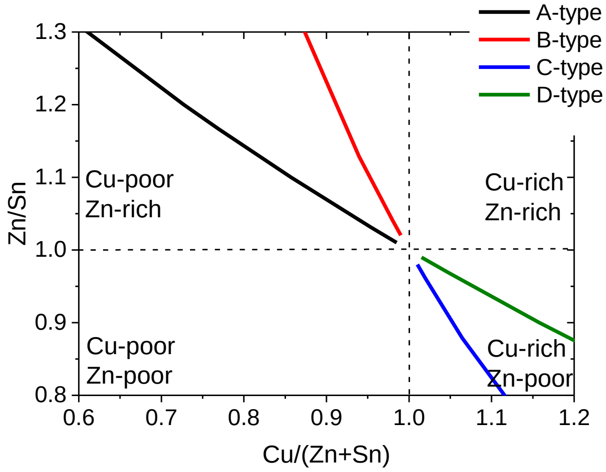

Figure 2.4 Compositional lines associated to the charged compensated defined as A type (black), B type (red), C type (blue) and D type (green) represented as a function of the Zn/Sn and Cu/(Zn+Sn) metallic ratio of the CZTSe films. The plot is courtesy of Prof. Susan Schorr.

The most interesting range of composition is the Cu-poor and Zn-rich region, where the devices with higher performance are produced [11, 14, 36]. In this thesis, understanding the defects present in the CZTSe synthesized in this particular range of composition was prioritised and is discussed in chapters 6, 7 and 8.

2.3 Synthesis of $Cu_2ZnSnSe_4$ thin films

One of the main advantages of the kesterite technology is its great versatility in terms of synthesis approaches. The majority of kesterite absorber layers are synthesised via a 2-stage process consisting of the deposition of a precursor layer followed by a reactive annealing step with sulphur and/or selenium. CZT(S,Se) devices with efficiencies greater than 8% have been achieved by a variety of vacuum synthesis methods including co-evaporation [69, 70], sputtering [71, 72], reactive sputtering [73]. Electrodeposition [74] and several other liquid processing techniques, including the deposition of a CZTS solution either by spray of spin coating [35, 75-78], have also been used for fabricating highly efficient devices. The reader is referred to the review article reported by Delbos for a compilation of several synthesis routes for kesterite based absorbers [14]. The way of fabricating the absorbers are normally classified in two groups, the vacuum process techniques (co-evaporation, sputtering) and the non-vacuum techniques (electrodeposition, spin/spray coating of CZTS solution…), which normally refers to the way that the precursor layer is deposited.

There is one important thing that the groups synthesising highly efficient kesterite absorbers have in common, that, with the exception of the CZTSe processed by coevaporation by the group at NREL [69] and Luxembourg [79], all processes involved a 2nd step consisting of the sulfurisation (for the case of CTZS) or selenisation (for the case of CZTSe or CZTSSe) of the precursors at temperatures between 450 ºC and 600 ºC. In the case of selenium-pure kesterites (CZTSe), the best devices found in literature are dominated by vacuum deposited precursors with the exception of the electrodeposited films reported by Vauche et al. [74], i.e. the 11.6% efficient world record CZTSe reported by Lee et al. [16]. For the pure selenide case, there are no reports of highly efficient devices reported based on solution process CZTSe precursors. This might be due to limited research on these routes to avoid the use of more expensive and toxic Se containing chemicals that would be needed to prepare the precursor ink such as selenourea (CH_4N_2Se).

2.3.1 Efficiency chart of pure selenide kesterite solar cells and the selection of the chalcogen source

Since a 3.2% pure selenide solar cell was reported in 2009 by the group at Northumbria University, several groups progressed significantly in making efficient devices with CZTSe absorber layers. In 2013, at the beginning of the research of this thesis, the efficiency charts of CZTSe based devices were dominated by NREL with a 9.2% efficient device deposited by co-evaporation. In Europe, the best CZTSe devices were processed by IMEC, using H_2Se (g) as the chalcogen source [80].

As mentioned earlier, the selenisation-annealing step plays an important role for the synthesis of high quality CZTSe. Several Se sources led to high efficiency pure selenide kesterite solar cells and they are summarised in table 2.1.

In the experiments presented in this thesis, two different types of Se sources were employed. The first one was used for the synthesis of the samples presented in chapters 5 and 6. In this case, an evaporated cap layer of Se on top of the precursor layer was deposited, as described in section 3.3.1. Some issues related to this way of incorporating the chalcogen in the samples were identified. These issues will be discussed in chapter 5. Because of these problems, the synthesis of the CZTSe films in chapters 7 and 8 was performed using Se pellets, as described in section 3.3.2. The use of H_2Se (g) was avoided for safety reasons, despite having demonstrated good results in a similar approach [80-82].

Since many efficiency charts of kesterites involving the pure sulphide CZTS, the pure selenide CZTSe and the solid solutions CZTSSe together can be found in reviews in the literature [14, 75, 83, 84], this section aims to discuss the progress made only in the pure selenide counterpart of the kesterites. A compilation of the current density-voltage (J-V) characteristics of CZTSe solar cells with efficiencies higher than 7% is also shown in table 2.1, including the open circuit voltage (V_{OC}), fill factor (FF) and current density (J_{SC}) values. In this table, the values the J-V parameters of the best device of this thesis are also shown in the bottom row. The direct comparison of the current density values is complicated because in many cases these values are reported using the active area of the cell for the calculation, or the solar cells have MgF_2 as antireflecting coating. Nevertheless, it is interesting to see that for the case of pure selenide devices found in literature, the best CZTSe solar cell fabricated in the development of the research discussed in this thesis has the largest open circuit voltage (V_{OC}). The reasons for the large characteristic V_{OC} of this device will be discussed throughout this thesis, particularly in chapter 7 and 8. The reader is referred to section 4.5 for insights into the J-V analysis of solar cells.

Table 2.1 Summary of J-V parameters of CZTSe solar cells reported in literature. The method indicates the technique used for depositing the precursor. The way of introducing the Se in the synthesis process of the absorber layer is also indicated. This table is an adaptation from a table reported by Vauche [84].

- IMEC = Interuniversity Microelectronics Centre
- NREL = National Renewable Energy Laboratory
- IREC = Catalonia Institute for Energy Research
- IRDEP = Institute of Research and Development on Photovoltaic Energy
- KIST = Korea Institute of Science and Technology

Group	**Method**	**Se source**	**Eff (%)**	**J_{SC} (mA cm^{-2})**	**V_{OC} (mV)**	**FF (%)**	**Ref**
IBM	Co-evaporation + selenisation	No information	11.6	40.6	423	67.3	[16]
IMEC	Sputtering	H_2Se (g)	10.4	39.7	394	66.4	[81]
NREL	Co-evaporation	Se in cracking unit	9.8	37.6	380	68.9	[69, 85]
Nakai Univ.	Sputtering	Not given	8.7	36.2	418	57.6	[86]
IREC	Sputtering	Se powder	8.2	32.4	392	64.4	[71, 87]
Luxembourg Univ.	Co-evaporation	Se in cracking unit	8.1	42.1	331	58	[79]
IRDEP	Co-sputtering	Se in cracking unit	7.1	30.7	390	59.8	[88]
KIST	Electrodeposition	Not given	8.0	35.3	390	58	[89]
NEXCIS	Electrodeposition	Se powder	8.2	30.9	425	62.7	[74]
Northumbria Univ.	Sputtering	Se pellets	8.1	31.1	434	59.8	[90]

2.4 CZTSe and CTS solar cells: Device integration, physics of the solar cell and recombination mechanisms

Thin film solar cells based on Cu chalcogenides are fabricated in the form of heterostructures. These heterostructures are basically made by joining a p-type semiconductor material to a different semiconductor material that is n-type. One of the semiconductors is a light absorber and the other would be a window material or a wide gap semiconductor contributing very little to carrier generation, but is needed to create the heterojunction to separate the carriers. Therefore, a p-n junction diode, is formed between the p-type and n-type material.

Light-generated current in a solar cell occurs via the generation of electron and hole pairs due to the absorption of photons with energy greater than the bandgap and their spatial separation due to an electric field created by the p-n junction.

2.4.1 Solar cell architecture

The architecture used to make kesterite solar cells is adapted from the CIGS technology. In this section, only the so called “substrate configuration” will be described, where the absorber layer is grown in the order on top of the back contact/substrate, which forms the mechanical support for the thin film structure. The window layer is deposited on top of the absorber layer. Figure 2.5 shows a schematic diagram of the structure of a kesterite solar cell. The layers shown in the diagram are grown from the bottom to the top as is described in chapter 3. In this thesis, the substrates used were soda lime glass (SLG). Flexible substrates can also be used for CIGS and kesterite solar cells [8, 10]. On top of the SLG, a Mo metallic layer is deposited by sputtering and it serves as the back contact of the device. On top of the back contact, the kesterite CZTSe absorber layer is grown. As a result of a reaction with Se and the CZTSe [91], a $MoSe_2$ layer is formed between the metallic Mo and the absorber layer. To form the p-n junction, normally a thin CdS buffer layer is deposited on top of the absorber by chemical bath deposition, as for the example described by Neuschitzer et al. [71]. This material has given the best results so far in terms of efficiency for kesterite solar cells and also for CIGS technology [30, 35]. Also, other materials such as Zn(S,O,OH) buffer layers can be used to replace CdS [92]. To finally close the device, a window layer is sputtered on top of the buffer layer. The materials used for this are transparent conductive oxides (TCO) and in the case of this thesis, Al doped ZnO (AZO) has been used as the front contact of the devices.

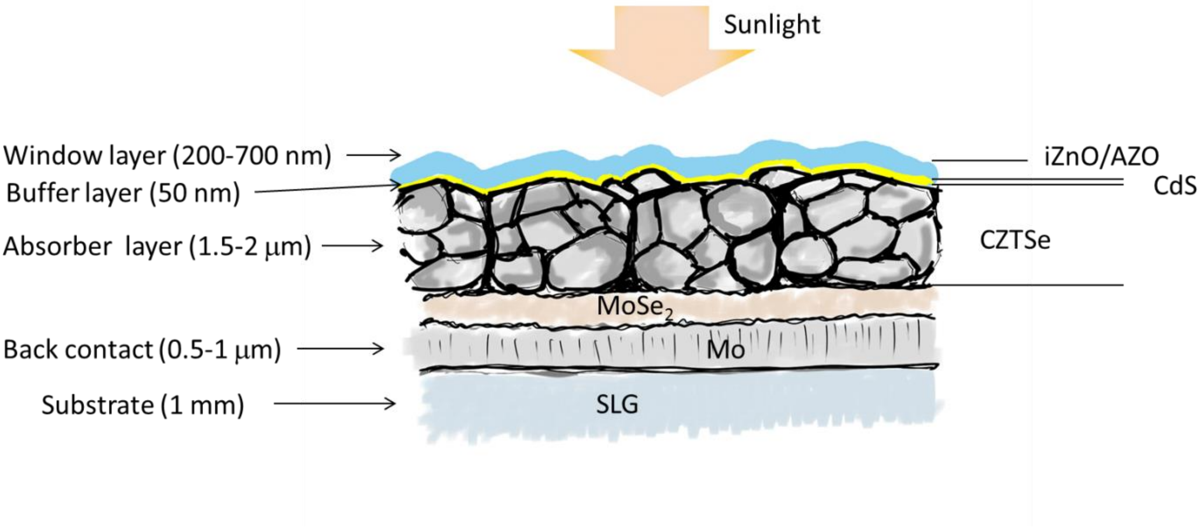

Figure 2.5 Schematic diagram of a CZTSe solar cell indicating the layers and approximate thicknesses of each one. The materials forming each layer are also indicated.

2.4.2 Physics of the p-n junction

The physics of the p-n junction (diode) has been well covered in several excellent text books and the reader is referred to them for an extended description [93-95] .

This section focuses on summarising the important points to understand the basic transport mechanisms behind the physics of the solar cells.

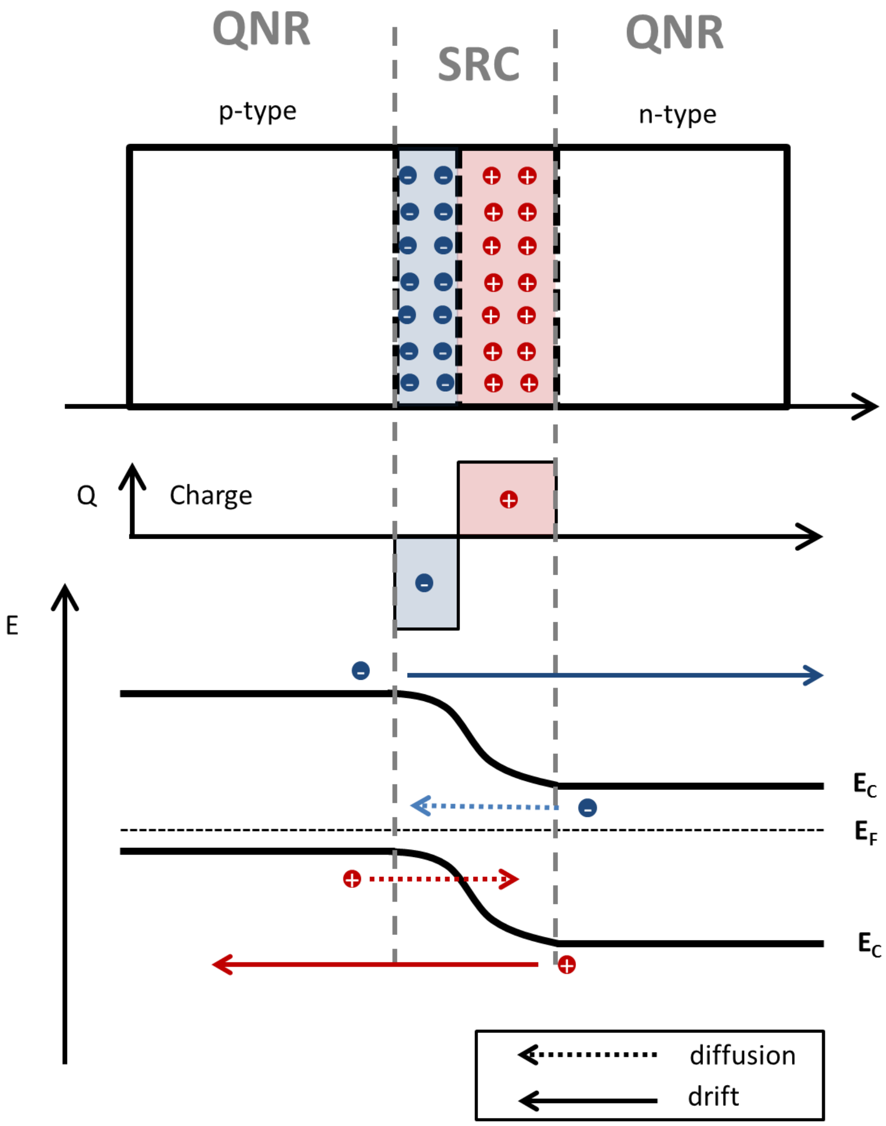

Figure 2.6 Schematics diagram of a p-n junction (top) showing the quasi-neutral region (QNR) and the space charge region (SCR), space charge density (middle) and the bending of the valance and the conduction band (bottom) under equilibrium. The transport of electrons and holes due to diffusion or drift are also represented in these diagrams. This figure is inspired by [93, 96].

The Fermi level in a p-type semiconductor is close to the valence band, whereas in a n-type semiconductor it is close to the conduction band. When both type semiconductors are electrically contacted, the conduction and the valence band need to bend in the interface to reach equilibrium. The region where the bands are bent is called the space charge region (SCR). In order to form the SCR, the majority carriers of the n-type semiconductor (electrons) diffuse towards the p-type semiconductor to a more energetically favourable state. The same occurs with the majority carriers of the p-type semiconductor (holes) that diffuse towards the n-type. This is known as the diffusion current. By this process, positively charged ions are left in the n-type semiconductor part and negatively charged ions are left in the p-type part having created an electric field. This electric field opposes the diffusion process, and allows a current in the opposite direction to flow, so-called drift current. For an illustrative explanation of this principle of operation of a p-n junction the reader is referred to figure 2.6

Once a semiconductor is under illumination, the energy of the light can promote an electron from the valence band to the conduction band leaving a positively charged absence of a particle (hole) behind. The separation of an electron and a hole due to excitation energy is not infinite, and these particles can recombine. The recombination mechanisms are covered in the next subsection. Under an electric field, electrons and holes can be driven in opposite directions before the recombination process happens. This electric field can be created by a p-n junction, and therefore the photoexcited electrons (and holes) can be transported to the terminal of a device and be collected.

In the work presented in this thesis, the p-n junction in the solar cells were created between the p-type CZTSe (or CTS in chapter 9) and an n-type CdS.

2.4.3 Recombination mechanisms

As mentioned in previous sections, once electrons are excited into the conduction levels and holes are created in the valence levels, they need to be separated by an electric field in order to be collected in the terminals of the solar cells. However, excited electrons can return to their ground state before being collected. This phenomenon is known as recombination and can happen in different ways that are introduced briefly in this section.

2.4.3.1 Radiative recombination (band-band)

Radiative recombination normally dominates in direct bandgap semiconductors. In radiative recombination, an electron in the conduction band directly combines with a hole in the valence band, and this process emits a photon with energy similar to the difference between the energy of the bands, i.e. the bandgap of the semiconductor. Due to the fact that the emitted photon has energy similar to the bandgap is therefore weakly absorbed and can escape the semiconductor. In some cases, radiative recombination can occur via defects if they are shallow, and this possibility in the case of CZTSe will be discussed in chapter 8. A band to band recombination process with the emission of a photon is illustrated in figure 2.7.

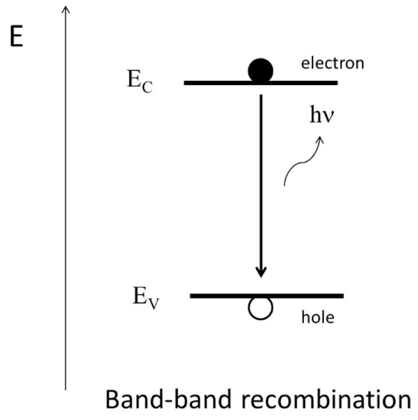

Figure 2.7 Simplified diagram describing a band to band recombination process.

2.4.3.2 Recombination through defect levels

The recombination through a defect level is also called Shockley-Read-Hall (SRH) recombination and occurs in materials with imperfections. SRH recombination can be described as a two-step process. First, an electron (or a hole) is trapped in a forbidden region (an energy level within the bandgap) which is normally introduced though defects in the crystal lattice, for example when an atom of an element is located in the position in the lattice that should be occupied by another element. Then, a hole (or an electron) can recombine in the same energy level before the carrier is re-emitted to the band. It is important to mention that in complex materials like CZTSSe, defects are very likely to occur unintentionally, but can be controlled to induce changes in the properties of the materials. If the energy levels are close to the band edges (shallow defects), the recombination process is less likely to happen since the energy difference is small and the re-emission process to the band edges is more likely to occur. Because of this, energy levels in the middle of the bandgap (deep defects) are more effective recombination centres. A SRH recombination process is illustrated in figure 2.8

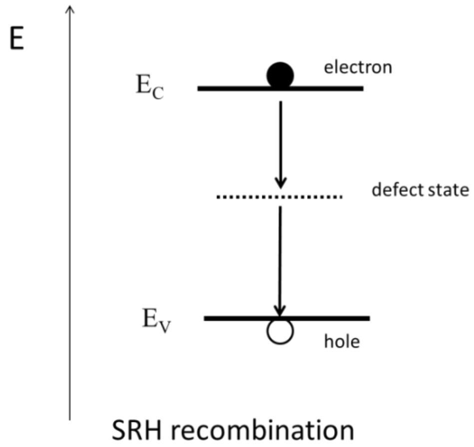

Figure 2.8 Simplified diagram describing a SRH recombination process through a defect state in the middle of the bandgap

2.4.3.3 Auger recombination

Auger recombination involves three carriers and it is a similar process to the band-band recombination. In this case, after an electron in the conduction band recombines with a hole in the valence band, the energy released from the process is transferred to an electron in the conduction band. This recombination process is typical from heavily doped material and the heavier the material is doped, the shorter the recombination lifetime is. An Auger recombination process is illustrated in figure 2.9

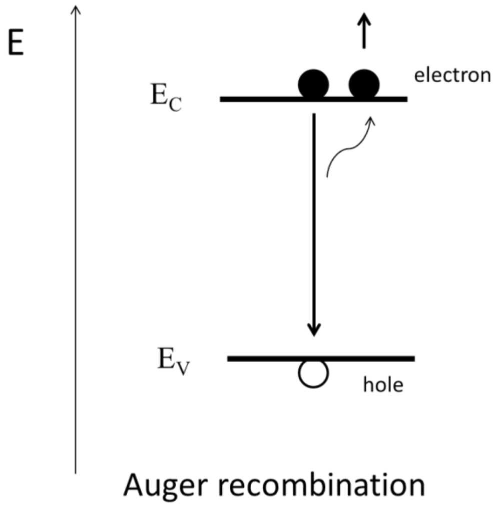

Figure 2.9 Simplified diagram describing an Auger recombination process.

3 Processing techniques

This chapter describes the processing techniques used for the development of the material of this thesis. The synthesis of the CZTSe absorbers in this thesis was a 2-stage process consisting of the physical vapour deposition of Cu-Zn-Sn precursor layers by sputtering followed by a reactive annealing step in Se atmosphere where the metallic precursors were selenised and converted into the CZTSe absorber layers of chapters 5, 6, 7 and 8. The process of fabrication of solar cells is also explained in this chapter of the thesis. In addition to the description of the synthesis of the CZTSe absorber layers, the coevaporation process used for the fabrication of the CTS absorber layers of chapter 9 is also described.

3.1 SLG/Mo Substrates

In this study, molybdenum coated soda lime glass (SLG/Mo) has been used for the substrates. The dimensions of the SLG used were either 76 x 26 x 1 mm^3 or 50 x 50 x 1 mm^3.

Typically, the Mo, which is used as the back contact in CIGSe and kesterite solar cells, is deposited by sputtering. The system used for this deposition was a 3-target Nordiko 2000 radio frequency (RF) magnetron sputtering system. The targets used in this system were 15 cm in diameter and are facing down above a substrate table to enable the deposition downwards as illustrated in figure 3.1. The substrate table rotates making the platens holding the samples pass underneath each target. This allows the capability of sputtering from the three targets uniformly in depth. The rotating speed used for the sputter depositions of this system was 2 rotations per minute. This means, that in a normal deposition of 1 hour, the substrates will pass 120 times underneath each target.

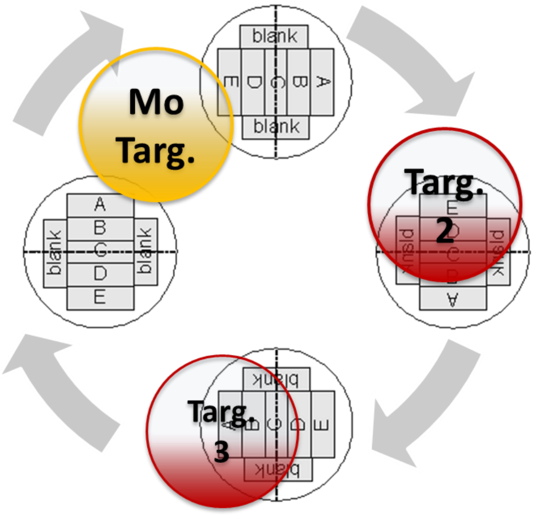

Figure 3.1 Schematics of the top view of the Nordiko 2000 sputtering system. The three targets are represented in yellow and red and are in a fixed position. Underneath the targets, four platens are located that are rotating as indicated by the arrows, allowing the substrates located on them to pass underneath the targets.

For the Mo back contact deposition one elemental high purity target (5N) was used. The chamber was evacuated to a base pressure typically of 10^{-6} Torr prior to deposition. During the deposition, the chamber was filled with Argon at a typical working pressure of 3×10^{-3} Torr. A voltage was applied between the targets and the substrate making the Ar atoms to be ionised. The positively charged Ar ions are attracted to the targets which are hit making their component elements be ejected towards the substrate table where they were deposited.

850 nm thick Mo layers were obtained after 2 hours deposition at 300 W. The sheet resistance of the layers was typically tested by four point probe technique [97]. Sheet resistance values between 0.4 and 0.5 Ohm sq^{-1} were obtained in these samples.

Additionally, SLG/Mo substrates from the Ångström Solar Centre at Uppsala University were used for the work described in chapter 7 and chapter 8. The experimental details related to these substrates are reported elsewhere [98].

3.2 Sputtering of the Cu-Zn-Sn precursor layer

The sputtering of the Cu-Zn-Sn metallic precursor was produced at room temperature with a Nordiko 2000 with the same principle explained in part 3.1 and it is schematically represented in figure 3.2. High purity (5N) Cu, Zn and Sn elemental targets were used for the deposition. The rotation speed of the substrate table was kept fixed in 2 rotations per minute. The "multi thin layers" approach used for fabricating the metallic precursors allowed fabricating samples where the three elements are uniformly distributed in depth as it is possible to see in figure 3.3 in a glow discharge optical emission spectrometry (GDOES) elemental profile.

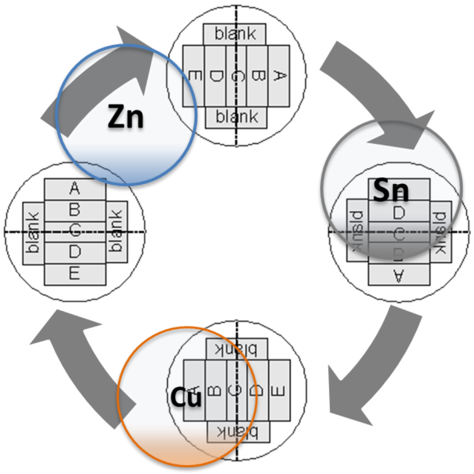

Figure 3.2 Schematics of the top view of the Nordiko 2000 sputtering system. The three targets (Cu, Zn and Sn) are in a fixed position. Underneath the targets, four platens are located that are rotating as indicated by the arrows, allowing the substrates located on them to pass underneath the targets.

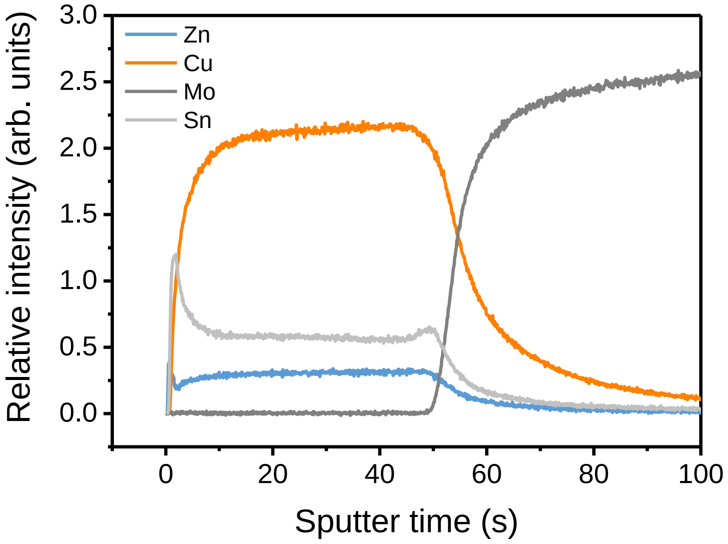

Figure 3.3 Elemental distribution Cu, Zn, Sn and Mo of a sputtered CZT metallic precursor on Mo coated SLG. This GDOES profile was acquired with the help of Lars Steinkopf from the HZB.

Variation of compositions in the films was achieved by varying the power applied to each target. An example of how the composition was systematically varied is presented in table 3.1 for the precursors used for chapter 6. The characterisation methods used for measuring the composition of the films are described in chapter 4. In this case a series of CZTSe films were prepared by varying systematically the precursor Cu content. It is important to point out that the behaviour of the targets has been monitored during the whole project and the power applied to them has been continuously adjusted and re-calibrated to obtain the desired compositions. The variation of the target behaviour can be attributed to the continuous erosion produced in them by the sputtering process as well as slight changes in the physical contact with the power supplies, which can be different when the targets have been replaced or changed. The thickness of the precursors can be controlled by adjusting the deposition time. In this thesis, the normal deposition time for the precursor layers ranged between 30 and 40 minutes, resulting in films with thicknesses between 450 nm and 600 nm.

Table 3.1. Variation of Cu atomic ratio in relation to the power applied to the targets during sputtering deposition.

	EDX-Precursors	Power (W)		
Sample	**Cu/(Zn+Sn)**	**Cu target**	**Zn target**	**Sn target**
Cu poor	0.90	130	70	140
Stoichiometric	0.99	150	70	140
Cu rich	1.12	170	70	140

3.3 Selenisation of CZT precursor layer

The conversion of the CZT metallic precursors into the chalcogenide absorber CZTSe was identified as a key process to achieve high performance solar cells. During the development of the work of this thesis, this process has been in a continuous evolution, which has finally led to a progress in the performance of the solar cells due to an improvement of the structural and optoelectronic properties and a subsequent improvement in the solar cell performance. Two different systems were used for selenising the precursors. The samples studied in chapter 5 and 6 have been selenised in a tube furnace where the heating ramping rate was limited to a maximum of 30 ºC per minute and a long natural cooling time. The samples presented in chapter 7 and 8 were selenised using a rapid thermal processor that allowed heating ramping rates of around 5 ºC per second. Some other differences such as the background pressure, the design of the graphite boxes containing the sample or the method of introducing the chalcogen are discussed in the following subsections.

In the development process of the selenisation step many more variables than the ones reported in this thesis have been studied. To achieve the selenisation conditions for the best devices reported in this thesis, extensive studies in this step were carried out such as how much Se should be supplied, the time at the maximum temperature or the effect of the heating ramp rate. Although these studies are not described in detail in this thesis, they were key experiments that led to the best selenisaton conditions for the fabrication of the CZTSe absorbers, and the changes between both selenisation processes described below are a result of a continuous study. This means that this process has been developed gradually and not as abrupt as the comparison between the following sub-sections 3.3.1 and 3.3.2 could suggest. The selenisation conditions producing the most efficient devices of this project are shown in chapter 10.

3.3.1 Tube furnace approach

The process used to selenise the CZT precursor comprises the evaporation of a Se cap and a post heating treatment inside a graphite box placed in a tubular furnace. The tubular furnace has a maximum heating speed of around 30 °C per minute and the cooling of the system is natural, taking several hours from temperatures around 500 ºC to room temperature. A schematic description of the process is shown in figure 3.4. The thickness of the evaporated Se cap was chosen to be 2.3 μm. This thickness was chosen after an initial assessment of the minimum amount of Se required to selenise a 650 nm thick CZT precursor layer and convert it into kesterite without the detection of secondary phases by XRD in Bragg Brentano configuration.

The same process was used for the conversion of the Cu-Zn and Cu-Sn precursors discussed in chapter 5.

Before starting the reactive annealing, the tube was filled with Ar with a final pressure of 1 mbar. These conditions were kept constant for the synthesis of the samples presented in chapter 5 and 6. Throughout this thesis, the amount of inert gas used to fill the annealing system where the graphite reactors with the samples are placed will be referred as “the background pressure”.

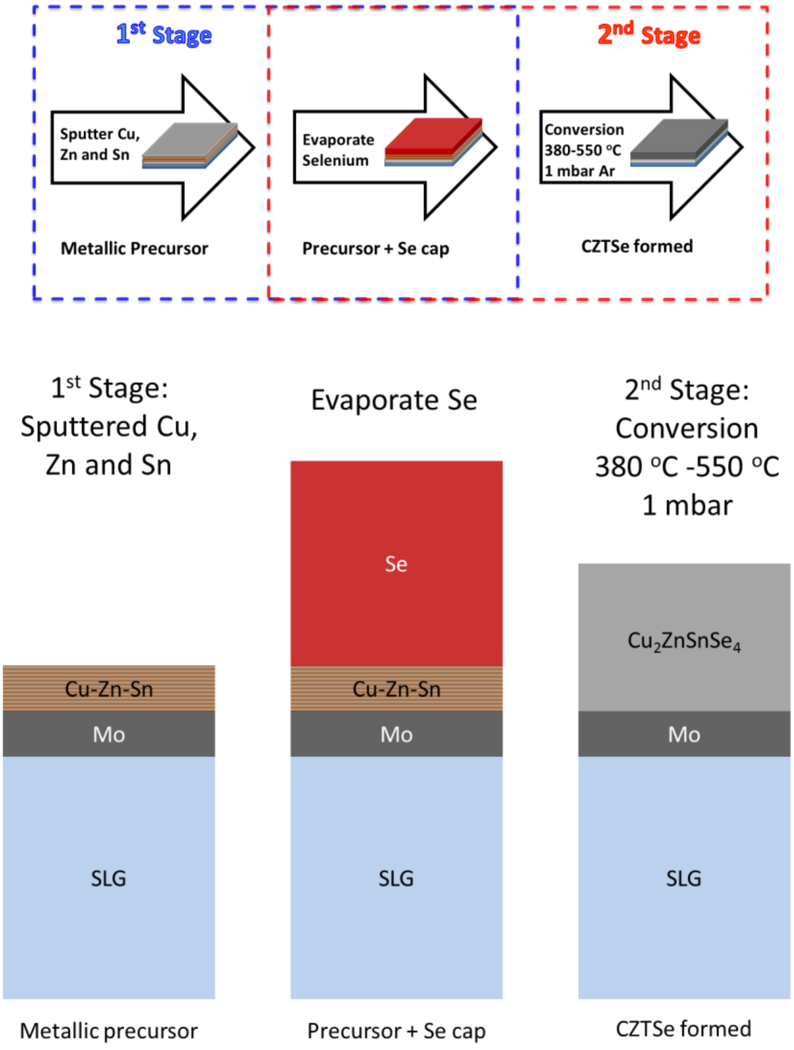

Figure 3.4. Schematic description of the two stage synthesis process with evaporation of Se cap and conversion in a tubular furnace for the samples discussed in chapters 5 and 6.

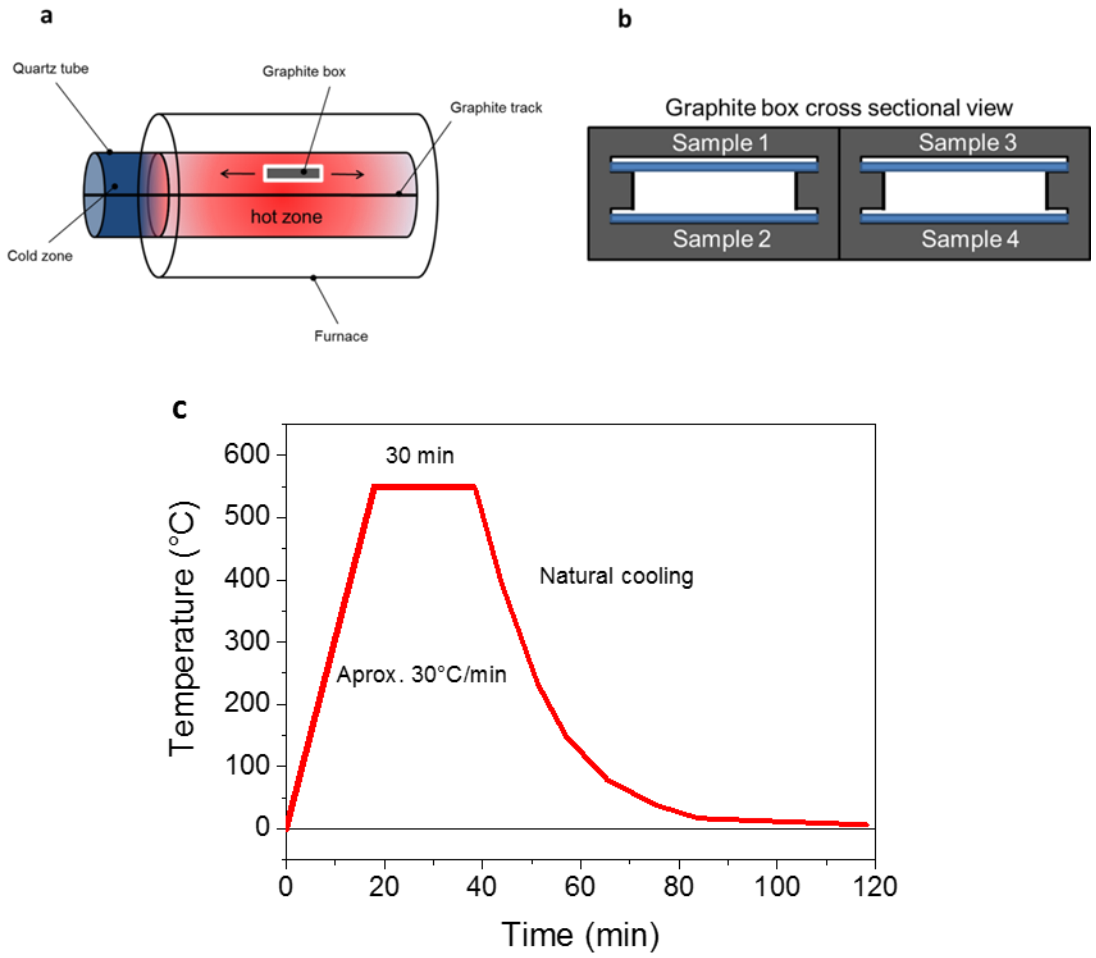

Figure 3.5 a) Schematic representation of the quarz tube furnace and b) cross section of the graphite boxes used for the selenisation process of the CZTSe samples discussed in chapters 5 and 6. The schematic diagram of the tubular furnace is courtesy of Dr. Pietro Maiello from Northumbria University. c) Example of heating profile of a typical selenisation process used for the synthesis of the CZTSe absorbers discussed in chapters 5 and 6 using the tube furnace at a maximum temperature of 550 ^{o}C.

Graphite boxes were used to enclose the samples inside the tube furnace. The graphite boxes had an internal volume of approximately 12 cm^3. 4 samples with dimensions of 0.1 x 2.6 x 7.6 cm^3 were placed inside each graphite box as shown in the cross section scheme view shown in figure 3.5 along with a schematic view of the tubular furnace where they were introduced and an example of a heating profile.

3.3.2 Rapid Thermal Process approach

The rapid thermal selenisation of the samples presented in chapters 7 and 8 of this thesis has been performed with an “as-one” rapid thermal processor (RTP) from Annealsys. An illustration of the RTP is shown in figure 3.6.a. The Cu-Zn-Sn precursors were introduced in graphite reactors.

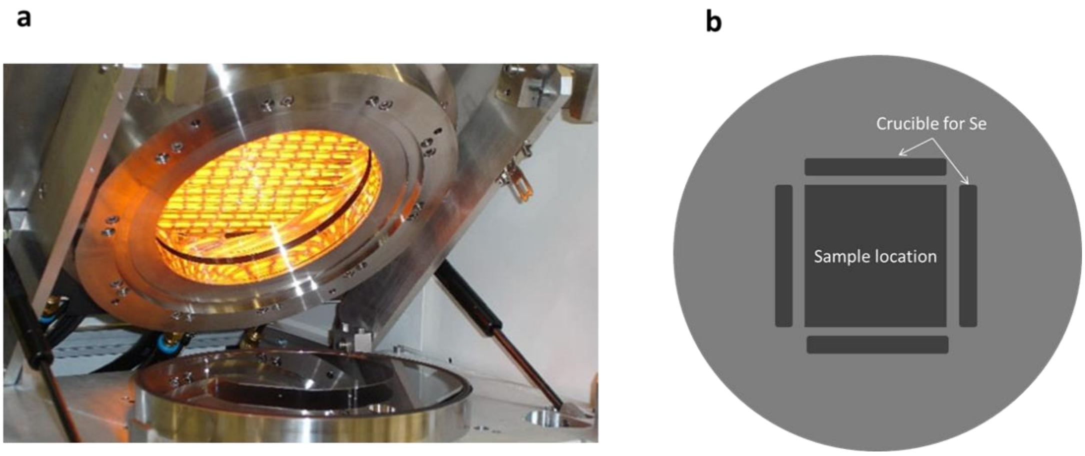

Figure 3.6. a) Picture of the “Annelasys As-one”, rapid thermal processor. Image taken from www.annealsys.com. The susceptor shown in the photograph is not the one used in these experiments b) Schematics of the top view of an open graphite reactor indicating the locations of the sample and the crucibles were the Se pellets are located.

In this case, the Se was supplied in pellets that were located around the sample as shown schematically in the diagram of figure 3.6.b. Four Se pellets were used for each selenisation process presented in chapters 7 and 8. The average weight of each Se pellet was approximately between 60-70 mg. Therefore, in each selenisation process with this method the total amount of Se introduced in the graphite reactor was around 250 mg. The lid of the graphite reactor (not represented in figure 3.6) is fixed with screws, minimising the leakage of vapour inside the reactor and therefore, increasing the partial pressure of Se during the heating treatment.

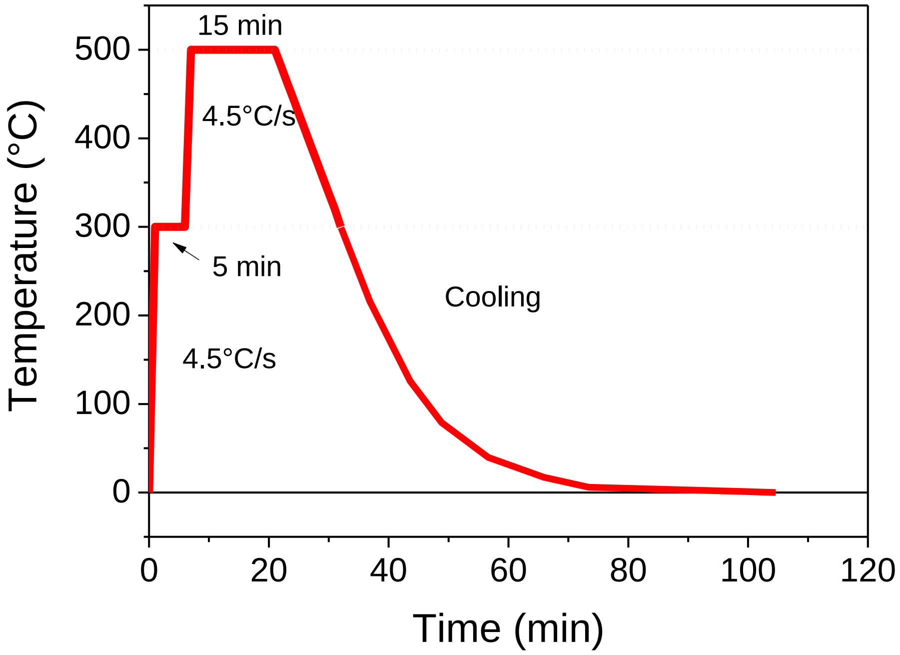

Figure 3.7. Example of heating profile of a typical selenisation process used for the synthesis of the CZTSe absorbers discussed chapters 7 and 8 using the RTP system.

An example of a temperature profile process used for the synthesis of CZTSe discussed in chapter 7 is shown in figure 3.7. In chapter 8, the maximum temperature of the process was studied, and temperatures of 450, 500 and 550 ºC were tested. The temperature profile shows a 5 minutes' step at 300 ºC. This step is kept constant in all the processes. One of the reasons for introducing this first step is because the manufacturer of the rapid thermal processor recommends having a low temperature step in the processes. The second reason is to introduce a temperature above the melting point of Se (217 ºC). This allows the Se to be melted and distributed more uniformly in the crucible rails shown in the scheme of figure 3.6.b. The cooling step shown in figure 3.7 is representative and the values are approximated.

3.4 Buffer layer

In this project, CdS was used as the buffer layer for all the solar cells fabricated. A chemical bath deposition (CBD) method was used to deposit an approximately 50 nm thick CdS layer on top of the absorber layers. All the CZTSe absorber layers were etched in a 10 wt% KCN aqueous solution for 30 seconds prior to the CBD process. The CBD process was at 70 ºC in a jacketed beaker heated with water. 0.028 M of cadmium acetate and 0.374 M of thiourea were used as the Cd and S sources respectively in an ammonium hydroxide solution. The samples were immersed in the solution for 22 minutes before being rinsed with abundant DI water. Further information regarding this process can be found elsewhere [8].

3.5 Front contact

After the chemical bath deposition, a transparent bilayer of ZnO and aluminium doped zinc oxide Al:ZnO was deposited by RF magnetron sputtering [99]. All the CZTSe solar cells were mechanically scribed to produce individual cells of 0.09 cm^2 in area. The CTS solar cells studied in chapter 9 had an area of 0.5 cm^2 and a Ni/Al/Ni grid was evaporated on top of them.

3.6 Coevaporation of Cu-Sn-S absorber layers

The synthesis of absorber layers for thin film solar cells by coevaporation methods is commonly used, particularly in CIGS technology, where the most efficient devices have been synthesised by this method [30]. Also for CZT(Se,S) there are reports by several groups of solar cells using this synthesis methods, i.e. [69, 100, 101].

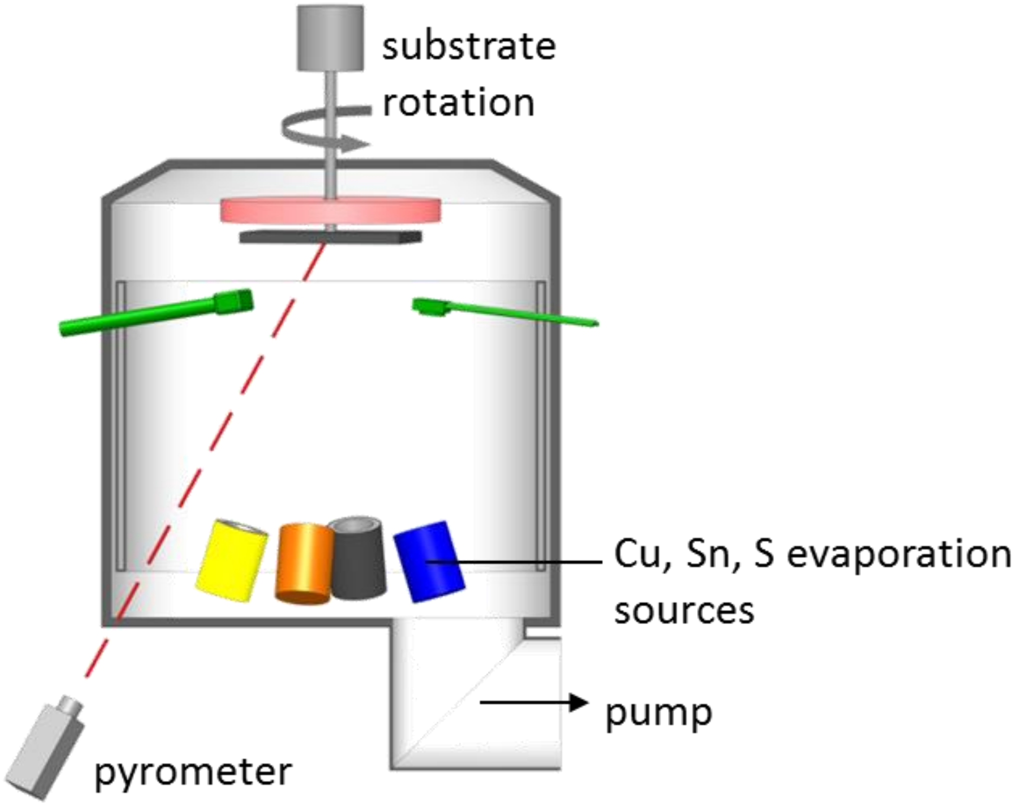

Figure 3.8 Schematic diagram of the coevaporation chamber used for evaporating the Cu-Sn-S absorber layers discussed in chapter 9. Adapted from [102].

CTS absorber layers were deposited using a PVD system equipped with elemental Sn and Cu thermal evaporation sources and a S evaporator with a cracking unit. Molybdenum coated soda-lime glass substrates were used. A sketch of the PVD chamber used for the synthesis of the CTS layers is shown in figure 3.8. The total pressure of the chamber during the deposition was around 1.5×10^{-3} Pa (1.1×10^{-5} Torr). For all the depositions the substrate temperature was set to a nominal temperature of 400 °C. Infrared reflectometry was used for in situ process control. The temperature of the Cu and Sn source and S cracking unit were 1285, 1295 and 500 °C respectively. The deposition was stopped after achieving a layer thickness of approximately 1 μm. More details about coevaporation of CZTS using a similar process have been described in the literature [100].

The evaporation of the CTS absorbers was performed with the help of Lars Steinkopf from the Helmholtz Zentrum Berlin (HZB).

4 Characterisation techniques and analysis methods

This chapter describes the main characterisation methods used for assessing the properties of the CZTSe and CTS absorber layers and solar cells reported in this thesis. It includes a description of the experimental setup used for the measurements with each techniques and a brief description of the methods used for the analysis of the data obtained. Where applicable, the contributions of different colleagues to each measurement or analysis have also been indicated.

Part of the research of this project was carried out in different centres apart from Northumbria University within the frame of the KESTCELLS project including:

- Catalonia Institute for Energy Research (IREC), C. Jardins de les Dones de Negre 1, 08930 Sant Adrià del Besòs, Barcelona, Spain
- Helmholtz-Zentrum Berlin (HZB) for Materials and Energy, Hahn-Meitner-Platz 1, 14109 Berlin, Germany
- Empa – Swiss Federal Laboratories for Materials Science and Technology, Laboratory for Thin Films and Photovoltaics, 8600 Dübendorf, Switzerland

This explains why certain measurements like Raman spectroscopy were performed with different systems as described in this chapter.

4.1 SEM and EDX

The microstructure and composition of the metallic precursors and the absorber layers were analysed by scanning electron microscopy (SEM) using a FEI Quanta 200 microscope equipped with an Oxford Instruments energy dispersive X-ray analyser (EDX). For the composition measurement 20 kV was used as the acceleration voltage corresponding to a penetration depth of approximately 1.2 µm. The cross section image of the CTS solar cell in chapter 9 was acquired by Justus Just from the Helmholtz Zentrum-Berlin with a LEO 1530 GEMINI SEM of Zeiss.

4.2 X-ray fluorescence (XRF)

X-ray fluorescence was used to measure the composition of metal ratios using an operating voltage of 40 kV with a rhodium anode. The XRF system was calibrated with reference samples measured by inductively coupled plasma mass spectroscopy (ICP-MS, Agilent 7500ce). The reference samples were prepared with powder from absorber layers carefully scratched from the Mo substrates. The powder was dissolved in concentrated HNO_3 in a gas tight polyethylene vessel. The calibration of the ICP-MS equipment was performed with certified elemental standards with an error of ±10%.

4.3 X-ray diffraction

X-ray diffraction is possibly one of the most important characterisation techniques used for the development of this thesis. Therefore, this section presents a detailed description of the theory and analysis of the data acquired using this technique.

The samples presented in this thesis have been measured with a Siemens D-5000 diffractometer in the Bragg-Brentano geometry and with a PANalytical X'Pert MPD Pro X-ray diffractometer in grazing incidence configuration. Both diffractometers operate with a Cu Kα radiation source (λ=0.154059 nm). The measurements with the Siemens D-5000 have been carried out with a voltage of 40 kV and current of 40 mA. The PANalytical X'Pert MPD Pro X-ray diffractometer was operated with a voltage of 40 kV and a filament current of 30 mA.

In both systems, the X-rays are directed through a Ni filter in order to attenuate the Cu Kβ radiation. In the case of the PANalytical, the Ni filter was allowed to attenuate the 99% of the Kβ radiation. However, in the case of the diffractograms recorded with the Siemens D-5000 it was possible to see that the most intense peaks of the patterns had a replica due to the Cu Kβ radiation, since in this system, the Ni filter was not able to block it completely.

In this part, the principle of characterization by X-ray diffraction will be briefly explained. The two different configurations that have been used to measure the samples of this thesis, Bragg-Brentano and Grazing Incidence are also explained in this part. Finally, the principles of the analysis of the data acquired by this method are also explained.

4.3.1 X-ray diffraction theory

In order to understand the basic phenomenon of the principle of the technique, it is necessary to consider the interaction of X-rays in the relevant energy range with matter. There are three different types of interaction between X-rays and electrons [103]:

- Electrons can be liberated from their bound atomic state in a process of photoionisation, where the energy and momentum of the radiation are transferred to the excited electron. This is an inelastic scattering process.
- In Compton scattering, the radiation energy is also transferred to an electron which in this case is not released. The wavelength of the scatter light is different of that of the incident radiation. This is also another inelastic scattering process.

- X-rays can be elastically scattered by electrons. When this occurs, the electron oscillates at the frequency of the incoming beam becoming a source of dipole radiation. This type is called Thompson scattering and the wavelength λ of the incoming X-ray radiation is conserved in the scattering process. This type of scattering of X-rays is the one that we make use of for structural investigation by X-ray diffraction [103].

When the incident X-ray impacts the electrons, the energy of the elastically scattered X-rays is equal to the energy of the incident beam, but the intensity is determined by the electron density of the scattering centres, therefore by the atoms in the lattice. A signal in terms of a diffraction patterns is detected only if the electron density centres (atoms) are located in a periodic manner, which is the definition of a crystalline material.

When an X-ray radiation hits an atomic plane in a crystalline material with an incident angle θ, a fraction of this radiation is elastically reflected without changing the wavelength, λ. Then, the angle of the incident radiation and the reflected radiation is equal. Part of this incoming radiation can be transmitted and then can be reflected at a second plane of atoms, as shown in figure 4.1, and so on for further planes of atoms. If the path difference, L, of the reflected beam in lattice plane array is equal to an even multiple (n) of the wavelength λ, where d is the inter-planar distance, then constructive interference occurs. This representation of the diffraction phenomenon was presented by W. L and W. H Bragg in 1913, which is mathematically represented in equation 4.1, and it is known as the Bragg law [104].

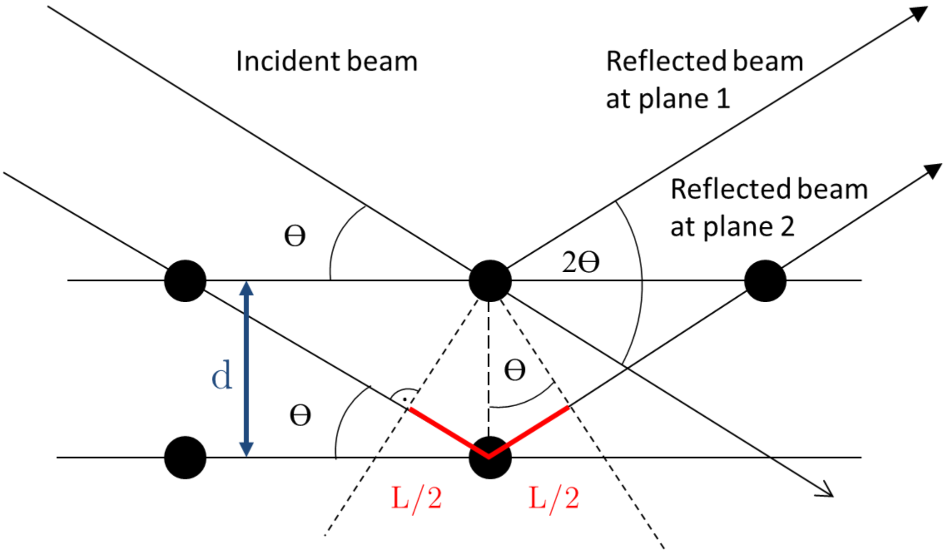

Figure 4.1. Diagram illustrating the Bragg law

$$L = n \cdot \lambda = 2 \cdot d \cdot sin\theta \qquad 4.1$$

The diffraction angle θ of the reflection depends on the crystal lattice. Taking into account also the distribution of the intensities of the reflected radiation and its dependence with the angle θ, the crystal structures can be determined.

4.3.2 Bragg-Brentano geometry

The Bragg-Brentano X-ray diffraction (BBXRD) configuration is commonly used for characterising powder samples. In this type of measurement, both, the X-ray source and the detector move at the same angular speed changing the incidence and diffracted angle that coincide at every point in the measurement. This is represented in figure 4.2. Because of the characteristics of this type of geometry, just the family of planes that are parallel to the surface of the sample are measured. One of the most positive characteristics of this type of measurement is its speed. The diffractograms for this thesis with this configuration using the Siemens D5000 system were recorded in 2.5 hours and the ones presented in the chapter 9 recorded with the PANalytical system took around 40 minutes each. The diffractograms recorded in grazing incidence (GI) configuration took 17 hours each, making BBXRD a more practical measurement for phase identification, which can be performed using both types of geometries. In contrast, when data for an accurate depth resolution and greater surface sensitivity is required, GI configuration is needed, as discussed in the next section. In addition to the speed advantage, BBXRD offers the possibility of having qualitative information regarding the preferred orientation along the z-axis due to the fact that the lattice planes measured are parallel to the surface of the film.

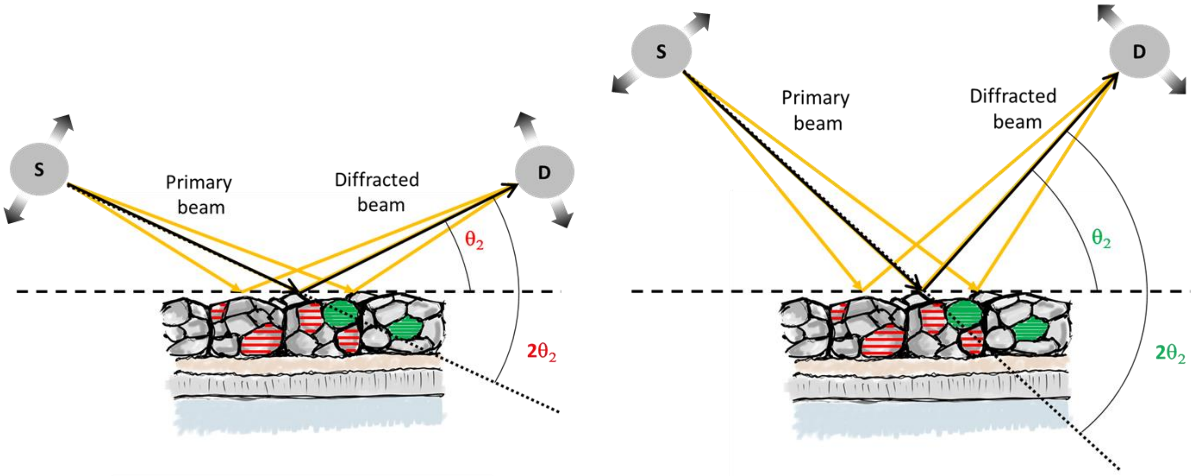

Figure 4.2. Simplified diagram representing a Bragg Brentano measurement in a polycrystalline CZTSe absorber layer on a SLG/Mo/MoSe$_2$ substrate. Both, the X-ray source (S) and the detector (D) move at the same angle speed. Because of the position of the detector is always given by 2*θ* the parallel planes to the surface of the films are the only ones detected. As the *θ* varies, different families of planes with different interplanar (*d*) distances are detected.

4.3.4 Grazing incidence geometry

The grazing incidence X-ray diffraction (GIXRD) configuration is possibly the most suitable configuration for accurate analysis of thin films. In this case, and the main difference with the BBXRD, is that the incidence angle of the X-ray source (ω) is fixed, and the detector is moving along the 2θ space. By doing so, it is possible to tune the penetration depth of the X-rays within the films and acquire depth-resolved information. In addition, the planes measured with this geometry are no longer parallel to the surface of the sample and change with the variation of the position of the detector as shown in figure 4.3.

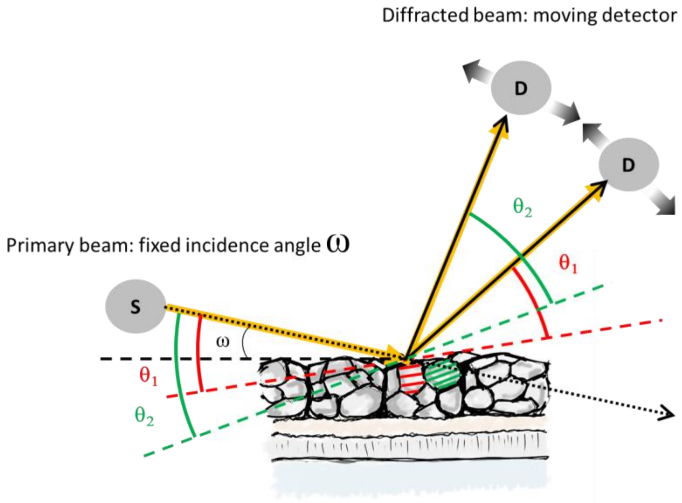

Figure 4.3. Simplified diagram representing a grazing incidence measurement in a polycrystalline CZTSe absorber layer on a SLG/Mo/$MoSe_2$ substrate. The X-ray source (S) remains at a fixed position with an incidence angle ω. The detector (D) moves along the 2θ space.

Normally, the incidence angle used for thin films varies between 0 and 18 º. By increasing the incidence angle, the penetration of the X-rays in the samples also increases. The dependence of the penetration of the X-rays in a CZTSe film have been calculated by Gunder [105]. This allows us to discuss the properties of the CZTSe films in the near surface region, bulk and at the interface with the $MoSe_2$/Mo back contact. This configuration has been used for measuring the samples discussed in chapter 7, at 4 different incidence angles of 0.5, 1, 2 and 5º.

4.3.5 Le Bail analysis

Le Bail analysis is similar to Rietveld refinement and consists of the comparison of the measured data with a given model of the crystal structure of the phases that are analysed with the least square method [106]. By doing so, the difference between the model and the measured data is reduced iteratively until a point where the model fits with great quality. The main difference with Rietveld analysis is that, in the model used to fit the pattern, just the space group of the phases are taken into account and the atomic positions are not considered. This allows the model to fit the intensities of the experimental patterns providing an accurate refinement that allows a good microstructural analysis, as discussed in the next part.

Two indicators of the quality of the refinements are typically the Bragg value R_{Bragg} defined in equation 4.2 and X^2 in equation 4.3. The Bragg value is an indicator of the agreement of the phases used to fit the pattern, were I_{obs} represents the intensity of the experimental patterns in each data-point recorded (h) and I_{calc} the intensity of the refined model. The X^2 stands for the quality of the pattern as a whole and is defined as the ratio between the weighted profile R-factor (R_{wp}) and the expected R factor (R_{exp}) which stands for the best possible R_{wp} value [107]. The X^2 and the R_{Bragg} will be evaluated and used for the Le Bail refinements processed in the GIXRD patterns of the samples discussed in chapter 7.

Le Bail analysis was performed with WinPlotR software from the FullProf Package [108]. Analysis and comparison of the phases in this thesis have been performed with Powdercell software using powder diffraction data from the ICSD [109]. After having an accurate estimation of the phases measured in the samples, then the structural parameters can be introduced in order to perform the Le Bail analysis.

$$R_{Bragg} = 100 * \frac{\sum_h \left| I_{obs,h} - I_{calc,h} \right|}{\sum_h \left| I_{obs,h} \right|} \quad 4.2$$

$$X^2 = \left(\frac{R_{wp}}{R_{\exp}} \right)^2 \quad 4.3$$

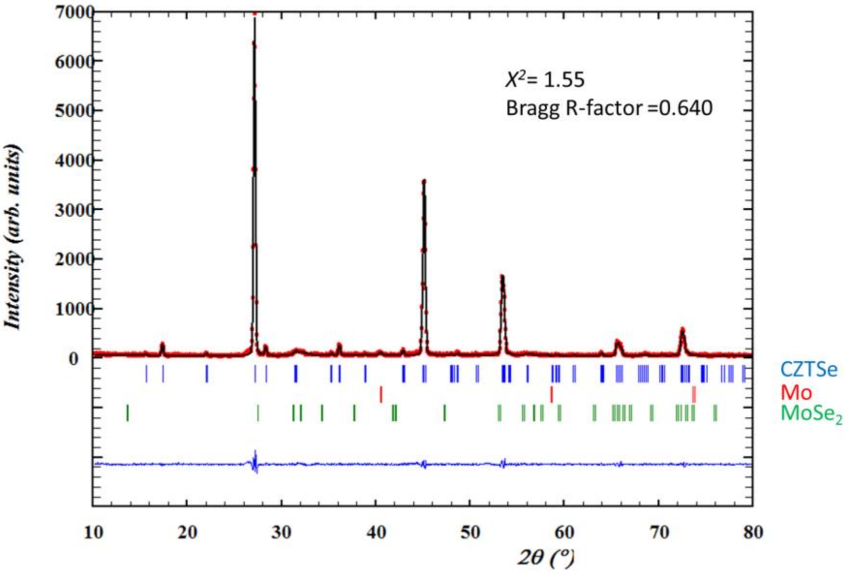

Figure 4.4. Le Bail analysis of a SLG/Mo/MoSe$_2$/CZTSe sample recorded with an incidence angle of 2º.

An example of a Le Bail refinement in one of the samples discussed in chapter 7 can be found in figure 4.4. The red dots represent the measurement of the pattern, and the black line represents the model fitted to the patterns. The blue line represents the difference between the fitted model and the experiment. In this case, three phases have been considered to fit the model including Mo, $MoSe_2$ and CZTSe. The positions of the reflections of the CZTSe, Mo and $MoSe_2$ can be seen in blue, red and green below the pattern. Once the model is in close agreement with the experiment, then an accurate estimation of the lattice parameters can be obtained. Because the shapes of the peaks are accurately fitted, this allows a good microstructural analysis as explained in the following subsection.

4.3.6 Microstructural analysis

In chapters 5 and 6, the microstructural analysis has been performed with the software Powdercell, after Le Bail analysis has been performed.

Microstructural analysis can provide interesting information about the polycrystalline films that were measured by XRD methods. To do so, one needs to be consider that the broadening of the peaks are due to micro-strain and a small average value of domain size. The broadening of the peaks can be expressed mathematically as the integral breadth β. The integral breath is calculated as a ratio between the integral intensity and the full width at the half of the maximum (FWHM) of the peak. In order to have a clearer understanding the information that it can be obtained from the analysis of our patterns with regards to the microstructure of the films analysed, the different type of strains are illustrated in figure 4.5 and described in the text below.

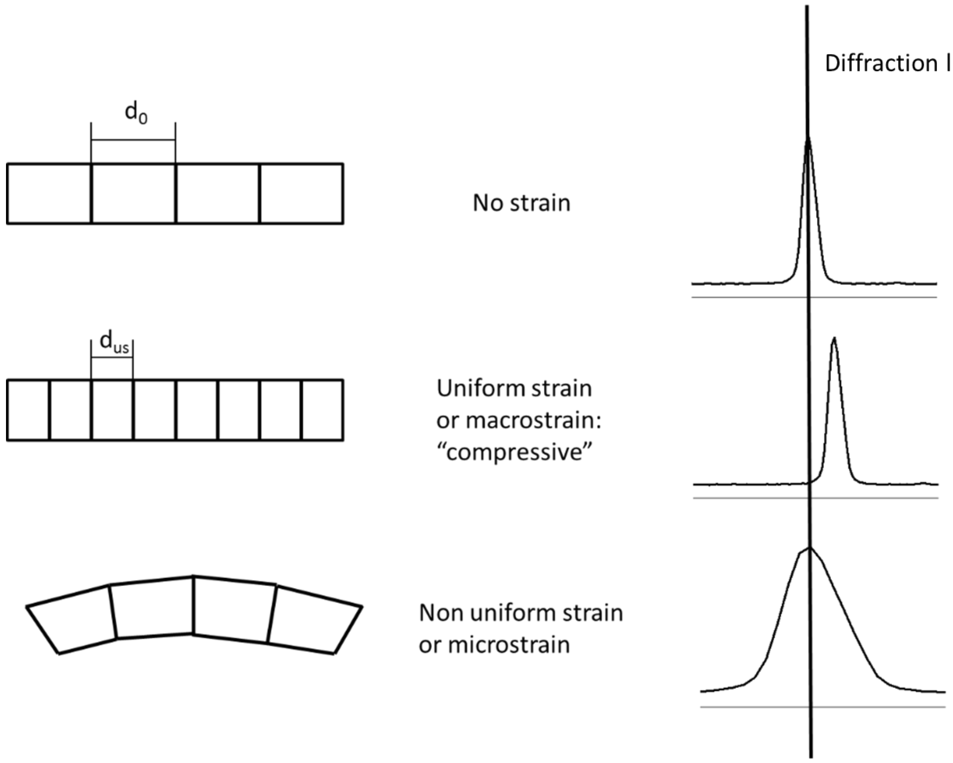

Figure 4.5. Schematics of different type of strain in the lattice and its influence on the peaks observed in the experimental diffractograms.

- **Strain free:** the Bragg peak appears at the position corresponding to the original interplanar distance d_0.
- **Uniform strain or macro-strain:** uniform strain can be created by a force applied to the lattice inducing its interplanar distance to vary uniformly in the whole crystal lattice. If the force is compressive and perpendicular to the planes, then the interplanar distances would uniformly decrease and the Bragg peak will appear at higher angles. If the force is under tension, then the opposite will occur.
- **Non-uniform strain or micro-strain:** micro-strain in the lattice could be induced by several factors, like planar defects, point defects such as vacancies or antisite disorder. In general terms, micro-strain is induced by the displacement of the atoms from their ideal positions resulting in

non-uniform values of *d* in the lattice that leads to a broadening of the observed peaks.

After fitting the experimental patterns to a model with Le Bail analysis, information about the shape of the peaks of the whole pattern is acquired, and thus, the integral breadth of them. With the values of the integral breadth, now the domain size and micro-strain can be calculated.

The broadening due to domain size can be expressed by the Scherrer formula in equation 4.4 [110], where λ is the wavelength of the X-rays, D is the volume averaged domain size and K_S is the Scherrer constant. At this point, it is important to point out that domain and grain size do not necessarily have to be the same thing. Domain is defined as a particular crystallite or a particular grain where the 3D is perfectly periodic (coherent). Within a grain, this periodicity can be interrupted by imperfections such as stacking faults or dislocations, making the grain size larger than the domain size. Larger domains than 100 nm do not contribute a significant amount to incoherent scattering and then the broadening of the peaks due to size when the patterns are measured with a standard diffractometer cannot be resolved.

$$\beta_{size} = \frac{K_s \lambda}{D\ cos\ \theta} \qquad 4.4$$

The broadening due to micro-strain can be calculated with the Wilson relation shown in equation 4.5, where ε the average micro-strain value and K_D is the scaling factor that depends on the nature of the lattice distortion [103]:

$$\beta_{strain} = 2K_D \varepsilon \tan\theta \qquad 4.5$$

By adding both equations it is possible to obtain the total broadening of the peak, having previously subtracted the instrumental broadening:

$$\beta_{2\theta} = \frac{K_s\lambda}{D\ cos\ \theta} + 2K_D\varepsilon \tan\theta \tag{4.6}$$

Multiplying both sides of the equation by cos θ/λ it is possible to obtain the Williamson-Hall linear relation:

$$\frac{\beta_{2\theta}\ (cos\ \theta)}{\lambda} = \frac{K_s}{D} + K_D\varepsilon\frac{2\sin\theta}{\lambda} \tag{4.7}$$

By plotting $\beta_{2\theta}\ cos\ \theta$ vs $2\ sin\theta/\lambda$ it should be possible to obtain a straight line where the domain size can be extracted from the intercept and the micro-strain can be determined from the slope. This is known as the Williamson-Hall plot [111]. The values obtained in chapters 5 and 6 have been calculated automatically with the Williamson-Hall plot with the Powdercell software, after performing Le Bail analysis. The instrumental broadening could not be measured and it could not be subtracted from peak broadening. Therefore, the microstrain values presented in this thesis should just be compared qualitatively.

4.4 Raman Spectroscopy

Raman spectroscopy is based on the measurement of the scattered light from a material. A sample is excited with a monochromatic light beam. This light is mainly elastically scattered (Rayleight scattering), but can also interact with the crystal lattice of a material and be scattered inelastically, decreasing its energy (Stokes) or increasing its energy (anti-Stokes). The energy shift in the inelastic scattering process is that involved in the photon-phonon interaction [112]. The measurement of the energy of the scattered light from a sample allows the building of a Raman spectrum. From this spectrum a large amount of information can be extracted from a sample such as the phases contained in it [113], the crystal structure [114], chemical composition [115] and even information about the defects present in the crystal lattice [58, 116, 117].

The Raman spectra analysed in chapters 5 and 6 were recorded by Jonathan Scragg at Uppsala University with a Renishaw inVia system using 532 nm excitation wavelength. The Raman spectra presented in chapters 7 and 8 were recorded by Mirjana Dimitrievska at IREC with 532 nm excitation using a LabRam HR800 -UV spectrometer. Finally, the spectrum discussed in chapter 9 was measured by Sergej Levcenko at HZB. These Raman scattering measurements were performed with He-Ne laser (633nm) excitation using an Andor spectrometer (SR-500i-D2) and CCD detector (Princeton Instruments 100Br Excelon). The different measurements were a result of collaborations with the groups of the KESTCELLS project.

4.5 Current density - Voltage (J-V)

Insight into the electronic transport of solar cells can be acquired by measuring their J-V characteristics under illumination and in the dark. To measure the solar cells under standard test conditions the illumination source should match the AM 1.5G solar spectrum [118]. Since the solar cell parameters are influenced by the temperature, during the measurements the sample is kept at 25 ºC to meet standard conditions.

A typical J-V curve of a CZTSe solar cell is shown in figure 4.6. In the figure, the points can be identified and can be used to describe some of the characteristics of the solar cells:

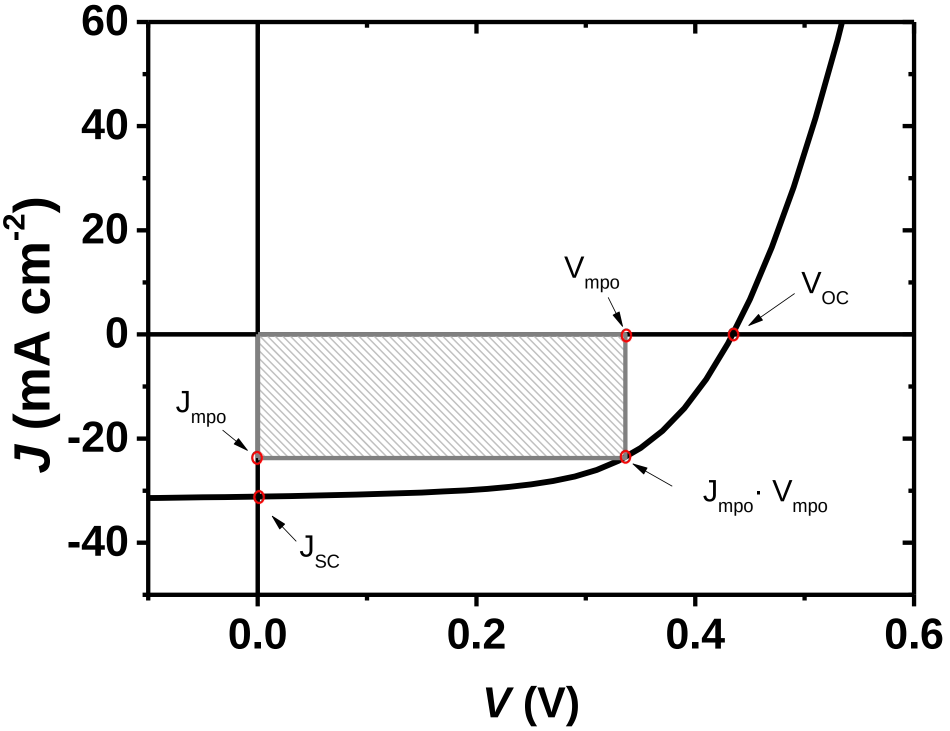

Figure 4.6. Example of a J-V curve of a CZTSe solar cells indicating relevant points to identify the characteristics of the device.

- The open circuit voltage V_{OC} is the voltage when the total current density is equal to zero
- The short circuit current density J_{SC} is defined as the current per unit area when there is no bias voltage applied to the solar cell.
- When the product of J·V is maximum in the fourth quadrant, this defines the maximum power output of the solar cells (J_{mpo}, V_{mpo}).

The maximum achievable power point of a solar cell is limited by the values of J_{SC} and V_{OC} as shown in equation 4.8.

$$P_{max} = V_{OC} J_{SC} \quad 4.8$$

This represents an ideal limit that is never achieved in reality. To define the proximity of the real J-V curve to the theoretical limit the parameter called fill factor is introduced (FF). This parameter defines the 'squareness' of the J-V curve.

$$FF = \frac{V_{mpo}J_{mpo}}{V_{OC}J_{SC}} \qquad 4.9$$

The main figure of merit of the solar cell is the conversion efficiency (ŋ) which can be calculated as the ratio between the maximum power output and the power density of the incident radiation (P_i) which in the case of the standard test conditions is equal to 1000 W/m^2.

$$\eta = \frac{V_{mpo}J_{mpo}}{P_i} = FF\,\frac{V_{OC}J_{SC}}{P_i} \qquad 4.10$$

The J-V characteristics of the solar cells of this thesis have been measured with a class A solar simulator under 1000 W/m^2 AM 1.5G simulated illumination with a HMI light source. The system was calibrated with a certified monocrystalline Si reference solar cell from Fraunhofer ISE. The samples were contacted in the front of the solar cells directly on the TCO since a metallic grid was not evaporated on them. The back of the samples was contacted by probing silver paste on the Mo layer. The measurements were performed in a 4-point contacting mode with a Keithley 2400 source meter.

4.6 Quantum Efficiency (QE)

Ideally, the photons arriving at the absorber layer with energy larger than the bandgap generate electron hole-pairs than can be collected at either the back or front contact of the device. However, due to a number of different factors, the ratio of collected electrons (and holes) per time is reduced by means of recombination or optical losses. These losses limit the maximum achievable photocurrent density reducing the J_{SC} of the solar cells.

The ratio of the collected electrons per time $J_{ph}(\lambda_{ph})$ per incident photons $\Phi(\lambda_{ph})$ with certain energy can be measured by the external quantum efficiency (EQE).

$$EQE\left(\lambda_{ph}\right) = \frac{1}{q}\frac{J_{ph}\left(\lambda_{ph}\right)}{\Phi\left(\lambda_{ph}\right)} \qquad 4.11$$

By integrating the EQE spectrum with the AM 1.5G illumination spectrum, it is possible to obtain a value for J_{SC} from another characterisation technique to compare with the one that was measured in the J-V curve.

$$J_{SC} = q \int EQE(\lambda)\Phi(\lambda)d\lambda \qquad 4.12$$

Optical losses can affect significantly the shape of the EQE. These could arise, for example, due to reflection of light from the TCO, or the layers above the absorber layer. If the reflectance of the solar cell is known, then the EQE can be corrected and one can calculate the internal quantum efficiency (IQE), which refers to the ratio of the collected electrons per time per absorbed photon. This will be used to identify the origin of a kink feature observed in the EQE spectrum discussed in chapter 9.

The bandgap (E_g) of the absorber layer can be extracted from the low energy part of the EQE. In literature, several methods for extracting the value of E_g have been used for kesterite solar cells [119].

For an ideal p-n junction, the EQE can be dependent on the absorption coefficient (α), the space charge region width (W) and the minority carrier diffusion length (L_n) as shown in equation 4.13 [120]:

$$EQE = 1 - \frac{\exp(-\alpha W)}{1 + \alpha L_n} \qquad 4.13$$

Assuming a very short diffusion length of the minority carriers the expression can be simplified to equation 4.14:

$$EQE = 1 - \exp(-\alpha W) \qquad 4.14$$

For direct bandgap semiconductors the dependence of the absorption coefficient on the energy of the photons is described by equation 4.15

$$\alpha h\nu \propto \left(h\nu - E_g\right)^{1/2} \qquad 4.15$$

Therefore, plotting $[h\nu * \ln(1 - EQE)]^2$ vs $h\nu$ can be used to extrapolate the E_g. Examples of this method to extrapolate the bandgap from the EQE can be found in literature for the materials studied in this thesis, i.e. [19, 47].

In recent years it became very popular to calculate the bandgap from the EQE from the inflection point of the low energy decay of the spectrum [121]. This has been reported to provide a more robust way to calculate the bandgap than the method previously described in this section [121]. The calculation of the bandgap from this derivative method normally leads to larger values and depends on the steepness of the decay of the EQE at long wavelength.

The EQE of the solar cells presented in chapter 7 have been measured using a lock-in amplifier and a chopped white light source (900W, halogen lamp, 360Hz) combined with a grating monochromator calibrated with Si and Ge diodes. The EQE of the CTS solar cell presented in chapter 9 has been measured without white light bias and with a lock-in amplifier combined with a 1/4m Oriel monochromator.

4.7 Capacitance -Voltage (C-V)

Capacitance - voltage profiling is commonly used to characterise the charge carrier concentration one-dimensional profile in thin film solar cells. The capacitance, represents the change in charge induced by a small change in the voltage $C = \delta Q/\delta V$.

To estimate the charge carrier concentration from C-V measurements two main assumptions need to be taken [122]:

1. The space charge region (SCR) ends abruptly and it is fully depleted of carriers, so called the depletion approximation.
2. The region outside the SCR is assumed to be neutral.

The application of a small voltage δV will induce charging/discharging δQ at the edge of the SCR and it is defined by equation 4.16:

$$\delta Q = q \cdot A \cdot N_A \cdot \delta W \qquad 4.16$$

Where A is the area of the device, q is the elemental charge, N_A is the shallow acceptor concentration and δW is the change in the SCR width.

By applying an additional bias voltage, the SCR width increases as the voltage is in reverse on the side of the junction with lower doping concentration, which in the case of this thesis will always be the absorber layer. Measuring the capacitance by sweeping the bias voltage applied δV_{dc} the 1D profile of the charge carrier concentration N_{CV} can be obtained according to equation 4.17 where ϵ is the dielectric constant of the material and ϵ_0 is the permittivity of the vacuum.

$$N_{CV} = -\frac{2}{q\epsilon\epsilon_0 A^2}\left(\frac{d(C^{-2})}{dV_{dc}}\right)^{-1} \qquad 4.17$$

A more detailed theoretical description of this principle has been described by Heath and Zabierowski [122], where all the theory and details of this measurements for thin film solar cells are described.

Capacitance-Voltage measurements have been performed by Dr. Sergej Levcenko from HZB in the CTS device presented in Chapter 9. The measurements were performed with an HP4284 LCR meter and four-point probes.

4.8 Photoluminescence (PL)

For the photoluminescence analysis of thin films semiconductors, normally, a laser is used as an excitation source. The excitation source is focused into the sample. By this excitation, the samples emit luminescence radiation that is collected and guided through a filter that allows removal of unwanted radiation of higher order. The luminescence light is guided into a monochromator. After leaving the monochromator, the luminescence light reaches a radiation detector. Different transitions can be detected in PL measurements. The different transitions can be distinguished as a function of the excitation intensity and temperature. For temperature variation measurements, the samples are normally place in a cryostat. More information about the photoluminescence principle, and measurements in thin film solar cells can be found in detail elsewhere [123].

In chapter 8, the radiative recombination of the absorber layers presented has been studied by photoluminescence methods and is compared to the compositional and structural data of this set of samples. This allowed a better understanding and correlation with the optoelectronic properties of the solar cells, with CZTSe absorber layers synthesised at different temperatures. In addition to this, the identification of the different transitions observed in the PL spectra are analysed and discussed.

The photoluminescence data has been measured by Dr. Michael Yakushev from the University of Strathclyde at Glasgow. A 1 m focal length single grating monochromator and the 514 nm line of a 300 mW Ar+ laser were used for the photoluminescence (PL) measurements. A closed-cycle helium cryostat was employed to measure temperature dependence of the PL spectra at temperatures from 6 K (-267.15 ^{o}C) to 300 K (26.85 ^{o}C). The PL signal was detected by an InGaAs photomultiplier tube sensitive from 0.9 µm to 1.7 µm. The preliminary analysis of the PL data has been performed also by Dr. Michael Yakushev and co-authors as indicated in the introduction of this thesis. The discussion of the results and the correlation with the structural properties of the CZTSe absorbers and the optoelectronic properties of the solar cells has been performed in collaboration with the author of this thesis.

5 The formation of CZTSe by two-stage process

The aim of this chapter is the exploration of the formation of the CZTSe layer from Cu-Zn-Sn metallic precursors via the two stage synthesis method. For a better understating of the evolution of the phases during the growth of the CZTSe, the selenisation of Cu-Zn and Cu-Sn alloys, formed in the Cu-Zn-Sn metallic precursors, is also explored for a wide range of temperatures as explained in the specific experimental details. The results and discussions are presented in this chapter in three subsections. Subsequently, the role and use of an evaporated cap in the selenisation process is discussed, leading to the final section of the chapter, where the main conclusions are addressed. The development of this study allowed a deeper insight into the growth of the CZTSe and helped addressing the limitations of the process used for the selenisation of the metallic precursors used in this thesis.

This chapter is in part based on the following publications:

J. Márquez-Prieto and I. Forbes, "Evolution of Phases in Two Stage Vacuum Processed Thin Film $Cu_2ZnSnSe_4$ Absorber Layers," *Materials Research and Innovations,* 2014.

J. Márquez-Prieto, Y. Ren, R. W. Miles, N. Pearsall, and I. Forbes, "The influence of precursor Cu content and two-stage processing conditions on the microstructure of $Cu_2ZnSnSe_4$," *Thin Solid Films,* vol. 582, pp. 220-223, 2015.

5.1 Motivation and state of the art

In this chapter, CZTSe kesterite films are produced using a 2-stage process. Sputtered metallic precursor layers of Copper, Zinc and Tin were synthesised. These layers have a chalcogen (Se) layer thermally evaporated on to their surface before they were placed in a graphite box to be heated in a furnace to convert the metallic layers into a semiconducting absorber as explained in chapter 3 section 3.3.1.

The conversion step is a key process for the formation of device-quality absorber layers. During conversion, various phases have been identified in the literature as taking part in kesterite formation. The narrow stoichiometric region of kesterites implies that different secondary phases can also be formed during the growth of the absorber layers, this being partly dependent on the composition of the precursors used [36, 62, 124]. Decomposition at the surface of the CZT(S,Se) films [125] and at the interface with the Molybdenum back contact [73, 91] has been reported as another source of secondary phases.

The sputtered metallic precursors used for synthesizing kesterite absorbers in this thesis are mainly formed from Cu-Zn and Cu-Sn alloys as for previous work carried out at Northumbria University [72]. The microstructure of the precursors and their variation with the Cu content are studied in chapter 6 section 6.3.1. In order to provide a brief summary, the most typical secondary phases to be formed from each phase or alloys forming the metallic precursors are compiled in table 5.1.

The formation of CZTSe and secondary phases can be controlled by varying the process conditions as is partly covered in this chapter, and also by variations in the composition of the precursors as discussed in chapters 6 and 7. To minimise the formation of secondary phases and to gain a greater degree of control over kesterite formation, a greater understanding of the relationship between the phase evolution process and processing conditions is needed in order to be able to improve the design of the synthesis process of CZTSe to achieve device quality absorber layers.

Table 5.1. Possible secondary phases formed after the selenisation of Cu-Zn-Sn metallic precursors. The phases in the precursors associated with each metal are also indicated taken into account the formation process of CZTSe reported by Wibowo et al. [126].

Metal contained in the secondary phase	Possible phase in the precursor	Secondary phase compound
Cu	Cu, Cu-Sn alloy, Cu-Zn alloy	Cu_2Se, CuSe, $Cu_{1.8}Se$
Zn	Cu-Zn alloy	ZnSe
Sn	Sn, Cu-Sn alloy	SnSe, $SnSe_2$
Cu,Sn	$Cu_{2-x}Se$, SnSe, $SnSe_2$	Cu_2SnSe_3

For the synthesis of device quality CZTSe, it is crucial to avoid certain secondary phases, particularly the ones with bandgap narrower than the kesterite phase, which if located in the p-n junction interface, would be likely to induce a bandgap reduction and therefore reduce the maximum achievable V_{OC} of the solar cell [36]. Bearing this in mind, for CZTSe the most detrimental phase to be avoided is Cu_2SnSe_3 (CTSe), with a bandgap of 0.5 eV [54]. The role of several secondary phases such as copper selenide binaries and ZnSe are discussed in the following sections.

Apart from the aim of understanding the detrimental effect of the CTSe phase when it is coexisting in CZTSe absorbers, this ternary compound, as well as its pure sulphide counterpart Cu_2SnS_3, has attracted increased interest in the research community for several reasons. These will be discussed briefly in this chapter and also in chapter 9.

The following sections correlate materials data on the evolution of phases with conversion conditions for the 2 stage process used in this thesis.

5.2 Specific experimental details

In this chapter, the formation of $Cu_2ZnSnSe_4$ absorber layers has been investigated. In order to do so, the selenisation of the Cu-Zn-Sn ternary and together with binary precursors (Cu-Sn, Cu-Zn) has been studied at different conversion temperatures. The specific conditions for the synthesis of the precursors of this chapter are presented in table 5.2.

Table 5.2 Sputtering conditions for the Cu-Zn, Cu-Sn and Cu-Zn-Sn precursors.

	EDX-Precursors	**Deposition time (min)**	**Power (W)**		
Sample	**Cu/(Zn+Sn)**		**Cu target**	**Zn target**	**Sn target**
Cu-Zn	1.9	30	175	70	-
Cu-Sn	2.1	30	175	-	130
Cu-Zn-Sn	0.90	30	175	70	130

The binary precursors Cu-Zn and Cu-Sn were prepared with excess of Cu (Cu/metal~2) to study the phase formation from the Cu-Zn and Cu-Sn alloys.

The precursors were selenised at four different conversion temperatures (380, 430, 520 and 550 ºC). These temperatures were chosen to critically compare with the observed phase transitions in an in-situ study proposing the formation mechanism shown in figure 5.1, from samples fabricated with a similar synthesis approach [126]. The selenisation process was carried out as described in chapter 3 section 3.3.1 in a tube furnace.

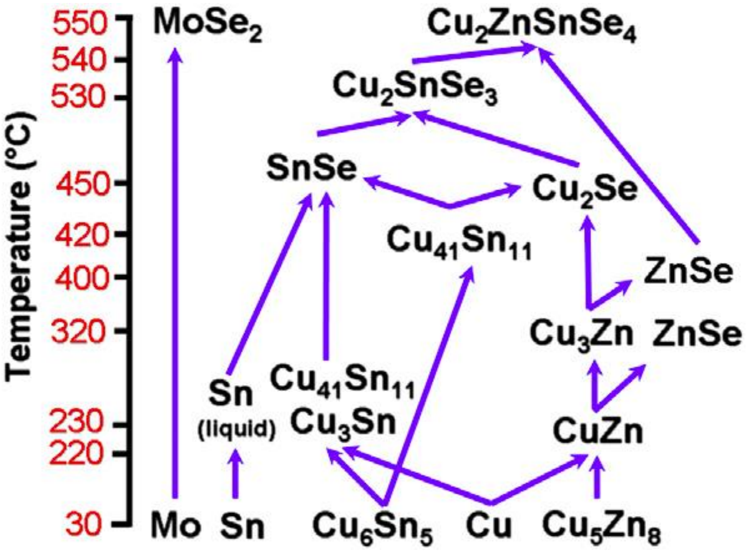

Figure 5.1. Phase evolution proposed by Wibowo et al from Cu-Zn-Sn metallic precursors to CZTSe. (From [126])

The sets of converted precursors were designated as follows: the selenised Copper-Tin samples will be referred to as Cu-Sn-Se, the Copper-Zinc as Cu-Zn-Se and the Copper-Zinc-Tin generally as Cu-Zn-Sn-Se. The binary precursors were produced “Cu-rich” to produce films that were limited by the Zn or Sn content.

5.3 Results and discussion

5.3.1 Conversion of Cu-Zn precursors: formation of $Cu_{2-x}Se$ and ZnSe

Other workers reported studies regarding the selenisation of Cu-Zn-Sn metallic precursors and found that the formation of ZnSe started to be observed at temperatures above 300 ºC [126]. Following the formation of ZnSe, Cu_2Se started to form at about 450 ºC. It was also suggested that these compounds react with Cu_2SnSe_3 to form CZTSe at around 550 ºC [126].

In addition to the information regarding the phases formed from these precursors, it was also important to gather information about their morphology and how they were formed. Copper selenides can be formed at the surface of kesterites as in CIGS absorbers, but these can be removed by a KCN etching prior to the chemical bath deposition of CdS, being a critical step for the final performance of these solar cells [127].

The presence of ZnSe has also been studied in CZTSe solar cells. It has been reported that when ZnSe is present at the surface of CZTSe absorbers this phase may act as a current blocker [128]. NREL reported initially that an excess of ZnSe at the back contact interface would not be as detrimental as at the surface, yielding devices with efficiencies over 9 % with anti-reflecting coating (ARC) [129]. The same group reported later that a controlled excess of Zn at the surface of the CZTSe could induce an increase of the bandgap at the interface leading to an increase of the V_{OC} and performance of the solar cells [85]. A selective etching route for ZnSe has also been developed and can be applied to CZTSe [64]. As for copper selenide phases, this chemical etching could be an effective and beneficial process to enhance solar cell performance as long as the phases are segregated towards the surface. If the secondary phase connects the front and back of the absorber, etching could lead to pinholes that would be detrimental to the solar cell performance. In fact, in CZTSe films from electrodeposited metallic precursors, ZnSe segregation was observed towards the surface but created voids underneath its location [130].

5.3.1.1 XRD of Cu-Zn-Se films

Figure 5.2 shows the diffractograms acquired for the films resulting from the selenisation of Cu-Zn precursors.

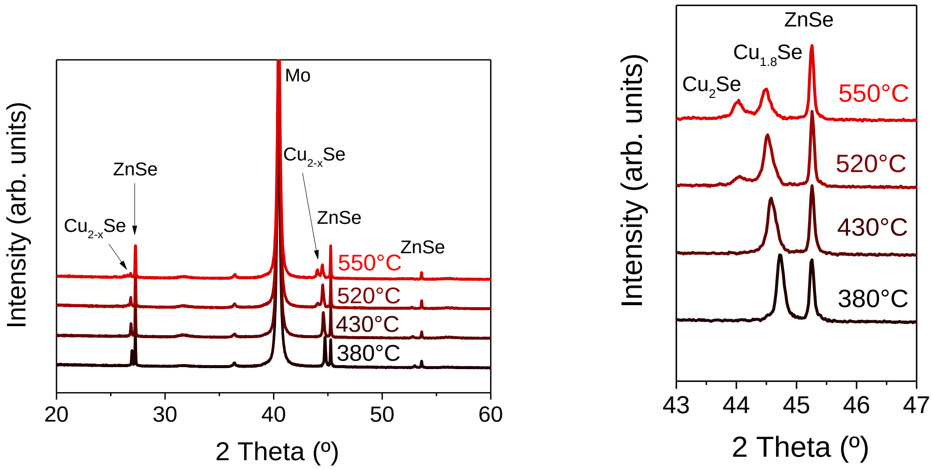

Figure 5.2. Sections of the XRD patterns of the Cu-Zn-Se samples showing the ZnSe peak at 45.2^o and the evolution of the Cu-Se binary phases. The peak attributed to $Cu_{1.8}Se$ (44.7^o) decreases in intensity with increasing conversion temperature. For the 520^{o}C and 550^{o}C samples, a peak attributable to Cu_2Se is observed and its intensity increases with temperature. The position of the peaks between 43 and 47^o have been attributed to the 220 family of planes by comparing with the powder patterns of Cu_2Se (ICSD-59955), $Cu_{1.8}Se$ (ICSD-77375) and ZnSe (ICSD-77091).

The presence of ZnSe (ICSD-77091) was observed in all samples from the 111, 220 and 311 reflections at 2-theta values of 27.2^o, 45.2^o and 54.0° respectively. The patterns also indicated the presence of Cu-binary phases and their evolution with conversion temperature. The main Cu-Se phase found in the samples was $Cu_{1.8}Se$ (ICSD-77375) with peaks at 2θ values of 27.0° and 44.7° showing a relative decrease in intensity with increasing conversion temperature compared to the ZnSe and Mo peaks. The peaks attributed to $Cu_{1.8}Se$ are slightly shifted towards lower angles as the conversion temperature increases. This shift might be due to a slight loss of Se in the $Cu_{1.8}Se$ phase as the conversion temperature increased. For the samples converted at 520 °C and 550 °C, a peak attributed to Cu_2Se (ICSD-59955) at 44.0° appears, increasing in intensity with temperature. The opposite trend is observed for the $Cu_{1.8}Se$ phase (figure 5.2). This trend evidences that an increase in conversion temperature, induces a Se loss in the Cu-binary phases, which evolve from $Cu_{1.8}Se$ to Cu_2Se as the temperature increases.

5.3.1.2 Composition and morphology of Cu-Zn-Se films

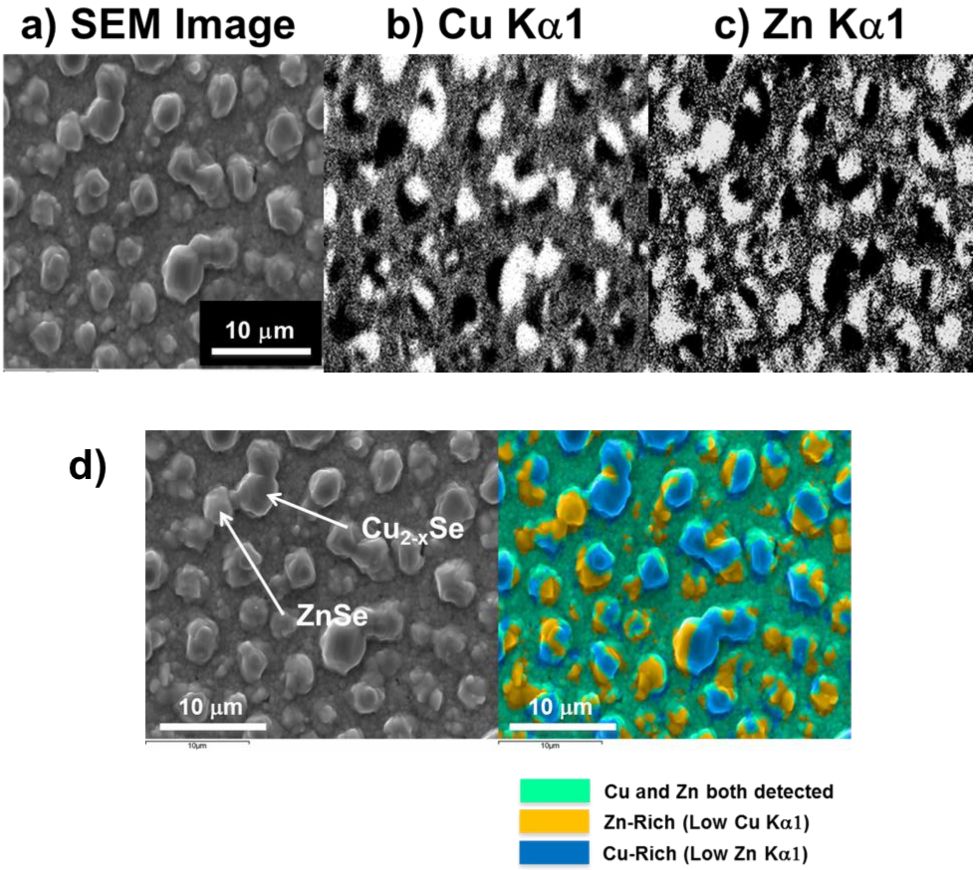

Figure 5.3. EDX map of Cu-Zn-Se sample selenised at 550 °C. High concentrations of Cu (b) and Zn (c) are indicated high intensity (white regions) of the measured Cu-Kα and Zn-Kα signals, respectively. The black regions indicate an absence of the mapped element. Cu is located where no Zn was recorded and vice versa. Phase map reconstruction showing the regions associated with high content of Zn in yellow, high content of Cu in blue and the regions where both elements are detected in green (d)

SEM and EDS mapping characterisation was used to investigate the morphology and composition. SEM surface micrographs of the set of Cu-Zn-Se samples showed that uniformly distributed, large grains were present in all films. An example of this is shown in figure 5.3.a. Mapping and point measurements of the grains showed that the composition of the features was consistent with their being composed of ZnSe and Cu-Se phases. This is in agreement with the XRD data that indicated the presence of these phases. Composition mapping of the sample converted at 550 ºC is shown in figure 5.3. A phase map elaborated with the Inca software from Oxford instruments shows the location of compositions attributed to $Cu_{2-x}Se$ and ZnSe.

The observed segregation of phases can lead to incorrect conclusions when interpreting absolute compositional data acquired with EDX, which is surface sensitive. That means that if there is a proportion of one phase segregating above the other, an increase in the counts of the elements composing the phase closer to the surface will be detected, and the obtained results could lead to misinterpretations of the composition of the whole film. For instance, the presence of a ZnSe layer at the surface, overlaying a Cu-Se phase, may lead the EDX analysis to indicate Zn-rich compositions, whereas the reality would be that the total thickness-averaged composition would not have changed from that of the precursors. In order to mitigate this issue, XRF compositional measurements were taken in this set of samples to cross check the metal ratios in the films. With this technique, the four samples gave the same ratio as the precursor with Cu/Zn equal to 2, demonstrating no loss of any of the elements.

5.3.1.3 Discussion: the formation of $Cu_{2-x}Se$ and ZnSe binary phases from Cu-Zn metallic precursors

The selenisation of Cu-Zn alloys resulted in the formation of the same phases that evolve as intermediate compounds during synthesis of CZTSe absorbers [126]. The study presented in this chapter implied that the ZnSe and $Cu_{1.8}Se$ form together in large grains. When the formation of CZTSe was produced by the selenisation of Cu-Zn-Sn metallic precursors, the reaction of liquid Se (from the Se cap) with Cu-Zn alloys contained in the precursor could lead to local segregation of secondary phases, within the CZTSe absorbers, which may be problematic for the solar cell performance. In addition to this, a loss of Se is observed in the copper selenide binary phases as the conversion temperature is increased as evidenced by the XRD patterns. A modification of the selenisation process by increasing the Ar ambient pressure of the furnace (background pressure) might help to keep the Se vapours within the graphite reactor during the conversion.

5.3.2 Conversion of Cu-Sn precursors: formation of Cu_2SnSe_3

In table 5.1 it was shown that the phases that we can expect from the selenisation of Cu-Sn precursors are Cu-Se binaries, Sn-Se binaries and the ternary compound Cu_2SnSe_3 (CTSe). In the literature, the CTSe phase has been reported to crystallise in three different modifications of monoclinc structures (space group Cc) [131-133], and this will be explored in the next subsection of the chapter.

5.3.2.1 Composition, morphology and Raman spectra of the Cu-Sn-Se films.

The composition of the Cu-Sn-Se layers produced by the selenisation of the Cu-Sn metallic precursors was measured by EDX before and after selenisation, and can be seen in table 5.3. After selenisation, the compositional values of the layers are close to the stoichiometry of the Cu_2SnSe_3 ternary compound 2:1:3.

Table 5.3. Variation of the atomic composition of the Cu-Sn-Se samples with conversion temperature.

Sample	**Conversion Temperature (°C)**	**Cu (at %)**	**Sn (at %)**	**Se (at %)**
Cu-Sn	RT	68.6	31.4	
CTSe 380	380	33.7	15.7	50.6
CTSe 430	430	33.0	16.2	50.8
CTSe 520	520	33.1	16.4	50.5
CTSe 550	550	32.4	16.0	51.6

The morphology of the layers was studied by SEM at high and low magnification. The micrographs acquired for the Cu-Sn samples selenised at the four different temperatures are shown in figure 5.4. High magnification images show very uniform surface for the samples converted at 380°C and 430°C. As the conversion temperature was increased, a number of cracks started to appear in the sample selenised at 520°C and this number increased in the sample produced at 550°C. High magnification SEM images show the formation of a polycrystalline film. It is possible to observe a clear evolution of the size of the grains of the films. For the samples selenised at 380 °C and 430 °C a uniform compact material can be observed with grain sizes of hundreds of nanometres. The sample converted at 520

°C shows the formation of well crystallised 1 μm grains and the sample at 550 °C shows larger grains of the order of 2-3 μm. Small holes can be also observed in the samples at the two highest temperatures.

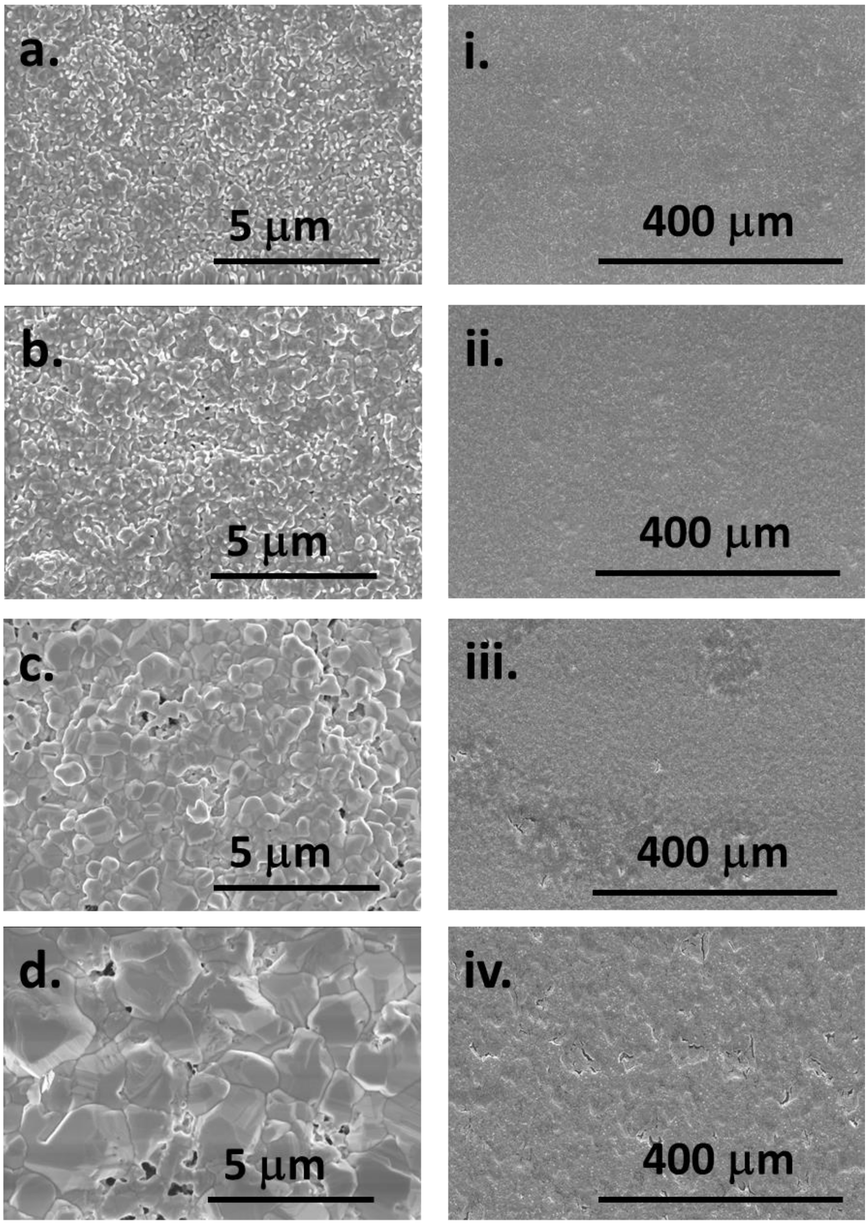

Figure 5.4. *a, b, c* and *d* shows SEM surfaces images of CTSe samples at low magnification of samples converted at 380^{o}C, 430^{o}C, 520^{o}C and 550^{o}C respectively. *i, ii, iii* and *iv* show SEM surfaces images of CTSe samples at high magnification of samples converted at 380^{o}C, 430^{o}C, 520^{o}C and 550^{o}C respectively.

5.3.2.2 XRD of the Cu-Sn-Se films

XRD patterns of the whole set of samples are shown in figure 5.5. The strongest peak observed at 40° corresponds to the Mo used as the back contact layer. In the patterns for absorbers synthesised at the two highest temperatures, at 2θ angles of 14°, 32° and 56°, it is possible to see in the patterns the presence of a broad peaks which are attributed to the formation of $MoSe_2$. These peaks increase in intensity with temperature, indicating a larger formation of $MoSe_2$ with increasing temperature. The intense peaks at 2θ 27.17°, 45.15°, 53.42°, 65.63° and 72.35° corresponds to the Cu_2SnSe_3 phase, and are observed in all samples. These peaks would overlap with the most intense peaks of the $Cu_2ZnSnSe_4$ phase at the same Bragg positions, making it difficult to identify this phase in kesterite absorbers by this technique when the quantity of CTSe phase is much smaller than the CZTSe phase present in the sample. However, additional peaks were observed in the samples converted at 430, 520 and 550°C. Figure 5.5.b shows a low angular magnification of the XRD patterns of the CTSe set of samples. At 15.5, 20.0 and 30.0° small peaks can be observed for the samples produced at 430, 520 and 550 °C, corresponding to the reflections 110, 021 and -221, confirming a monoclinic cell for Cu_2SnSe_3. This is in very good agreement with the structure reported and refined by Delgado et al [131]. These peaks increase in intensity with temperature and are not observed in the samples produced at 380°C. This does not necessarily mean that the sample produced at 380°C does not have a monoclinic structure, but a poorer crystallinity for this sample may be responsible for the lack of observed small peaks.

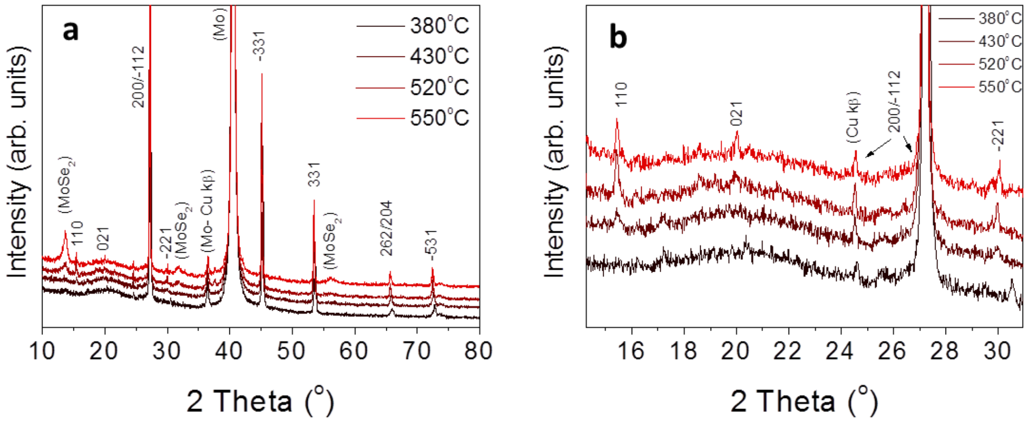

Figure 5.5. a. XRD patterns of the CTSe samples converted at 380 °C, 430 °C, 520 °C and 550 °C between 10° and 80°. **b.** Magnification of the patterns shown in **a**, between 14° and 31°, which allows observation of the presence of the reflections 110, 021 and -221 of the Cu_2SnSe_3 monoclinic phase.

5.3.2.3 Raman spectroscopy of the Cu-Sn-Se films

The formation of Cu_2SnSe_3 was also confirmed by Raman spectroscopy. Figure 5.6 shows the Raman spectrum of the CTSe sample selenised at 550°C. All the Raman spectra acquired for the samples prepared for this study were similar, confirming the formation of Cu_2SnSe_3 from 380°C to 550°C. The most intense peak observed is at 180 cm^{-1} corresponding to the strongest A’ mode [134]. It is possible to observe clearly the peaks at 235 cm^{-1} and 251 cm^{-}1, in good agreement with those reported by Altosaar et al [135]. The peak at 180 cm^{-1} presents a shoulder between 190 cm^{-1} - 215 cm^{-1} that could be attributed to the modes at 204 cm^{-1} and 211 cm^{-1} calculated by Mortazavi et al [136]. Figure 5.6.b shows the evolution of the broadening of the peak at 180 cm^{-1} of the CTSe samples processed in the whole temperature range (380 °C-550°C). The FWHM of this peak was calculated using a Lorentzian profile fitting with the software Fityk 0.9.8 [137]. The calculated FWHM values progressively decrease with increasing conversion temperature, indicating an improvement of the crystal quality of the films, as was predicted by the increase in grain size observed in the SEM images of figure 5.4.

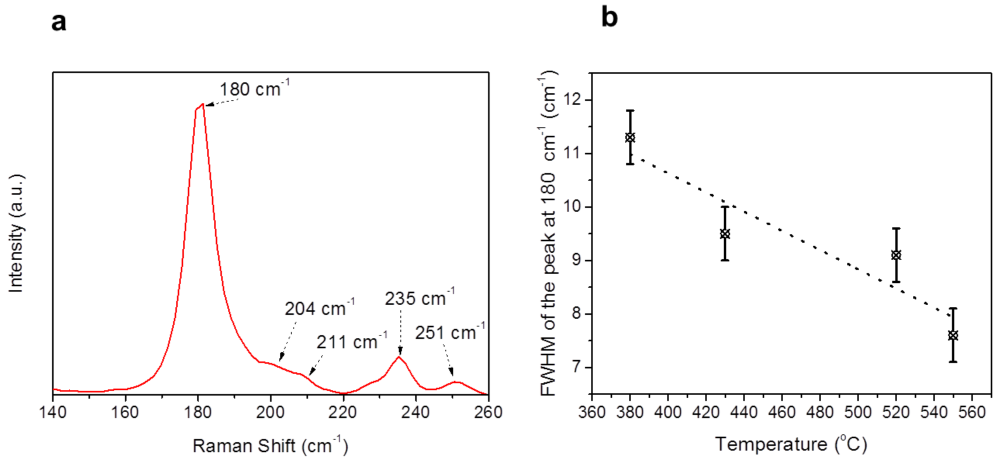

Figure 5.6. a) shows the Raman Spectra acquired with 532nm of the CTSe sample selenised at 550 °C indicating the main peaks identified associated with this phase. b) shows the FWHM values of the 180 cm^{-1} peak of the samples converted at 380 °C, 430 °C, 520 °C and 550 °C, showing a decrease on the broadening of the peaks with increasing temperature. The dotted line is visual guidance

5.3.2.4 Discussion: the formation of Cu_2SnSe_3

Recently, the $Cu_2Sn(S,Se)_3$ phase, present in the ternary phase diagrams of kesterites, [62, 124] is gaining more and more interest, not just because of its possible detrimental effect in kesterite solar cells. The potential application of $Cu_2Sn(S,Se)_3$ in PV and the use of this phase as a precursor for kesterites absorbers are being studied, since it was published that the formation of $Cu_2ZnSnSe_4$ is produced through the reaction of Cu_2SnSe_3 with ZnSe [138]. In addition to this, solar cells have been reported using Cu_2SnS_3 (CTS) as absorber layer, having the study of the formation of these ternary phases as an added value. Devices with efficiencies up to 4.6% have been fabricated out of the CTS phase [37] and Umehara et al. reported 6% efficient solar cells by introducing Ge in the synthesis of CTS layers [139]. No high efficiencies have been reported for the pure selenide Cu_2SnSe_3 (CTSe) as yet, however its high absorption coefficient of 10^4-10^5 cm $^{-1}$ and its direct bandgap, has encouraged groups to propose its use as an absorber in solar cells [53, 138, 140]. A wide range of values (0.8-2.2 eV) have been reported for the bandgap of Cu_2SnSe_3, obtained with optical absorption spectra, and no agreement is easily found in the literature. These values are far away from those calculated from a first principles electronic structure approach, where it is concluded that the material has similar optical properties to CZTSe but a narrower bandgap (0.4 eV) [141]. An ellipsometry study confirmed that CTSe had a bandgap of around 0.5 eV [54] which makes the material unsuitable for being used as a single absorber for thin film solar cells. The case of CTS, for which the bandgap is larger (close to 1 eV), is explored in more detail in chapter 9.

In this chapter, it has been shown the formation of CTSe layers by a 2-stage process consisting of the sputtering of Cu-Sn metal layer followed by a selenisation using a Se evaporated cap, with exactly the same process used for CZTSe absorber layers as described in section 5.3.3. This resulted in thin films showing the formation of Cu_2SnSe_3 crystallising in the monoclinic system. This result may appear contradictory with recent reports for co-evaporated CTSe layers in which, the formation of cubic Cu_2SnSe_3 is presented, observing a polymorphic transition from monoclinic to cubic at around 400°C [142]. For the samples presented in this chapter, from the characterisation techniques used in this study the presence of any other secondary phases was not detected. An improvement in crystallinity was found to be promoted by increasing the selenisation temperature, the film quality was decreased by the appearance of cracks and subsequent pinholes, for samples produced at the two highest conversion temperatures. A similar issue was also observed in Cu_2SnS_3 absorbers that were used for solar cells [47]. In the work of

Berg et al., a poor performance of the devices was attributed to losses due to non-covered areas by the absorber layer and the presence of pinholes, leading to very small values of shunt resistance and affecting severely the photovoltaic performance in solar cells produced by electrodeposited Cu-Sn precursors followed by sulfurisation at 550°C [47]. Voids and pinholes were also observed by Aihara et al in their solar cells produced by sulfurisation of electroplated Cu-Sn precursors at 560 °C [39].

The results presented in this section suggest that a compromise needs to be reached for selecting the optimum temperature for processing CTSe films, if they are used as precursors for the synthesis of CZTSe. It has also been demonstrated that the CTSe films crystallised in the monoclinic system for a wide range of synthesis temperatures. This demonstrates that the formation of this phase it can happen under the same conditions used for processing CZTSe absorbers, where its presence should be avoided. Although it has been suggested that CTSe is not suitable for being used as an absorber layer, theoretical calculations predict that it might be a good candidate for thermoelectric applications and the synthesis route presented in this section might be used for this application [143].

5.3.3 Conversion of Cu-Zn-Sn precursors: formation of CZTSe absorbers

In this sub-section, the formation of CZTSe in a two stage conversion process starting from Cu-Zn-Sn precursors and using a Se cap is discussed. The evolution of the films as the selenisation temperature varied was studied mainly through analysis of XRD, SEM and EDX data.

5.3.3.1 Compositional measurements of Cu-Zn-Sn-Se films

Zn-rich Cu-Zn-Sn precursors were produced for the investigation of the quaternary material. The compositions of the CZTSe absorbers obtained by EDX are shown in table 5.4. A progressive decrease of the relative Zn content, with increasing conversion temperature, can be seen from the Zn/(Cu+Sn) ratios.

Table 5.4. EDX composition measurements and Zn/(Cu+Sn) atomic ratios of the precursor and absorbers produced at different temperatures. The Zn/(Cu+Sn) ratios show a decrease in the relative Zn content with increasing conversion temperature.

Conversion temperature (°C)	**Composition (at. %)**			**Zn/Cu+Sn**
	Cu	**Zn**	**Sn**	
Precursor	48.1	27.9	24.0	0.39
380	23.7	17.0	10.8	0.49
430	24.5	16.0	11.2	0.45
520	23.9	15.7	11.5	0.44
550	24.9	14.3	11.9	0.39

When the compositions for the Cu-Zn-Sn-Se samples are compared with the ZnSe-Cu_2Se-$SnSe_2$ pseudo ternary phase diagram, reported by Dudchak et al. [62], the composition points would be located in the ZnSe-$Cu_2ZnSnSe_4$ region as shown in figure 5.7, which implies that ZnSe should be present in the samples. As was introduced in the background chapter, in section 2.2.2, this phase diagram corresponds to equilibrium conditions at 400 ºC, and it is not well known how the stoichiometric regions vary with temperature. However, it can be used as a reference point to clarify how the composition of the samples vary and which phases may be formed in each region.

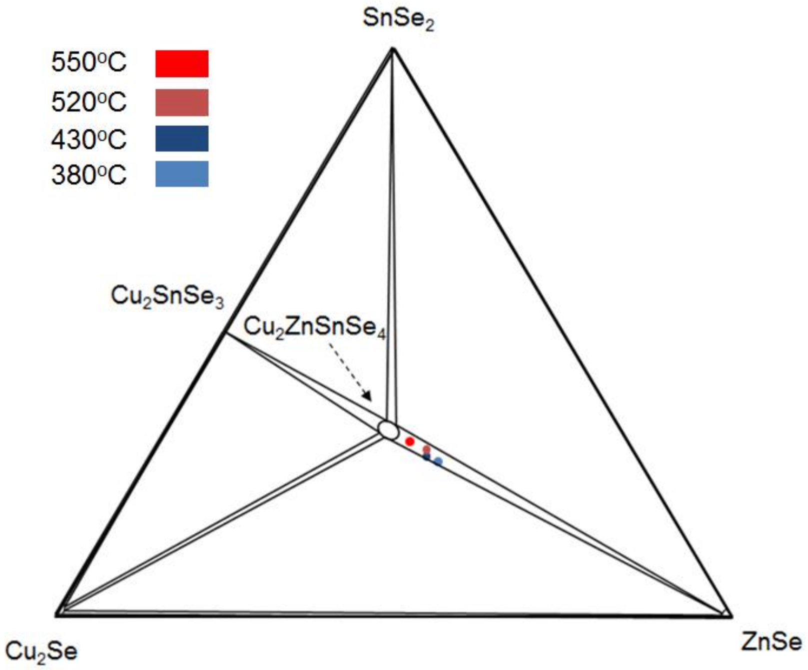

Figure 5.7 Metal ratios of the CZTSe samples synthesized at 380, 430, 520 and 550 ºC in the pseudo ternary phase diagram reported by Dudchak et al [62].

Subsequent XRF analysis was used to check the overall composition. Similarly, as reported in section 5.3.1 for the Cu-Zn-Se samples, the technique showed that there was no loss of metallic elemental components within the samples. This implied that the EDX results indicate compositional variations that are believed to be caused by localised microscopic segregation.

5.3.3.2 XRD of Cu-Zn-Sn-Se films and microstructure

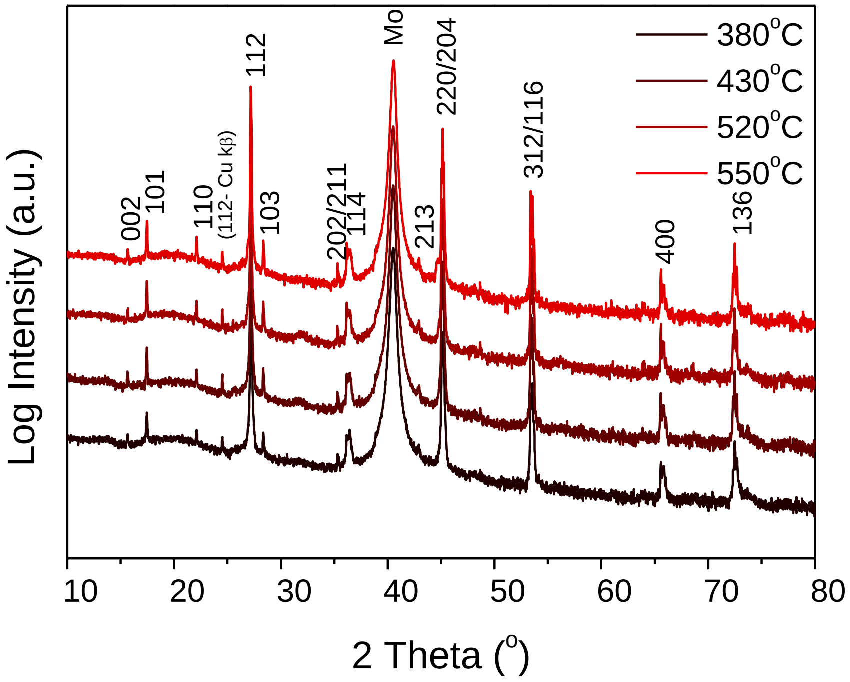

Figure 5.8. XRD patterns of the CZTSe samples synthesized at different temperatures.

X-Ray Diffraction analysis of these samples showed that $Cu_2ZnSnSe_4$ was present in all samples (Figure 5.8). The diffractograms were compared with the CZTSe powder pattern (ICSD-95117) which shows all the peaks indicating that the phase is tetragonal, including the low intensity 002, 101 and 111 peaks at 2–theta angles of 15.6°, 17.2° and 22.0°, respectively. These results are consistent with the formation of kesterite over the whole temperature range investigated. This identification has been performed in all the patterns of CZTSe film shown in this thesis. No secondary phases were detected using this technique. However, ZnSe (ICSD-77091) peaks would overlap the $Cu_2ZnSnSe_4$ kesterite peaks at 2θ values of 27°, 45°, 54°, 66°

and 73° [144], making it difficult to confirm the presence of ZnSe in $Cu_2ZnSnSe_4$ by XRD alone.

The micro-strain values of the CZTSe layers were calculated using the Williamson-Hall analysis described in section 4.3.5 and are shown in figure 5.9. A progressive decrease of micro-strain value was observed with increasing temperature. An increase in the non-uniform strain would be expected to be a result of the displacement of the atoms from their ideal lattice positions and this would result in the broadening of the peaks in the patterns. The study confirms that high processing temperatures are required to decrease the micro-strain in the CZTSe film. An increase in micro-strain in the CZTSe might be related to an increase of the concentration of dislocations or point defects such as vacancies or antisite disorders. The Cu^+ and Zn^{2+} cations have an identical number of electrons and this makes it difficult to distinguish by conventional X-ray diffraction [55], it is therefore not possible to attribute or quantify the contribution of an increase of [Zn_{Cu}] or [Cu_{Zn}] antisites to the peak broadening. Therefore, the decrease of micro-strain is attributed as a general improvement of the crystal quality of the films, evidenced by a greater grain growth, and a possible reduction of planar defects in them.

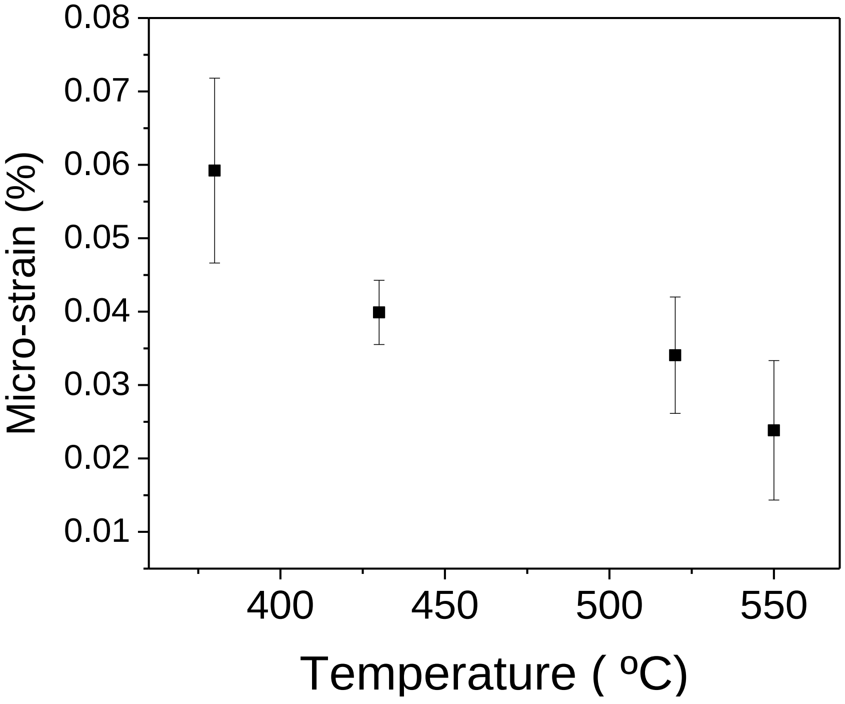

Figure 5.9. Micro-strain values derived from the Williamson-Hall method for the CZTSe samples at different temperatures.

The presence of ZnSe would be expected to be associated with Zn-rich regions. To provide evidence for the presence of secondary phases, EDX mapping and point measurements were used to measure the elemental distribution. Surface features were identified in SEM micrographs of the CZTSe. Generally, the composition was uniform, however, the features were associated with Cu-rich and Zn-rich areas, where the respective Cu/(Zn+Sn) and Zn/(Cu+Sn) ratios were larger than 2. Compositions far from the $Cu_2ZnSnSe_4$ stoichiometric region would imply the existence of other phases, in this case, the results are consistent with small regions of Cu-Se and Zn-Se phases (Figure 5.10).

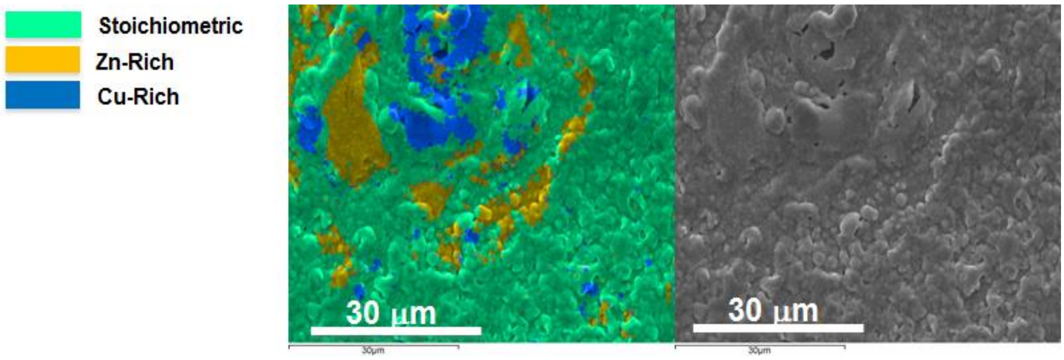

Figure 5.10. SEM surface micrograph of the surface of the Cu-Zn-Sn-Se sample selenised at 550 ^{o}C showing features with compositions acquired defined as "Stoichiometric", "Cu Rich" and "Zn Rich" by EDX point measurements related to the presence of Zn-Se and Cu-Se phases

The presence of Cu-Se binary phases was not predicted by the pseudo-ternary phase diagrams for Cu-poor compositions and the reason for their formation is still unclear. However, they may result from intermediate reactions during the formation of CZTSe. Segregation of the Zn-Se and Cu-Se phases in large grains was observed in the Cu-Zn investigation. These results allow it to be proposed that the ZnSe formation is associated with localised formation of Cu-Se binary phases or vice versa. Further studies are required to clearly identify the phases and to understand the role of intermediate reactions in the formation of CZTSe during the 2-stage process.

Morphological evolution for the CZTSe absorber layers was also observed. As the conversion temperature increased, the uniformity of the layers and the grain sizes increased. For the sample converted at 380°C, the morphology of the grains are granular and porous and they evolve as the temperature increases forming more compact and large grains as shown in figure 5.11.

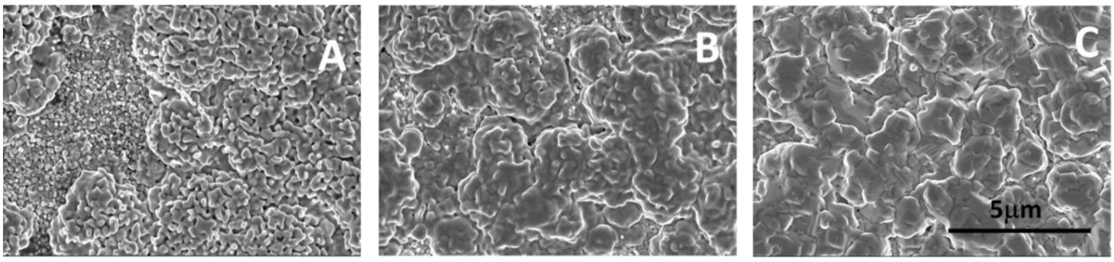

Figure 5.11. SEM top view micrographs of the Cu-Zn-Sn samples selenised at 380 ^{o}C (A), 430 ^{o}C (B) and 520 ^{o}C (C) showing an improved morphology with increasing conversion temperature.

EDX measurements result in compositional information related to localised near surface regions compared to other techniques, such as XRF. In the Cu-Zn-Sn-Se set of samples, a decrease of the Zn relative content was indicated by the evolution of the Zn/(Cu+Sn) ratio with increasing conversion temperature. This is consistent with a reduction of Zn rich phases, such as ZnSe, at the surface with increasing conversion temperature. A similar trend in decreasing ZnSe on the surface was found by Fairbrother et al. [113].

5.3.4 Analysis of the use of a Se cap layer

In this chapter and also in chapter 6 an evaporated Se cap is used to provide the chalcogen needed to react with the metals and form the kesterite. One of the advantages of using an evaporated cap is that it should ensure a spatially uniformly supply of Se across the whole surface of the precursor layer. Another advantage is that the amount of Se used can be controlled. Initially, taking into account these two characteristics, one would think that it could be a better solution than other conventional ways to provide the Se such as pellets or powder in crucibles.

After considering the positive effects of using an evaporated cap, the disadvantages of this method for delivering the Se to the sample, also need to be evaluated. The first disadvantage is the total usage of the Se. In order to evaporate a cap several Se pellets were needed to fill the crucible of the evaporation system used for this step. Then, the crucible needs to be heated, and when a uniform evaporation rate of Se vapour was achieved, a shutter covering the crucible was opened and the deposition started. Each of the Se pellets weight between 50 and 70 mg. The thickness used for the experiments was 2.3 μm. Aproximately 1g of Se was added to the crucible for each μm of Se cap evaporated. This cap was evaporated on the surface of the whole sample, with an area equal to 19.76 cm^2. With the density of Se (4.809 g cm^{-3}), it is possible to calculate that the amount of Se supplied with the cap with this thickness is approximately 22 mg. By doing this, the ratio between the Se consumed during the evaporation and the Se introduced into the graphite reactors is significantly high. This suggests that the introduction of 2-4 Se pellets directly into the graphite box would appear to enable a significantly more efficient use of Se than using between 15-25 Se pellets required for the evaporation of the Se cap. This also offers a more efficient possibility to work with high Se partial pressure.

One of the main disadvantages of the Se evaporated cap technique was not noticed at macroscopic level, where the samples showed good uniformity. A comparison of a picture of CZTSe absorbers synthesised with the Se cap method (section 3.3.1) and with Se pellets around the metallic precursor (Section 3.3.2) is shown in figure 5.12. It can be observed that the Se evaporated cap provides greater uniformity at macroscopic level. The CZTSe films fabricated with Se pellets show non-uniformities near the edges of the sample, adjacent to the locations of the Se pellets.

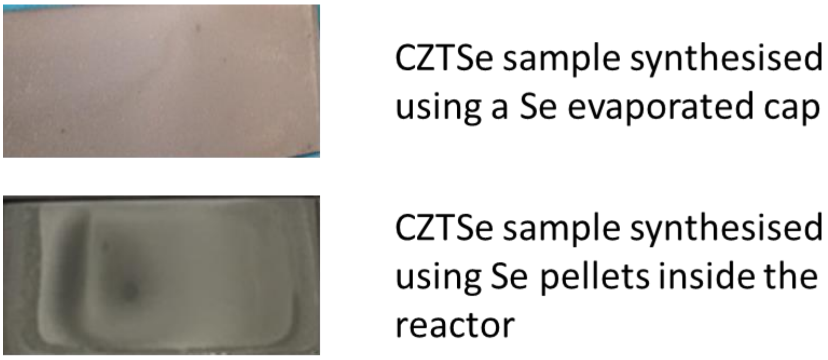

Figure 5.12. Comparison of the visual uniformity of a CZTSe absorber synthesised with the method described in section 3.3.1 with an evaporated Se cap (on top) and with method described in section 3.3.2 with Se pellets (bottom). The sizes of the samples shown in this figure are 25*50 mm^2.

At microscopic level, several localised features in the films, such as those shown in in figure 5.10 for the CZTSe films (also observed in figure 5.3 for Cu-Zn-Se films) were found when using SEM analysis of the surface of the samples. Selenisation experiments were performed in the laboratory at temperatures just above the melting point of the Se on Cu-Zn-Sn precursors. At a microscopic level it was possible to observe the formation of Se ball-like features on top of the Cu-Zn-Sn precursor, it was speculated that this may have been due to high surface tension between the Se in liquid phase and the flat surface of the precursor. A detailed study about the Se formation balls on Cu-Zn-Sn metallic precursors was being finalised by Mehrnoush Mokhtarimehr at Northumbria University at the time that this thesis was being written and a more complete study will be reported in future. The segregation of Se islands was also observed even at temperatures below the melting point of Se, as observed in the EDX mapping shown in figure 5.13 on a sample heated to 160 ºC. This appears to show a recrystallization of the Se layer and segregation onto islands that are believed to then form the ball like features when the melting point of the Se has been reached. It is thought that this may result in a localised reaction of the metal precursors and the Se liquid, creating the non-uniformities shown in the subsections 5.3.3 in the Cu-Zn-Sn-Se films (and 5.3.1 in the Cu-Zn-Se films).

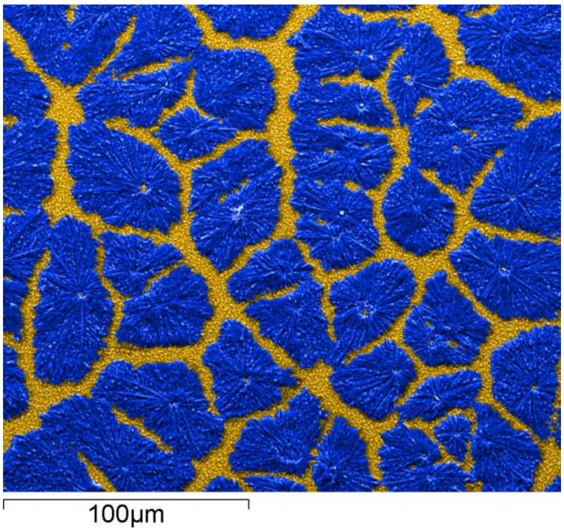

Figure 5.13. EDX phase map created with INCA software of a Cu-Zn-Sn precursor layer with a 2.3 μm Se cap heated up at 160 ºC for 3 hours. The blue regions represent where just Se was detected by EDX and the yellow regions represent where just Cu, Zn and Sn was detected.

5.4 Concluding remarks

This chapter reports the analysis of the phase evolution in the Cu-Zn-Se, Cu-Sn-Se and the Cu-Zn-Sn-Se systems, processed using a two-stage process in which metal precursor layers are sputtered onto glass substrates, selenium is evaporated on top of the sputtered metal layers and they are subsequently thermally treated to form metal-chalcogen phases.

The selenisation of Cu-Zn metallic precursors under conditions similar to those used for the production of CZTSe absorber layers was studied. The results showed that the conversion of Cu-Zn results in the formation of separate $Cu_{2-x}Se$ and ZnSe phases. ZnSe is formed in all the samples, and the evolution of the Cu-Se phases with conversion temperature has been presented. The segregation in the form of large grains is likely to be produced due to formation of Se balls in the liquid phase, which form due to the use of a Se cap, when the temperature is above the melting point of Se.

The selenisation of Cu-Sn metallic precursors resulted in the formation of monoclinic Cu_2SnSe_3, in the whole range of temperatures studied. No ball formation was observed in this case. This might be due to the fact that the melting point of Sn (231.9 ºC) is close to that of Se. This allowed a good intermixing of the elements and led to the formation of the CTSe ternary uniformly.

The synthesis of CZTSe via the selenisation of Cu-Zn-Sn precursors was also studied. XRD patterns confirm the formation of $Cu_2ZnSnSe_4$ over the range 380 °C to 550 °C. The presence of secondary phases such as ZnSe and Cu_xSe were identified with EDX mapping of the surface. It is possible to speculate that the formation of the secondary phases arises in a similar way to the segregation observed when selenising precursors in the absence of Sn. A decrease in the microstrain in the CZTSe is observed as the temperature increases. This may be due to a decrease of secondary phases, which might contribute to the breadth of the peaks observed in the XRD patterns. A decrease of the concentration of defects in the CZTSe, such as point defects or planar defects can also be responsible for this decrease in microstrain.

As a general conclusion regarding the processing conditions, it has been evaluated that the use of a Se cap might not be the best option to incorporate the chalcogen into the film. When the Se recrystallizes on top of the sample, it forms islands on top of the precursor, which melt and then induces segregation of $Cu_{2-x}Se$ and ZnSe phases in the formation process of large grains.

These studies provided an insight into the formation mechanisms of CZTSe absorber layers. Issues regarding the selenisation process were also identified highlighting the problem of using an evaporated cap. This helped in redesigning the selenisation process, in which Se pellets were used as the chalcogen source. The changes in the selenisation process were not implemented for the set of samples discussed in chapter 6, which were fabricated in parallel to the samples presented in this chapter.

6 The influence of Cu content on CZTSe I: From Cu-rich to Cu-poor

The previous chapter provided an insight into the formation of CZTSe absorbers. The crystalline quality of the CZTSe layers was shown to be greater for absorbers synthesised at the highest conversion temperature used (550 °C). Chapter 6 presents the investigation of the influence of the Cu content on the morphology and microstructure of the CZTSe thin films synthesized using the 2-stage process and the 550°C conversion temperature. The investigation studies variations of the Cu content from Cu-rich to Cu-poor CZTSe. This study enabled the identification of microstructural properties related to the Cu content of the CZTSe phase of the absorber layers synthesised, as observed by XRD and Raman spectroscopy.

This chapter is based on the following publication:

J. Márquez-Prieto, Y. Ren, R. W. Miles, N. Pearsall, and I. Forbes, "The influence of precursor Cu content and two-stage processing conditions on the microstructure of $Cu_2ZnSnSe_4$," *Thin Solid Films,* vol. 582, pp. 220-223, 2015.

6.1 Motivation and state of the art

A key requirement for high performance absorber layers is control over their composition. In the literature, the best devices have been prepared with Cu-poor and Zn-rich compositions while very few devices are reported with high efficiencies when the absorber layers have Cu/(Zn+Sn) ratios over 0.9 [14]. A better understanding of CZTSe properties with respect to composition will help to identify optimum synthesis routes and the reasons why Cu-poor and Zn-rich compositions yield higher efficiency solar cells. In this study, the composition of the precursors was varied to study the properties of Cu-rich and Cu-poor CZTSe, also reviewing the stoichiometric compositional point. The results compiled in this chapter became extremely important for the characterization of the defects in CZTSe, and their relevance is also highlighted in chapters 7 and 8.

6.2 Specific experimental details

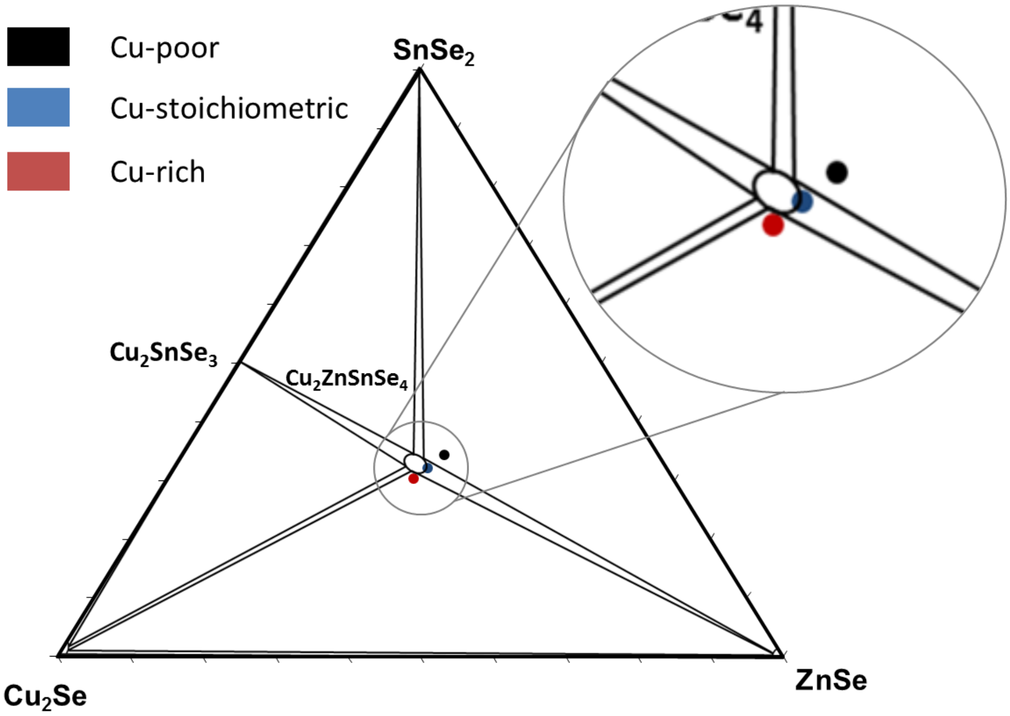

Figure 6.1. Equivalent compositions of Cu-Zn-Sn metallic precursors plotted into the pseudo ternary phase diagram of Dudchak et al [62].

Three compositions of the precursors were investigated, from the Cu-rich to the Cu-poor region passing through the “stoichiometric composition” with reference to the CZTSe pseudo-ternary phase diagram of Dudchak et al [62], and they are represented in figure 6.1. These sets of samples are referred to as Cu-poor, Cu-stoichiometric and Cu-rich respectively in this chapter as the Cu content increases. The compositions of the precursors produced for the study are compiled in table 6.1

with some relevant sputtering conditions. The selenisation process was carried out as described in section 3.3.1 at 550 ºC for 30 minutes.

Table 6.1 Sputtering conditions for the Cu-Zn-Sn precursors used in this chapter.

	EDX-Precursors	**Deposition time (min)**	**Power (W)**		
Sample	**Cu/(Zn+Sn)**		**Cu tgt.**	**Zn tgt.**	**Sn tgt.**
Cu-poor	0.84	30	130	70	140
Cu-stoichiometric	0.98	30	150	70	140
Cu-rich	1.11	30	170	70	140

6.3 Results and discussion

The general discussions applied in chapter 5, for the characteristics of the CZTSe samples processed at 550 ºC, are also applicable in this chapter. These include the presence of ZnSe, and local inhomogeneities found at the microscopic level in the absorbers. This chapter will be focused on the influence of the variation of the Cu content in the precursor and therefore in the CZTSe rather than repeat the discussion of the inhomogeneity results.

6.3.1 Influence of Cu content in CZT precursors

The influence of the Cu content in the CZT metallic precursors was also explored by means of XRD and SEM analyses. The XRD patterns of precursors with different Cu content are shown in figure 6.2. In order to show clearly the evolution of the patterns with Cu content, a diffractogram of a precursor layer with a lower Cu content

[Cu/(Zn+Sn)=0.7] is also shown. This precursor composition was used for the synthesis of CZTSe samples presented in chapters 7 and 8. The main peaks found in the patterns were attributed to Cu-Zn and Cu-Sn alloys as reported by our group [72]. In addition to these alloys, reflections attributed to elemental Sn increase in intensity when the Cu content decreases as observed in the diffractograms of figure 6.2. This is in agreement with Hutchings studies of the microstructure of Cu-Zn-Sn sputtered precursors [145]. This implies that the availability of Cu limits the alloying degree of the precursors.

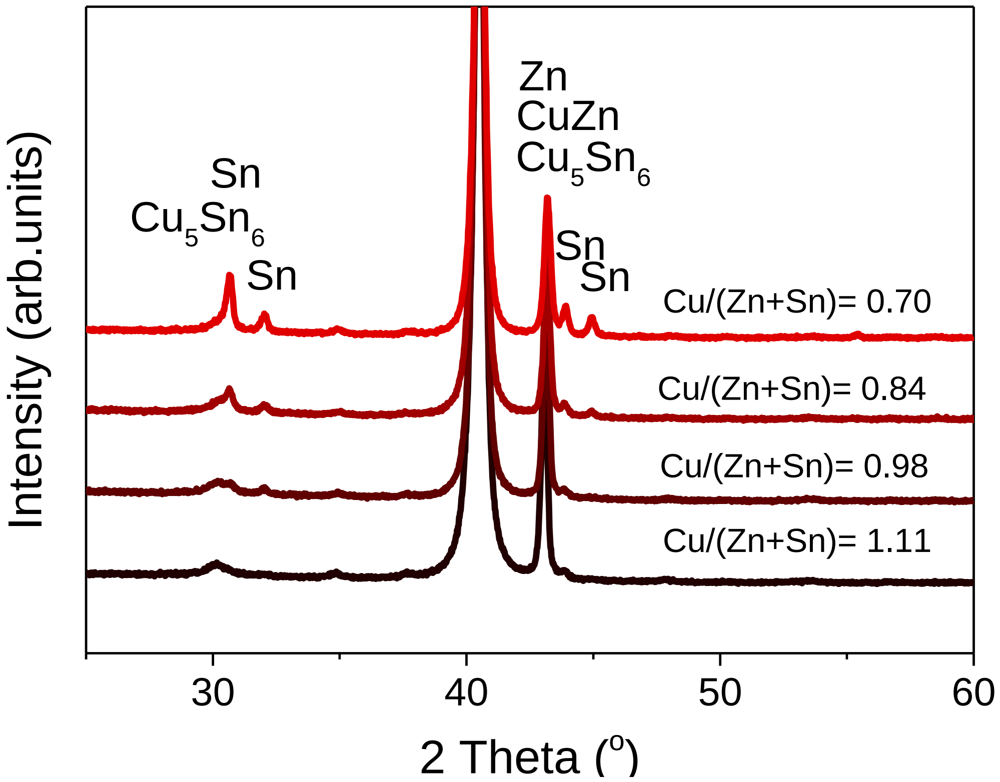

Figure 6.2 XRD patterns of CZT precursors on Mo/SLG substrates with different Cu content. The peak unlabelled at 40º corresponds to the Mo back contact as also shown in the patterns of chapter 5.

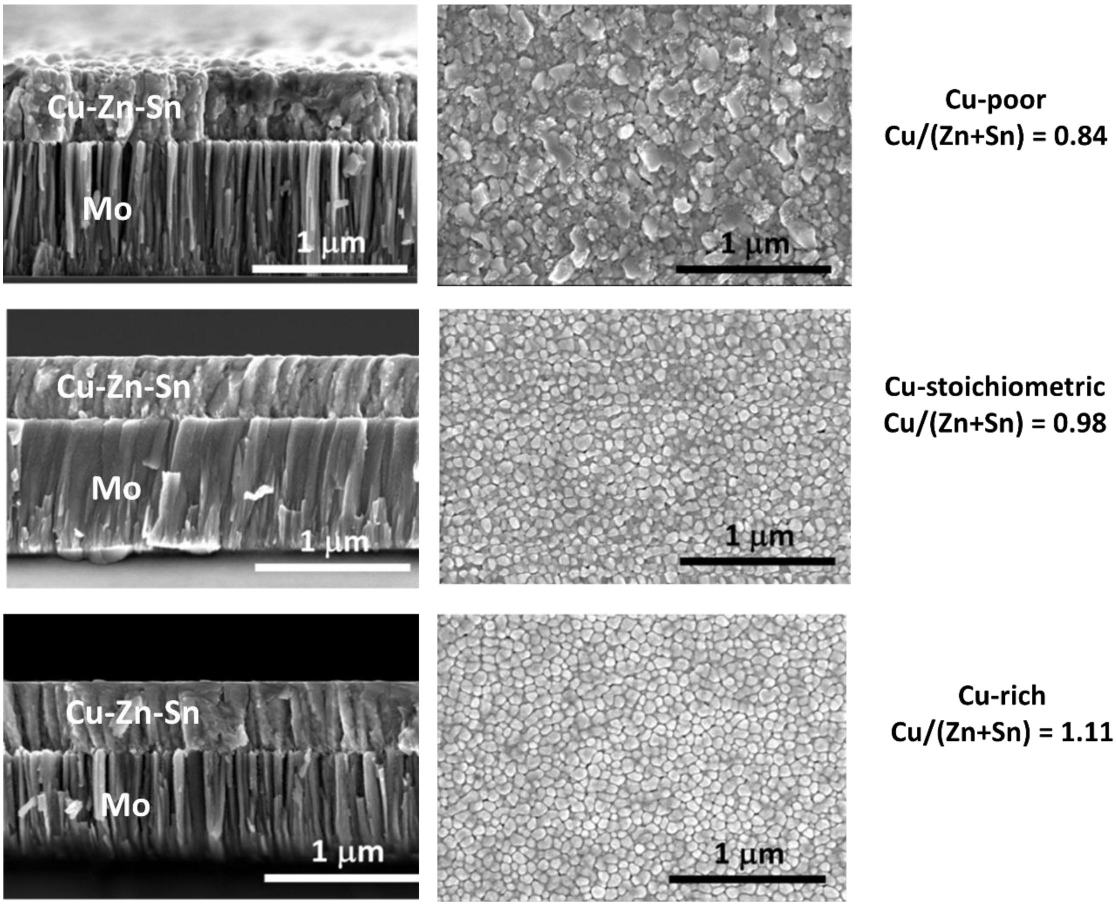

Figure 6.3 SEM micrographs of the Cu-poor, Cu stoichiometric and Cu-rich CZT precursor layer from the cross sectional (left column) and top view (right column)

The increase of elemental Sn in the precursor influenced the morphology of the films which were rougher when the Cu content was decreased (or elemental Sn increased). These changes can be observed in the SEM micrographs presented in figure 6.3. An increase in roughness for the Cu-poor sample is clear in the Cu-poor cross-section images (left hand side of figure 6.3), which also presents a different morphology in the top view micrograph. It is speculated that this may be associated with the segregation of elemental Sn in the sample. It can be seen that the precursors grow in a near columnar morphology, forming alloys, as shown in the XRD patterns, and not in multilayer structure, as was suggested in previous studies or might have been expected when considering the method by which the precursors were deposited (described in chapter 3) [19].

The influence of the microstructure on the formation of CZTSe is not very clear, at present, and is a subject that requires further study. In the literature, for electrodeposited precursors, the presence of elemental Sn was proposed as a source of blistering in the films [74].

6.3.2 Composition and morphology

SEM top view images of the CZTSe samples prepared with different Cu content are shown in figure 6.4. An increase in grain size is observed with increasing the Cu content in the precursor. The average values of grain sizes measured with the INCA software from Oxford from the SEM images of figure 6.4 are plotted in figure 6.5. The reasons for the increase are still unclear but might be due to a liquid-phase assisted growth process promoted by Cu_xSe ($x\geq1$) phases, similar to those found for chalcopyrites, which are present in Cu-rich layers even after completion of the selenisation process [146]. If this is similar to the growth process in CIGSe, introducing a Cu-rich step could lead to beneficial effects in the formation of CZTSe. However, it has been reported that similar device performance could be achieved with Cu-rich and Zn-rich growth strategies for coevaporated CZTSe [147]. Therefore, the potential benefits of introducing a Cu-rich step in the growth of coevaporated CZTSe absorbers are not clearly understood yet.

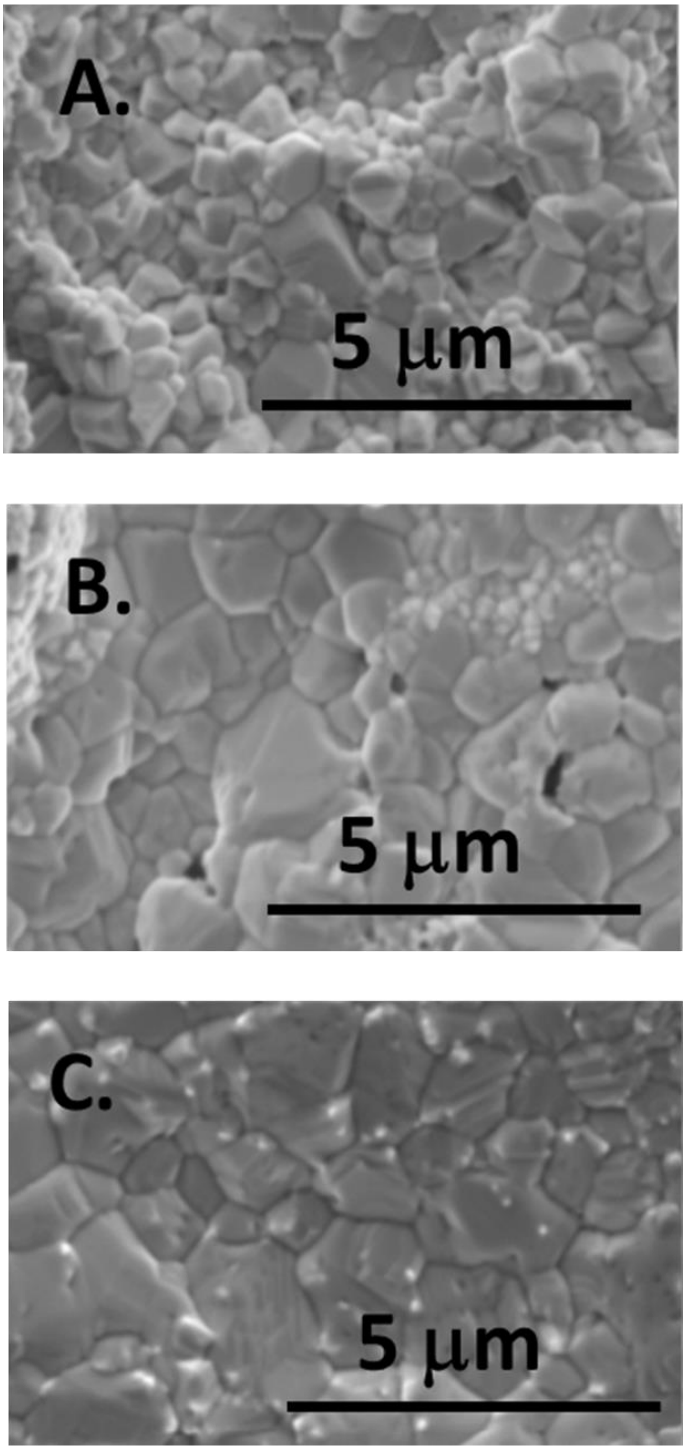

Figure 6.4 SEM top view of the CZTSe samples with Cu-poor composition (A), Cu-stoichiometric (B) and Cu-rich compositions (C).

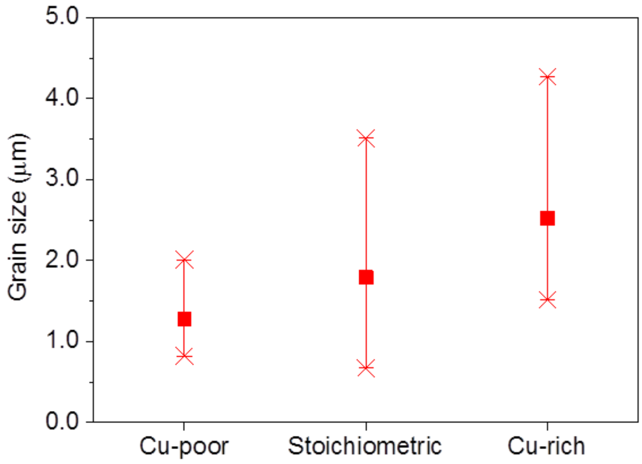

Figure 6.5 Average values of grain size measured on the SEM images plotted for each composition showing the standard deviation.

6.3.3 XRD of the CZTSe absorbers and microstructural analysis

Figure 6.6 shows the XRD patterns acquired from the Cu variation study. The diffractograms confirm the formation of CZTSe for all three compositions tested. The pattern corresponding to the Cu-rich sample shows a small shoulder on the left hand side of the 220/204 peak. This is attributed to the presence of $Cu_{2-x}Se$ (ICSD-59956), in agreement with what is expected from the quasi-ternary phase diagram shown in figure 6.1 [62].

The Williamson-Hall analysis yielded different values for micro-strain depending on the composition of the films. Figure 6.7 shows the calculated values of micro-strain with the variation of Cu content.

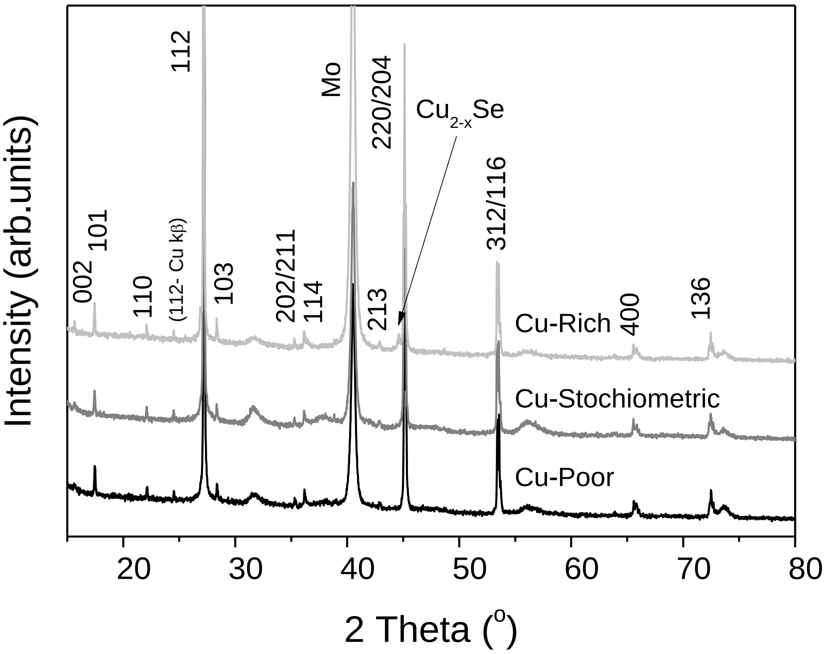

Figure 6.6 XRD patterns of the CZTSe samples with Cu-poor, Cu-stoichiometric and Cu-rich compositions. The arrow indicates reflections indicating the presence of $Cu_{2-x}Se$ in the Cu-rich sample.

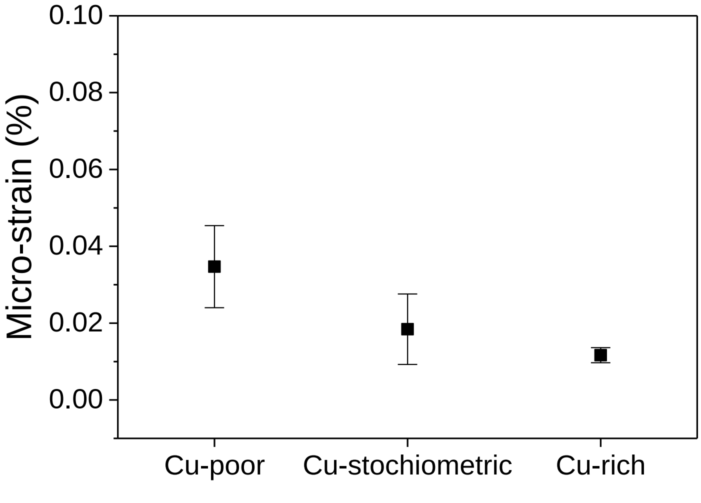

Figure 6.7 Plot showing the variation in microstrain values of the CZTSe samples with Cu-poor, Cu-stoichiometric and Cu-rich compositions.

The analysis shows a clear trend: the micro-strain values increase with decreasing Cu content of the precursor. An increase in the non-uniform strain would be expected to be a result of the displacement of the atoms from their ideal lattice positions and this would result in the broadening of the peaks in the patterns. An increase in micro-strain in the CZTSe might be related to an increase in the concentration of dislocations or point defects such as vacancies or antisite disorders. Considering that the cations Cu^+ and Zn^{2+} have an identical number of electrons, making them hard to distinguish by conventional X-ray diffraction [55], it is therefore not possible to quantify the contribution of an increase of $[Zn_{Cu}]$ or $[Cu_{Zn}]$ antisites to the peak broadening. However, an increase in $[V_{Cu}]$ or in the number of stacking faults or dislocations could be a source of the increase in the calculated microstrain observed when the Cu content is decreased. In fact, it has been suggested that in Cu-rich $CuInSe_2$ the concentration of stacking faults is significantly reduced compared to Cu-poor [148]. It is also possible to conclude that the presence of $Cu_{2-x}Se$ in the Cu rich sample does not lead to an additional increase in microstrain in the CZTSe phase, when compared to the samples with less Cu content, where this secondary phase was not detected.

6.3.4 Raman spectroscopy of the CZTSe films

Raman measurements on the films, shown in figure 6.8, also indicated that the crystalline quality of films with Cu-poor composition was poorer, with an asymmetrical broadening to the lower wavenumber side of the main Raman peak at 197 cm^{-1}. It can also be seen that the relative intensity of the modes at 168-173 cm^{-1} decreases for the Cu-poor sample, with respect to the mode at 197 cm^{-1}. Djemour et al. attributed this asymmetrical contribution to the main Raman A mode to phonon confinement because of the presence of lattice defects in the scattering volume

[149]. Recently, Rey et al. attributed the broadening of the mode at 197 cm^{-1} and the relative decrease and broadening of the peak at ~170 cm^{-1} to an order-disorder transition of CZTSe, in other words, to an increase of the concentration of $[Cu_{Zn}]$ and $[Zn_{Cu}]$ antisite defects. The results presented in the current chapter show that this asymmetrical broadening is composition dependent and related to Cu-poor absorber layers, which is consistent with these defects being related to a Cu deficit in the CZTSe structure. Ab initio calculations predicted that when the material becomes Cu poor, the concentration of $[V_{Cu} + Zn_{Cu}]$ and $[Zn_{Sn} + 2Zn_{Cu}]$ increases exponentially [60]. The presence of these defect clusters might be one of the reasons why Cu-poor Zn-rich compositions are required for high performance CZTSe solar cells [11] and may be associated with an increase in the micro-strain calculated from XRD data and with the evolution of the main Raman modes observed for the samples with Cu-poor compositions. The peak at 173 cm^{-1} is a convolution of two A modes arising from Se vibrations and two B modes from Cu-Sn and Cu-Zn vibrations, whereas the peak at 197 cm^{-1} corresponds just to Se vibrations. A decrease in the relative intensity of the peak at 173 cm^{-1}, as observed for the Cu-poor sample, might be associated to Cu deficit in the lattice, and very possibly linked to an increase of the concentration $[V_{Cu} + Zn_{Cu}]$. This will be discussed in more depth in chapter 7, which describes a study of the Cu-poor, and Zinc-rich region of the compositions of CZTSe.

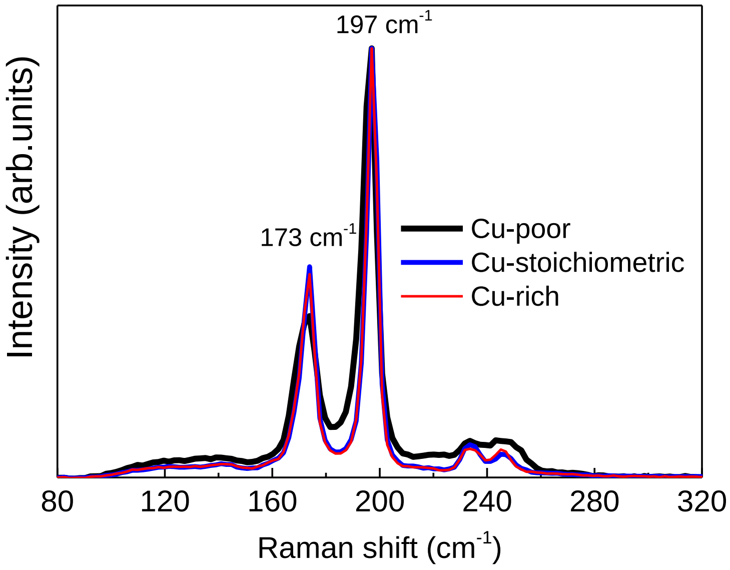

Figure 6.8 Raman spectra normalised to the A mode at 197 cm^{-1} with precursor composition defined in the text as “Cu-poor” (black), “Cu-stoichiometric” (blue) and “Cu-rich” (red) respectively.

6.3.5 Solar cells properties and limitations of the conversion process using a Se evaporated cap

The standard process for solar cell fabrication described in chapter 3 was used to produce devices from equivalent Cu-poor to Cu-rich samples presented in this chapter. The devices did not show photo activity which led to a review of the synthesis process. It was possible to tentatively attribute the poor performance of the devices to several features related to the synthesis observed in the samples presented in chapters 5 and 6 and these are discussed below:

- Local segregation of secondary phases: $Cu_{2-x}Se$ and ZnSe secondary phases were observed at the microscopic level, even in Cu poor samples as highlighted in section 5.3.3. This could affect the device performance as previously discussed. Among other problems highlighted in chapter 5, the removal of copper selenide phases due to localised segregation and through the thickness of the absorber layers, may lead to pinholes that would be expected to increase the number of shunting paths in the devices. Visual inspection of the samples confirmed the presence of pinholes in the as converted samples, leading to the conclusion that the synthesis process should be reviewed.

- Low Se partial pressure: A low partial pressure of Se during the selenisation process may lead to the surface decomposition of the CZTSe [150], the creation of selenium vacancies [151] or other factors that would affect the device performance. In conversion that uses graphite reactors, it is very difficult to accurately control the partial pressure of Se during the selenisation process. This is partly due to the lack of the control over the following: 1) leakage of vapour from the graphite boxes, 2) the temperature distribution in the tube furnace, and 3) the variation of these parameters with time. All these issues, are currently highly system related and make the reproducibility between different systems very challenging to achieve. This is also highlighted by the fact that in several groups, the best conversion parameters of CZTSe from metallic precursors are significantly different, i.e. [71, 80, 87, 152]. The leakage of Se vapour from the graphite reactor will be enhanced at lower background pressures. For the samples produced in chapters 5 and 6 the background pressure was 1 mbar. This parameter was one of those selected for review to improve the fabrication process of the CZTSe absorbers.

The actions taken towards improving the conversion process are highlighted at the beginning of the next chapter and were described in section 3.3.

6.4 Concluding remarks

The study of the influence of temperature and Cu content on the precursor for the synthesis of CZTSe by a 2-stage process has been presented. XRD analysis confirms the formation of CZTSe over the whole range of compositions investigated. Micro-strain values of the CZTSe phase decreased with increasing the Cu content of the precursors. The increase observed in micro-strain with the decreased Cu content in the films is consistent with an increase in the concentration of defects. Additionally, Raman measurements show that, for the Cu-poor composition, the red shift of the main mode at 197 cm^{-1} with an asymmetrical broadening is also consistent with an increase of defect concentration in the lattice and is related to a deficit of Cu in the crystal structure. The relative intensity of the Raman peak at 173 cm^{-1} to the one at 197 cm^{-1} depends on the Cu content in the CZTSe lattice.

SEM images reveal an increase in grain size with increasing Cu content in the samples. The present study contributes to the subject field by improving the understanding of the influence of the composition on the crystalline properties of selenised CZTSe thin film absorber layers.

Devices processed with the absorbers synthesised for this chapter did not show any photoactivity. The potential problems that could explain this were discussed and actions to mitigate these problems will be presented in the following chapter.

7 The influence of Cu content II: Investigation of Cu-poor and Zn-rich CZTSe absorber layers

The aim of this chapter is to explore and answer the question “how Cu-poor do we need to grow the CZTSSe based absorbers for maximising the performance of the devices?” To do so, the chapter explores how the Cu content in the CZTSe affects the microstucture of the aborber layers, and the performance of the solar cells within the compositional range required for device quality, commonly known as Cu-poor and Zn-rich. In addition, an important change in the synthesis of the CZTSe films, related to the selenisation step, is introduced in this chapter in comparison to chapters 5 and 6.

In the previous chapter, several issues were highlighted in relation to the selenisation step of the synthesis of CZTSe absorbers that were potentially limiting the quality of the films with regards to producing efficient solar cells. Some actions were taken to mitigate these issues and are detailed in chapter 3, in a comparison between the tube furnace and the rapid thermal conversion processess explained in sections 3.3.1 and 3.3.2 respectively. Qualitatively, and for the clarity of the reader, some of the main changes in the selenisation process can be summarised in the following points:

- A change in the Se source from a Se capping layer to Se pellets inside the graphite reactor.
- An increase the amount of Se in the reactor from ~22 mg with the Se cap to ~250 mg by introducing 4 Se pellets in the reactor.
- The use of a graphite reactor with lid attached with screws.

- The increase of the background pressure of the inert gas from 1 mbar to 850 mbar.
- A change from a large quartz tube furnace to an Annealsys RTP.

This chapter is partly based on the following publication:

J. Márquez, M. Neuschitzer, M. Dimitrievska, R. Gunder, S. Haass, M. Werner*, et al.*, "Systematic compositional changes and their influence on lattice and optoelectronic properties of $Cu_2ZnSnSe_4$ kesterite solar cells," *Solar Energy Materials and Solar Cells,* vol. 144, pp. 579-585, 2016.

7.1 Motivation and state of the art

In the previous chapter, the influence of the Cu composition on the microstructure of the CZTSe absorbers was studied. It was concluded that when the CZTSe absorbers had Cu deficit, the defect concentrations of these samples were significantly higher than in the samples without Cu deficit according to the stoichiometry of the $Cu_2ZnSnSe_4$ compound (2:1:1:4).

It has been reported several times in the literature that Cu-poor and Zn-rich compositions are needed to make high efficiency solar cells [11]. However, more experimental data regarding composition is needed in order to determine how the variation in the metal ratios affects the crystal structure of CZTSSe compounds in thin films and the correlation with the optoelectronic properties of the solar cells processed from them. When different publications where solar cells and their compositions are reported and compared, it is difficult to identify trends and therefore difficult to conclude why the devices work better within certain values of composition. With the addition of experimental errors in the compositional measurements, different calibration methods, and different techniques used for measuring, it is even more difficult to define certain values of compositions and relate them to the properties of the solar cells.

The main parameter that it is being tracked for kesterites is the open circuit voltage of the solar cells, since it most significantly differs between CZTSSe and CIGS solar cells. The open circuit voltage deficit, defined as Eg/q – V_{OC}, is substantially larger for CZTSSe devices with values close to 600 mV compared to CIGSe devices which generally present V_{OC} deficits less than 500 mV [15]. There are several possible explanations for the V_{OC} deficit that CZTSSe devices currently present. Firstly, $Cu_2ZnSnSe_4$ (CZTSe) and Cu_2ZnSnS_4 (CZTS) present a very narrow stoichiometric region [62, 124, 153]. In addition, it has been demonstrated that at high temperatures, when in contact with metallic Mo which is normally used for the back contact in kesterite solar cells, CZTSSe decomposes [73, 154]. It has also been proven that high chalcogen partial pressures are required when crystallising the CZTSSe in order to avoid the decomposition of the absorber layer on the surface [150] that leads to a decrease in the photovoltaic performance of the devices. In the bulk of the absorber layer, many questions are still to be resolved regarding the crystal structure of these materials. A better understanding of the formation and impact of defects needs to be developed in order to decrease the current V_{OC} deficit of the kesterite devices [17]. A combination of neutron and X-ray diffraction analysis demonstrated that CZTSe and CZTS crystallises in the kesterite type structure and also that Cu_{Zn} and Zn_{Cu} antisites in the (001) planes at z = 1/4 and 3/4 are present in high concentration opening the discussion of how ordered are the synthesized kesterite type compounds [55]. The order-disorder transition has been studied by Scragg *et al.* for CZTS [58], Kraemmer *et al.* for CZTSSe [61] and Rey *et al.* for CZTSe [60]. It has been concluded that this transition can change the effective bandgap of the material by more than 100 meV, thus affecting the V_{OC} of solar cells synthesized from the same absorbers with different degrees of ordering [155]. This chapter also aims to partly address the problem of the Cu-Zn disorder and how this is affected by variations in composition.

First principle calculations have explained theoretically why Cu-poor, Zn-rich kesterite solar cells should be of higher efficiency [11]. It was concluded that V_{Cu} could contribute to p-type conductivity. It was also shown that some self-compensated defect clusters [V_{Cu} + Zn_{Cu}], [Zn_{Sn} + $2Zn_{Cu}$] and [$2Cu_{Zn}$ + Sn_{Zn}] have low formation energy and can be present in high population either in CZTS and in CZTSe. [$2Cu_{Zn}$ + Sn_{Zn}] could induce electron-trapping effects and [V_{Cu} + Zn_{Cu}] could induce a downshift in the valence band that might be beneficial for the solar cell performance, helping the electron-hole separation.

As introduced in section 2.2.3, Lafond et al. studied the most realistic substitution reactions for Cu-poor CZTS concluding that two types of defects were the most likely to be formed: [Zn^{2+} + V_{Cu}] (A-type, presenting Cu poor and Zn rich composition) and [$2Zn^{2+}_{Cu}$ + Zn^{2+}_{Sn}] (B-type, presenting Cu poor and Sn poor composition) [68]. In a solid state nuclear magnetic resonance (NMR) study, Paris *et al.* demonstrated the presence of [V_{Cu} + Zn_{Cu}] and [$2Zn^{2+}_{Cu}$ + Zn^{2+}_{Sn}] for A-type and B-Type CZTS respectively [156]. The reader is referred to chapter 2 for the explanation of the plot correlating the different defect type lines with composition, which is used in the following sections of this chapter.

7.2 Specific experimental details

Cu-Zn-Sn metallic precursor layers were deposited on Mo coated SLG glasses as described in chapter 3. Three different compositions of precursors were used for this study. The sputtering conditions of the production of the set of samples with different

Cu content are summarised in table 7.1. The precursor used for the preparation of Sample 1 belongs to the same deposition batch as the Cu-poor sample of chapter 6.

For an easier understanding of this chapter, the samples prepared with the three different compositions will be referred as Sample 1, Sample 2 and Sample 3 as the Cu/(Zn+Sn) ratio decreases in the films and the composition moves away from the stoichiometric point in the pseudo-ternary phase diagram (see figure 7.1).

Table 7.1 Sputtering conditions for the Cu-Zn-Sn precursors used in this chapter.

	XRF-Precursors	**Deposition time (min)**	**Power (W)**		
Sample	**Cu/(Zn+Sn)**		**Cu tgt.**	**Zn tgt.**	**Sn tgt.**
Sample 1	0.90	30	130	70	140
Sample 2	0.70	35	120	70	140
Sample 3	0.65	40	110	70	140

The selenisation process was carried out by RTP at 500 ºC for 15 minutes as described in section 3.3.2.

7.3 Results and discussion

7.3.1 Composition of the CZTSe absorbers

To show a clear comparison, the metal compositions of the absorber layers produced in this study are plotted in figure 7.1 in the pseudo-ternary phase diagram (TPD) reported by Dudchak et al [62]. The metal atomic composition of the precursors and absorber layers was measured either by EDX at 20 kV from the top view or with XRF, and the values can be seen in table 7.2. A comparison of the composition between the precursors and the absorbers measured by XRF shows that the Cu/(Zn+Sn) ratios increase after the selenisation process. The Zn and Sn loss is attributed to the formation of volatile compounds of both constituents [20]. The Zn/Sn ratios seen for Sample 2 and Sample 3 increase after the selenisation process, indicating an increase of the Sn loss as the Cu content decreases in the precursor, as also observed by Collord et al [21].

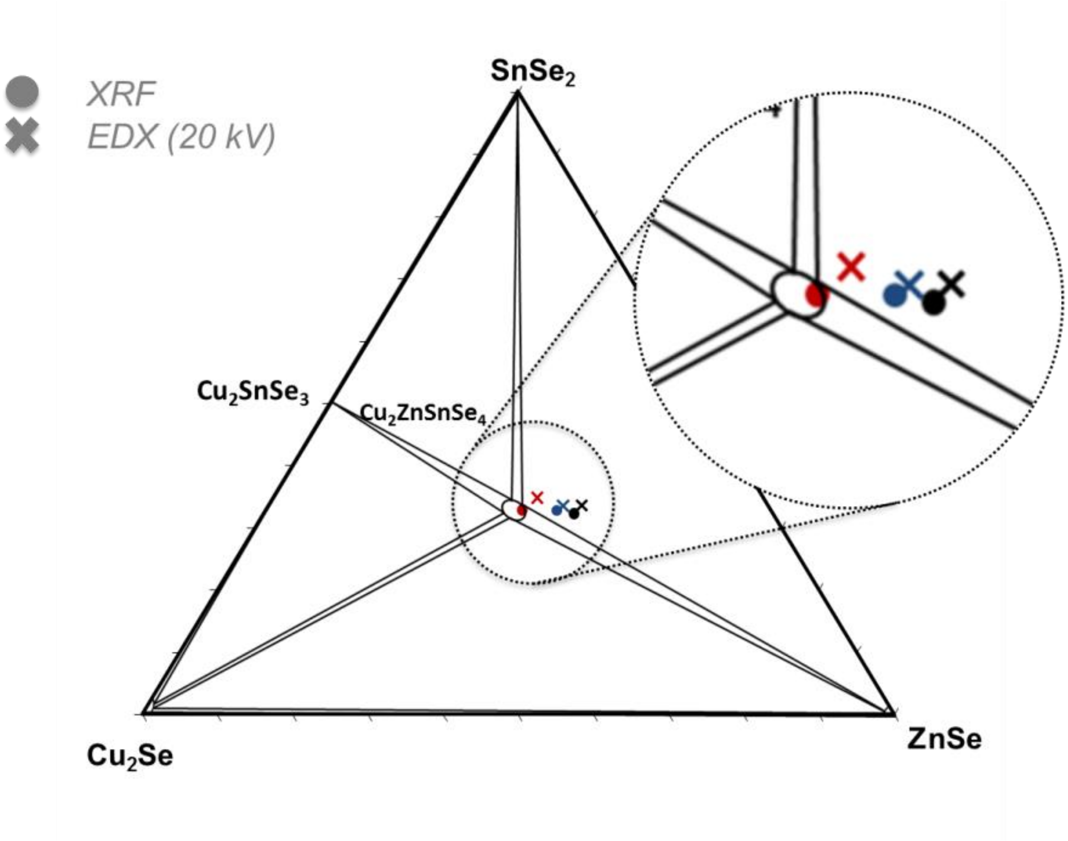

Figure 7.1. Pseudo-ternary phase diagram showing the average composition of the CZTSe absorber layers of this study measured with XRF represented with dots and EDX represented with crosses. As the points shift away from the stoichiometric point, the Cu content decreases moving from the Sample 1 (red), to the Sample 2 (blue) and then Sample 3 (black).

Table 7.2. Compositional atomic metal ratios of the Cu-Zn-Sn and CZTSe absorber layers of the study presented. The technique used for measuring the composition is specified at the top of each column.

	[XRF-Precursors]		**[XRF-CZTSe]**		**[EDX-CZTSe]**	
Sample	Cu/(Zn+Sn)	(Zn/Sn)	Cu/(Zn+Sn)	(Zn/Sn)	Cu/(Zn+Sn)	(Zn/Sn)
Sample 1	0.90	1.03	0.99	1.04	0.86	1.00
Sample 2	0.70	1.09	0.80	1.18	0.75	1.17
Sample 3	0.65	1.12	0.72	1.28	0.66	1.24

As discussed in chapter 5, EDX compositional measurements could be influenced by the presence of secondary phases on the surface such as ZnSe or Cu_xSe providing values that do not necessarily correspond to a representative average composition of the absorber layer [157]. Therefore, a combination of EDX and XRF measurements could be useful to compare and especially to make sure that the trends of composition studied are consistent. Differences are observed between the two measurements. Apart for the difference in penetration depth of each technique, this variation could be attributed to several factors such as the calibration used for each method. The main difference observed between the measurements is that, for the samples of this study, in both the precursors and the absorbers, the apparent Cu content is higher when measuring with XRF. The average composition of the films measured with the two techniques follows the same variation, with the difference between them being the variation in Cu content. Qualitatively, it is possible to observe that “Sample 2” and “Sample 3” have compositions far from the stoichiometric region. The reactive annealing process used for the synthesis of the CZTSe absorbers uses fast ramping rates. The ternary phase diagram, which applies to equilibrium conditions at 400 ºC, might not be the most adequate tool for estimating the amount and presence of secondary phases in the film as was discussed in chapter 2. However, it can provide an idea of which potential secondary phases might be present in the absorber layers. As the Cu content in the film decreases, the compositions plotted in the ternary phase diagram are located in the ZnSe-$SnSe_2$-CZTSe region so one could predict the possible presence of ZnSe and $SnSe_x$ particularly in “Sample 2” and “Sample 3”.

7.3.2 Raman spectra and prediction of defects

The metal compositions of the samples are plotted along the off-stoichiometric type lines in figure 7.2.a. As the Cu decreases from Sample 1 to Sample 3, the points move towards the A-type line, predicting an increase in the concentration of $[V_{Cu} + Zn_{Cu}]$ [68]. Raman spectra of the CZTSe absorbers measured with 532nm excitation are shown in figure 7.2.b. All peaks observed in the spectra are attributed to the Raman modes of the CZTSe phase [116]. For the analysis presented here, the discussion is focused in two main peaks:

- The most intense peak centred at ~197 cm^{-1} which is attributed to A symmetry mode and involves purely Se anion vibrations [158].
- A broad peak centred at around 170 cm^{-1} which could be attributed to the convolution of two A modes (corresponding to Se vibrations) and two B modes (involving mostly Cu/Zn and Cu/Sn atomic plane vibrations [159])

The three spectra are normalised to the most intense peak at ~197 cm^{-1}. When the Cu content is decreased in the absorber layers, the relative intensity of the peak at

170 cm^{-1} decreases. In chapter 6, it was observed that the intensity of this peak with respect to the A mode at 197 cm^{-1} was very sensitive to the Cu content in CZTSe thin films, decreasing when there was Cu deficit in the structure [117]. When the Cu/(Zn+Sn) ratio decreases and the composition moves away from the stoichiometric point towards the Cu poor region in the ternary phase diagram shown in figure 7.1, the relative intensity of the band at 170 cm^{-1} also decreases. One possible explanation for this decrease is that it is related to an increase in the concentration of [V_{Cu} + Zn_{Cu}], which has been theoretically predicted to be present in high population in Cu poor CZTSe [11]. This could decrease the intensity of the B modes appearing in this region corresponding to the vibrations of Cu/Zn and Cu/Sn atomic vibrations, as reported in [116], which would lead to the overall decrease in the intensity of the peak cantered at 170 cm^{-1}. The inset in figure 7.2.b shows a magnification of the Raman spectra centred at the A mode at 196 cm^{-1}. When looking in detail at the position of this peak, one can observe that for “Sample 2” and “Sample 3” it is blue shifted in comparison to “Sample1”. Rey *et al*. observed a blue shift of the A mode that could be related to an increase in the ordering in the samples of their study. [60]. In this study, it could be an indication that the two CZTSe thin films with less Cu content are more ordered than the one with composition near to the stoichiometric point. This is in agreement with the study of Paris *et al.* where they observed that Cu poor CZTS samples with predominant [V_{Cu} + Zn_{Cu}] defect clusters presented an increase in the ordering of the Cu and Zn cations in the 2c and 2d positions [156]. It is also appropriate to state that the opposite has been suggested for CZTS samples grown by flash evaporation and subsequent annealing [160].

Because of the large deviation of the composition of the CZTSe layers compared to the stoichiometric point and that the presence of ZnSe could be expected, Raman spectroscopy measurements with a blue laser were also performed to identify if ZnSe was present in the samples [161]. Several spots were probed in each sample and it was concluded that within the detection limits of this technique, no ZnSe was found in the surface of these set of samples.

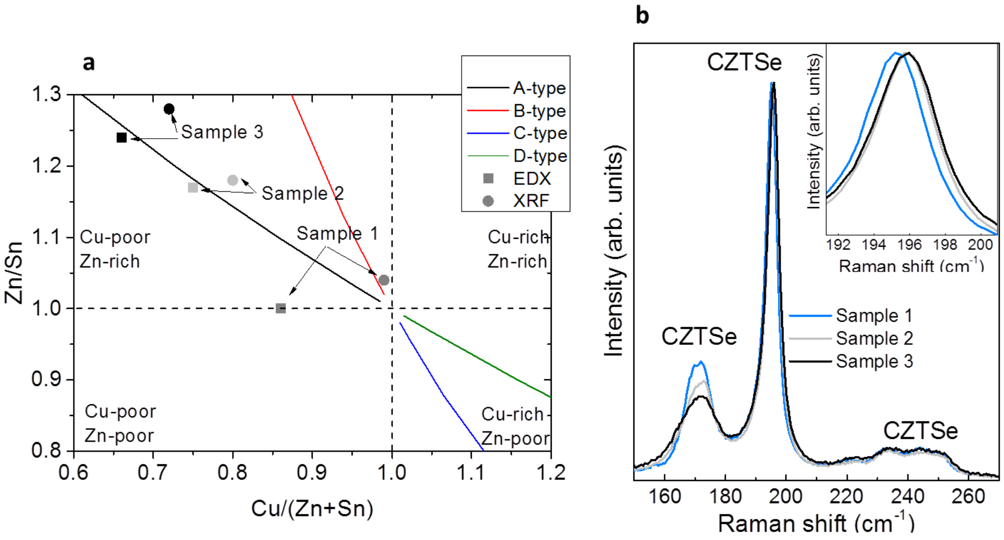

Figure 7.2 a) Positions of the samples 1-3 in the Cu/(Zn+Sn)-Zn/Sn plot indicating the off-stoichiometric type. b) Raman Spectra of the Sample 1 (blue), Sample 2 (grey) and Sample 3 (black) acquired with 532 nm excitation wavelength. The inset shows a magnification of the main A mode at around 197 cm^{-1}.

7.3.3 XRD of the CZTSe absorbers

Le Bail analysis was performed on the XRD patterns acquired at different GI angles for the CZTSe absorbers layers in order to have an accurate calculation of the lattice parameters. An example of one of the refinements of the patterns was provided in section 4.3.4. All the refinements performed for the samples of this chapter had an X^2 value below 2. This subsection is focused on the results obtained from the refinements. The diffractograms acquired at a GI angle of 1° are shown in figure 7.3. No secondary phases could be detected with this technique in the absorbers of this study. This is particularly interesting, since the composition of Sample 2 and Sample 3 are far away from the stoichiometric region of CZTSe and, if there was a quantitative presence of $SnSe_x$, then this technique should indicate it. The diffraction patterns were measured with low incidence angle of 0.5, 1 and 2º acquiring information from the near surface and bulk region of the absorbers. This allowed us to reduce the potential variations in the lattice parameter calculations induced by uniform strain created by the growth of $MoSe_2$ at the interface with the back contact. In addition, the acquisition of data from the near surface region ensures a more reliable comparison with the penetration depth of the laser used for recording the Raman spectra (~100nm).

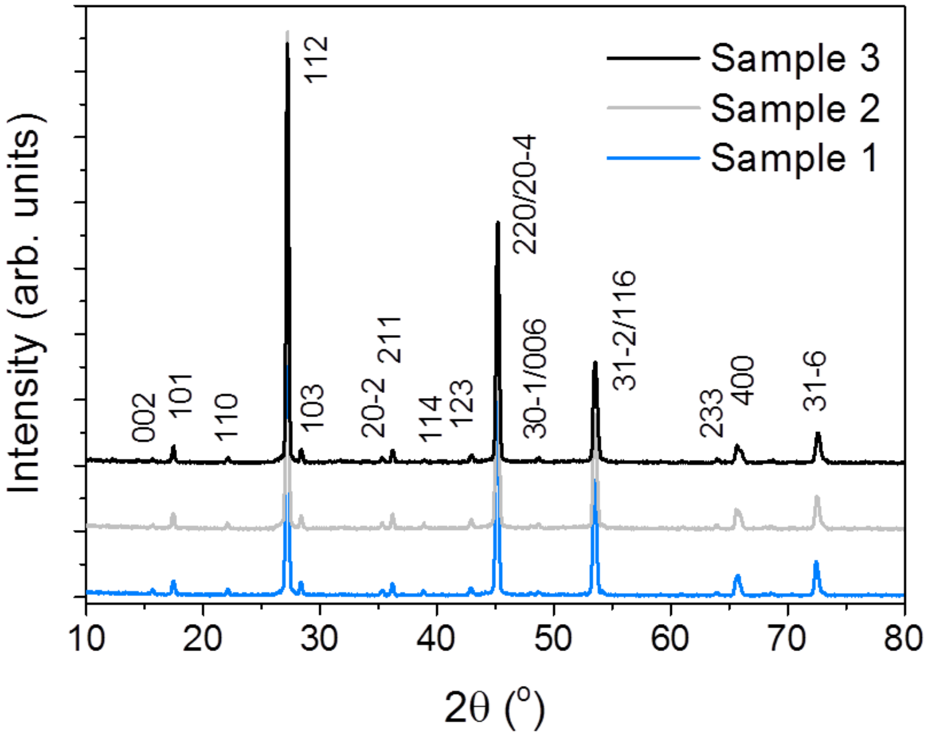

Figure 7.3 XRD patterns of the CZTSe absorbers acquired for a grazing incidence angle of 1°.

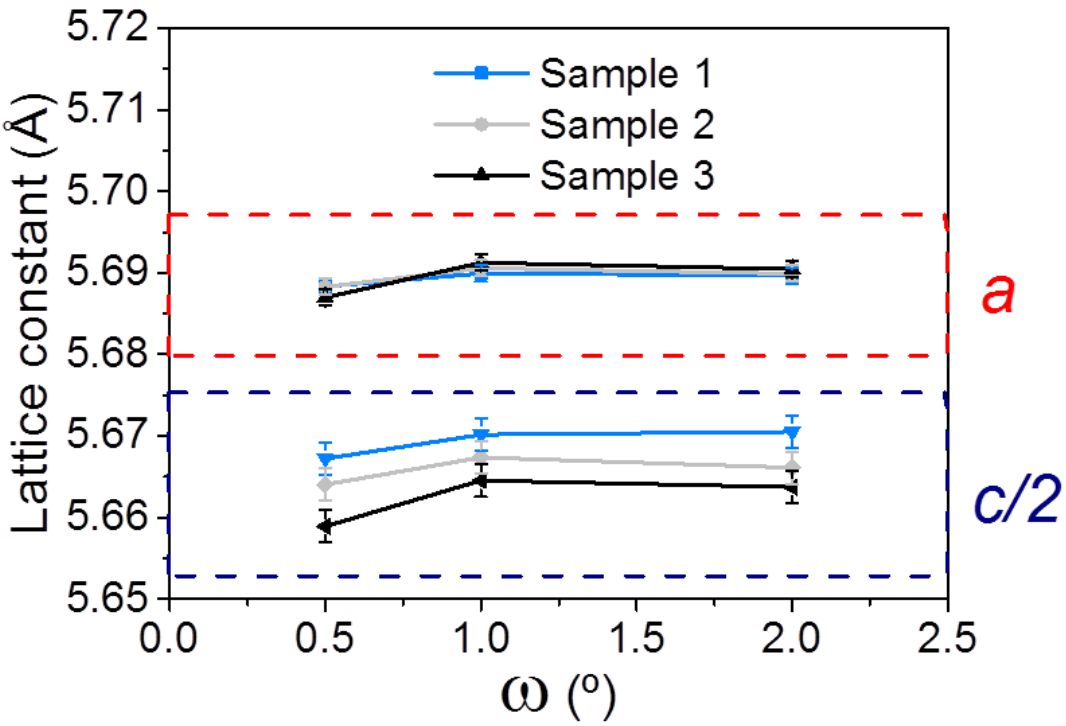

Figure 7.4 Lattice parameters of the of the CZTSe absorber layers calculated from the patterns acquired for different grazing incidence angles.

Figure 7.4 shows a comparison of the lattice parameters obtained for the CZTSe absorber layers of this study. The lattice constant *a* does not appear to be influenced by the variations in composition, although the lattice constant *c* decreases significantly when the Cu content in the samples is decreased. It is possible to observe a small shift of the lattice parameters in the three samples for the incidence angle (ω) of 0.5º. This could be due to diffraction when close to the critical angle. Schorr studied the temperature behaviour of the lattice parameters of CZTS, where a monotonic decrease of the lattice parameter *a* was observed with decreasing temperature [55]. A different behaviour was observed for *c*, where a kink indicating a more abrupt reduction of the lattice constant was observed starting at around 260ºC. This temperature was estimated to be the order-disorder transition temperature of this compound [58]. Additionally, Cu/Zn disorder has been predicted to expand the unit cell volume mainly by an increase in the value of *c,* suggesting that an accurate estimation of the lattice parameters can provide valuable information related to order-disorder in CZTSSe materials. These results show that the lower the Cu content of the CZTSe samples, the lower is the value of *c* and therefore a lower value of the tetragonal deformation (*c*/2*a*). The decrease in the value of *c* is in agreement with the theory of the increase in ordering of Cu/Zn (001) planes, as well as the results obtained from Raman spectroscopy.

7.3.4 Solar cell properties

The dark and illuminated current density-voltage (J-V) curves are represented in figure 7.5.a. Current-voltage characteristics values of the best devices processed with the CZTSe absorbers with different compositions within the Cu-poor and Zn-rich region are shown in table 7.3 and in figure 7.5 c, d, e and f with the average and maximum values of 9 cells measured in each sample category. It is possible to observe an increase in the performance of the devices when the Cu content in the absorber layer is decreased. This increase in performance is mainly driven by an increase in V_{OC}, from 367 mV to 434 mV. EQE measurements of the solar cells with different compositions are also presented in figure 7.5.b. The three devices present EQE values around 80-90 % between 500 and 900 nm. It is also possible to see interference in this range that may lead to loss in current. This is attributed to the TCO which in the case of these samples is about 700 nm thick with the aim of having a safer contact with sharp probes for electrical characterisation, since a front grid was not evaporated on these devices. The bandgap, Eg, of the devices is calculated from the inflection point of the decay of EQE at long wavelength. The values obtained are also shown in table 7.3. This method has already been used in highly efficient CZTSSe solar cells for calculating the bandgap and for evaluating the tail profile associated with potential fluctuations and bandgap fluctuations. The derivative method was also assumed to be the most robust for the calculation of Eg values [121]. It is interesting to observe that a difference in the bandgap of around 70 meV can be found between Sample 1 and Sample 3. This difference can also explain the increase in V_{OC} of around 70 mV in the case of the best cells and an increase of around 50 mV in the average values as shown in figure 7.5.d. V_{OC} varied from 367 to 434 mV when changing composition of the best devices from Sample 1 to Sample 3, the one with the lowest Cu content of the series. A similar trend with decreasing Cu content and increasing Zn/Sn ratio has also been identified for the CZTSSe solar cells [162].

Table 7.3. Electrical parameters of the best CZTSe solar cells fabricated with different compositions. The values of J_{SC} between parentheses are calculated from the integration of the EQE with the AM 1.5 solar spectrum. The efficiency values are calculated from the measured values of J_{SC}. The corrected efficiency of Sample 3 with the value of J_{SC} calculated from the EQE is also shown in parentheses.

Sample	**Voc (mV)**	**Jsc (mA/cm^2)**	**FF (%)**	**Eff (%)**	**Eg (eV)**
Sample 1	367	33.0 (33.3)	56.8	6.9	1.00
Sample 2	411	34.0 (34.1)	56.2	7.9	1.04
Sample 3	434	31.2 (32.8)	59.6	8.1 (8.5)	1.07

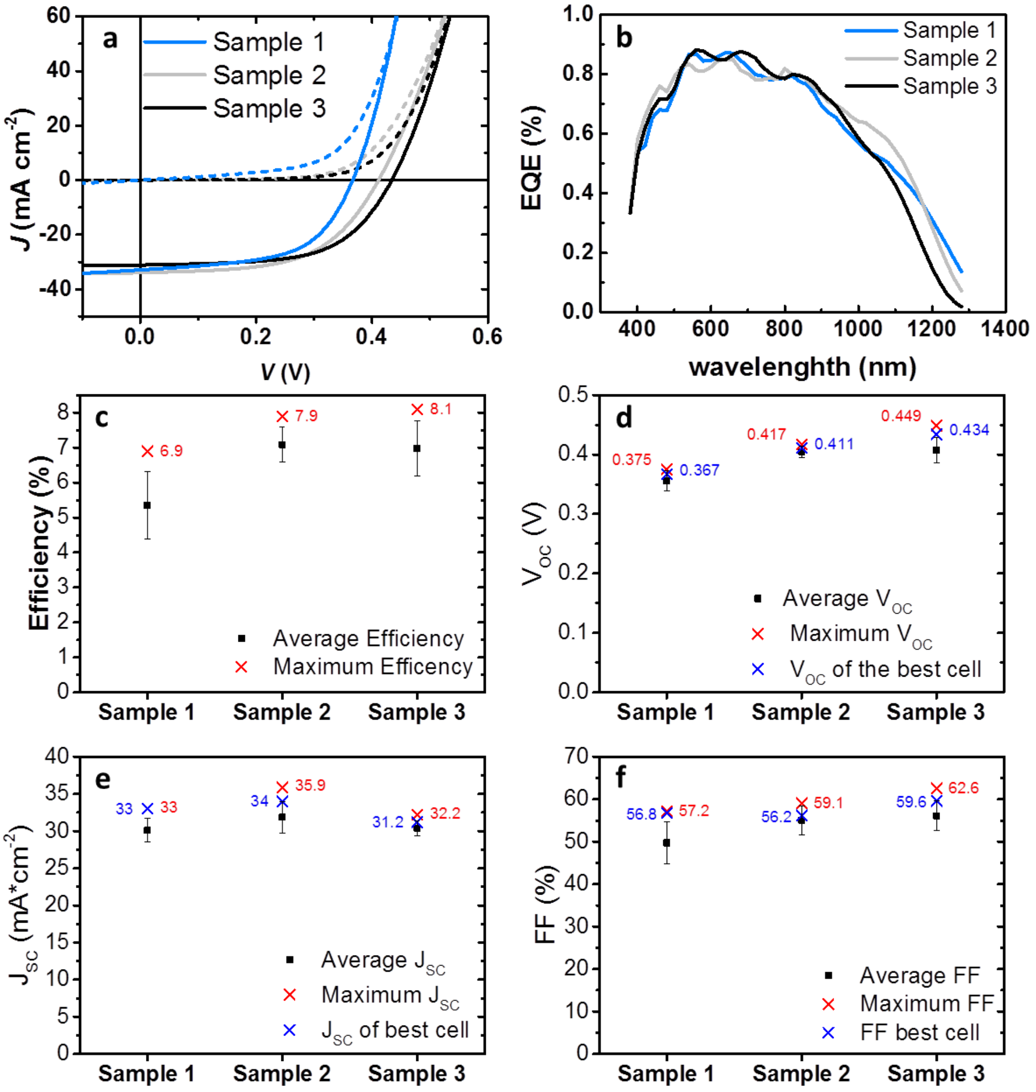

Figure 7.5 a) Current density – voltage (JV) curves and b) EQE of the best solar cells of each sample of this study. c), d), e), and f) show a summary of the average and standard deviation of the main optoelectronic parameters for the different devices (based on an average of 9 representative cells from each sample). Maximum values and the values for the best cells (highest efficiency) of each sample are also represented.

Variations in the crystal structure that the CZTSSe material adopts leads to different optoelectronic properties. In order to discuss the V_{OC} increase observed in the devices, several considerations regarding the bandgap dependency with the crystal structure of CZTSSe compounds need to be taken into account. Using different calculation methods, it is found that there could be a variation of around 150 meV between CZTSe in the kesterite or stannite crystal structure [163-165]. Rey *et al*., in an experimental study of the order-disorder transition in CZTSe co-evaporated thin films, observed an increase in bandgap from 0.94 to 1.06 eV after an ordering procedure. It is also important to consider how different point defects generated by differences in composition could induce significant differences in the bandgap. Charge compensated defect clusters have been calculated to be present in high concentration and to highly contribute to the non-stoichiometry of CZTSe. In particular $[V_{Cu} + Zn_{Cu}]$ induces a downshift of the valence band maximum and an upshift of the conduction band minimum [11].

In the previous section, it was shown that Raman and GIXRD measurements performed in the absorber layers suggest that the concentration of $[V_{Cu} + Zn_{Cu}]$ defect clusters increases with decreasing Cu content. This constrains the disorder in the Cu-Zn *2c* and *2d* positions, thus, increasing the Eg of the CZTSe absorber layers leading to an increase in the V_{OC} of the fabricated solar cells. In addition, while the Cu content in the CZTSe absorber layers decreases and the Zn/Sn ratio increases, in theory, it has been predicted that the concentration of the detrimental complex $[2Cu_{Zn} + Sn_{Zn}]$ decreases, producing a downshift of the conduction band edge and reducing electron trapping, thus increasing the solar cell performance [11].

7.4 Concluding remarks

CZTSe absorber layers with a variation of Cu-poor and Zn-rich content have been synthesised in order to investigate the correlation of modifications observed in the crystal structure with the optoelectronic properties of CZTSe devices. Raman spectroscopy suggests an increase in [V_{Cu} + Zn_{Cu}] defect clusters as the [Cu/(Zn+Sn)] ratio decreases and [Zn/Sn] ratio increases. This is observed from the change in intensity of the band at around 170 cm^{-1} relative to the band at 197 cm^{-1}. Le Bail analysis has been performed for the X-ray diffraction patterns of the CZTSe absorber layers in grazing incidence configuration. In the same compositional trend, while the lattice parameter *a* remains constant, *c* decreases. J-V results showed a dependence of the V_{OC} values on the Cu content ranging from 367 to 434 mV as the Cu concentration decreased in the absorbers. EQE shows that the increase in the maximum achievable V_{OC} appears to be linked to a widening of the bandgap. The best solar cell was based on the absorber layer with the lowest Cu content and yielded an efficiency of 8.1% with a fill factor of 59.8 %, J_{SC} = 31.1 mA/cm^2 and V_{OC} = 434 mV. It has been proposed that the widening of the bandgap is attributed to an increase of the concentration of the [V_{Cu} + Zn_{Cu}] defect cluster which induces ordering in the Cu/Zn (001) planes of the CZTSe. The results observed in the series of the presented devices show a good agreement with theoretical calculations regarding the influence of the defect clusters on the optoelectronic properties of CZTSSe solar cells. This chapter also demonstrates that the changes implemented in the selenisation process with respect to the samples produced for chapter 5 and 6 led to a significant improvement in the quality of the films, producing highly efficient CZTSe devices and introduces the reasonable next step in this research: the optimisation of this selenisation process. The first approach towards a better understanding of the influence of the properties of the CZTSe absorbers and how they are influenced by the processing conditions after the modifications will be covered in the next chapter with a study of the influence of the temperature in this process.

8 The influence of conversion temperature on the synthesis of Cu-poor Zn-rich CZTSe

The aim of the chapter is to present the investigation that explored the temperature of the synthesis process of CZTSe absorber layers used for solar cells. The previous chapter discussed the influence of Cu content in Cu-poor and Zn-rich CZTSe absorbers synthesized at 500º C that led to an 8.1 % efficient solar cell. In chapter 8, the structural and optical properties of the CZTSe absorbers processed at different temperatures are presented. This aims to improve the knowledge of the influence of processing conditions on material properties. Advanced characterization techniques such as PL and photoluminescence excitation (PLE) were used to assess the quality of the CZTSe processed at the temperatures investigated.

This chapter is, in part, based on the publication:

J. Márquez-Prieto, M. V. Yakushev, I. Forbes, J. Krustok, P. R. Edwards, V. D. Zhivulko*, et al.*, "Impact of the selenisation temperature on the structural and optical properties of CZTSe absorbers," *Solar Energy Materials and Solar Cells,* vol. 152, pp. 42-50, 2016.

8.1 Motivation and state of the art

The conversion process used to form absorber layers is one of the key steps in the fabrication of high performance CZTSe solar cells. This has been clearly demonstrated throughout this thesis, absorbers produced with the selenisation conditions chosen for the samples discussed in chapter 6 yielded non-photoactive devices. When significant changes were implemented to optimise this process, high performing solar cells were produced, as shown in chapter 7. This chapter investigates the influence of the conversion temperature.

In literature, a range of selenisation temperatures has been reported to be suitable for processing CZTSe absorbers for highly efficient solar cells. The reactive annealing process for a 11.2% CZTSe solar cell, reported by IBM [16], was carried out at very high temperature (590 ^{o}C) whereas for a 10.4% CZTSe solar cell, reported by IMEC, the absorber layer was selenised at 460 ^{o}C [81]. This large variability in the process conditions between different groups, that produce high efficiency solar CZTSe solar cells, suggests that the selenisation parameters need to be optimised for the specific precursor and selenisation system design used for the conversion. Therefore, a comprehensive study of selenisation temperature and its relationship to the electronic properties of the absorber layers and parameters of subsequent solar cells is needed to optimise the quality of the conversion process.

In addition to characterisation techniques such as Raman spectroscopy and XRD, photoluminescence (PL) is an effective technique for the study of defects in semiconductors [166]. Low temperature PL spectra of CZTSe thin films with strong Cu deficiency and Zn excess (compositional requirements for the absorber layer in high performance solar cells [11, 162, 167]) are dominated by a broad and asymmetrical band attributed to band tail related recombination [168-170]. To gain a better understanding of the defect properties it is important to study correlations of spectroscopic parameters with the knowledge acquired about the microstructure of the CZTSe thin films produced for this thesis and fabrication parameters used. The spectroscopic parameters presented in this chapter resulted from detailed PL analysis.

To interpret the data gained from PL measurements, it is essential to have reliable values of the bandgap E_g. Photoluminescence excitation (PLE) is one technique which can be used to determine E_g and it does not require a *p-n* junction. However, to the best of our knowledge the use of PLE on kesterites has been reported only for the sulphide branch of these materials [171].

8.2 Specific experimental details

Cu-Zn-Sn precursors from the same batch that yielded the highest efficiency device presented in chapter 7 (Sample 3 - 8.1%) were used for all the absorbers discussed in this chapter. The chapter aims to review the influence of the conversion temperature for the precursors giving the best performing devices. The selenisation process described in section 3.3.2 was used in all cases, with the only variation being that of the temperature of the 15 minutes step. In the previous chapter, the samples were selenised at 500 ºC. For this chapter, a series of three CZTSe absorbers are studied synthesised at 450, 500 and 550 ºC originated from the same precursor batch. For an easier understanding of the results, these samples with be labelled as Sample 1-450, Sample 2-500 and Sample 3-550 respectively. The results presented for Sample 2-500 can also apply to Sample 3 in the previous chapter. This is because the precursor used for Sample 2_500 in this chapter was from the same precursor batch as sample 3 in Chapter 7 and the same selenisation process was used.

8.3 Results

8.3.1 Microstructure and composition

The top SEM views of the Samples 1-450, 2-500 and 3-550, are shown in figure 8.1 (a), (b) and (c), respectively. Qualitatively, a progressive increase of the grain size is observed as the selenisation temperature was increased. This is consistent with the results observed in section 5.3.3 with the conversion process based on a Se evaporated cap layer. In the image corresponding to Sample 1-450, grains with flat plate type morphology are also observed. This type of morphology has been attributed in the literature to the presence of $Sn(Se,S)_2$ secondary phases [65] as indicated in figure 8.1 (a).

The elemental compositions of the films, determined by EDX are shown in table 8.1. All the CZTSe absorber layers exhibit a strong Cu deficiency and a weak excess of Zn. With a similar composition, CZTSe solar cells with high V_{OC} and efficiencies exceeding 8% were reported in chapter 7 for a selenisation temperature of 500 ºC [90]. In table 8.1, it is can be seen that as the selenisation temperature increased, the atomic % of Cu increases. A monotonic decrease of the concentration of Sn and Se in the samples is also observed with increase in selenisation temperature.

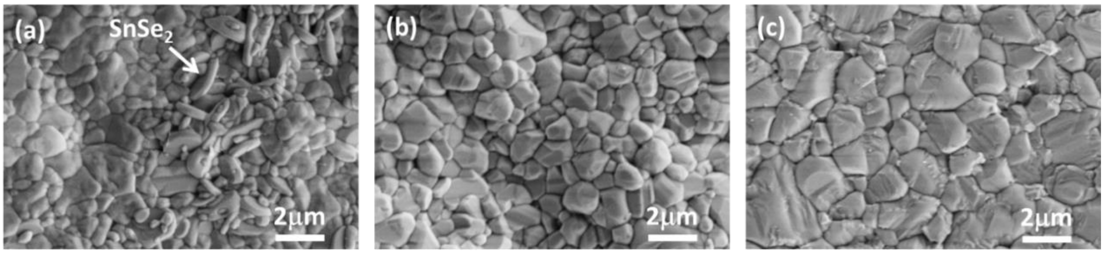

Figure 8.1 Top view SEM micrographs of the as deposited Sample 1-450 (a), Sample 2-500 (b) and Sample 3-550 (c), respectively.

Table 8.1. EDX elemental composition of Sample 1-450, Sample 2-500 and Sample 3-550.

	Cu (at. %)	**Zn (at. %)**	**Sn (at. %)**	**Se (at. %)**	**Cu/(Zn+Sn)**	**Zn/(Cu+Sn)**
Sample 1-450	18.8	14.7	13.7	52.9	0.66	0.45
Sample 2-500	19.3	16.2	13.1	51.3	0.66	0.50
Sample 3-550	20.5	15.8	12.9	50.8	0.71	0.47

Sn and Se loss has been attributed in literature to the decomposition of the CZTSe compound, which is enhanced as the temperature increases [150]. In order to see if the Sn and Se loss were enhanced near the surface, the composition of the samples are measured at lower acceleration voltage (10 kV), therefore, decreasing the penetration depth of the electron beam and ensuring that compositional information was acquired from the near the surface region of the films.

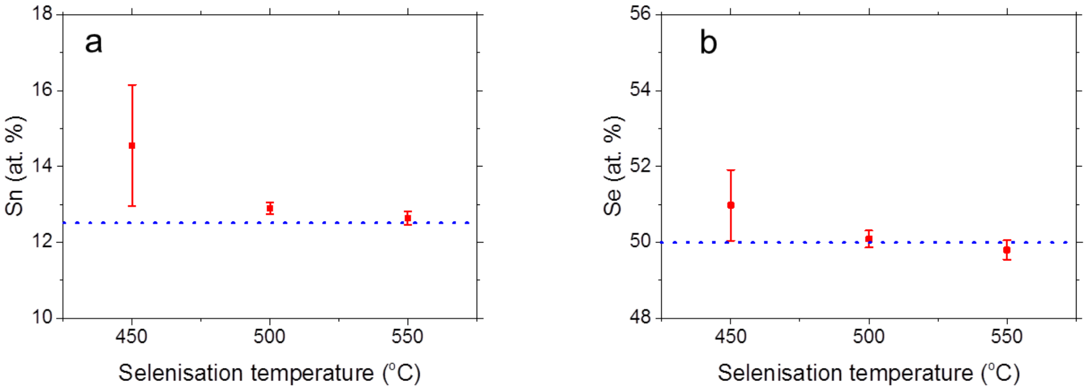

Figure 8.2 Plots showing the evolution of the mean Sn content (a) and Se content (b) as the selenisation temperature was increased with the standard deviations. The blue dotted lines are located for guidance at 12.5% of Sn content in (a) and 50% of Se content in (b), which correspond to the values of the stoichiometry of CZTSe 2:1:1:4.

Figure 8.2 shows the evolution of the Se and Sn content as the selenisation temperature increases confirming the loss of these elements towards the surface of the samples. In this case, as already mentioned in chapter 5, the interpretation of the compositional trends when secondary phases are present in the samples can lead to mistakes. In Sample 1-450, features associated with Sn-Se binary phases have been found at the surface of the film. This fact could lead to an increase of the counts of Se and Sn, and this may also explain why the standard deviation of the composition (10 points measured) is greater for the Sample 1-450. The measurements performed at 10 kV, also shows that the Se content for Sample 3-550 decreases even below 50 at. %.

8.3.2 XRD of the CZTSe absorbers

XRD patterns of the absorber layers are shown in figure 8.3. The formation of tetragonal CZTSe is confirmed for the whole range of temperatures tested in agreement with previous studies [117, 157]. In the diffractogram of Sample 1-450, it is possible to observe the most intense peak at 40^o, attributed to metallic Mo used as a back contact. As the selenisation temperature increases, this peak starts to decrease in intensity and it disappears for Sample 3-550 which has been selenised at the highest temperature. The opposite trend occurs with the broad reflections attributed to the presence of $MoSe_2$ at around 32^o showing an increase in intensity as the selenisation temperature increases. The total conversion of the metallic Mo into $MoSe_2$ is observed, explaining why a good electrical contact with the back of the device made from Sample 3-550 could not be reached, making the electrical characterization of this sample impossible, as it will be discussed in the following sections. The difractogram of Sample 1-450 shows two narrow peaks at 14.4^o and 30.8^o which are consistent with the presence of $SnSe_2$ (PDF numbers: 01-089-2939 23-602) and also in agreement with the presence of grains with the typical flat plate morphology of $SnSe_2$ observed in the SEM micrograph of this sample, as shown in figure 8.1 (a).

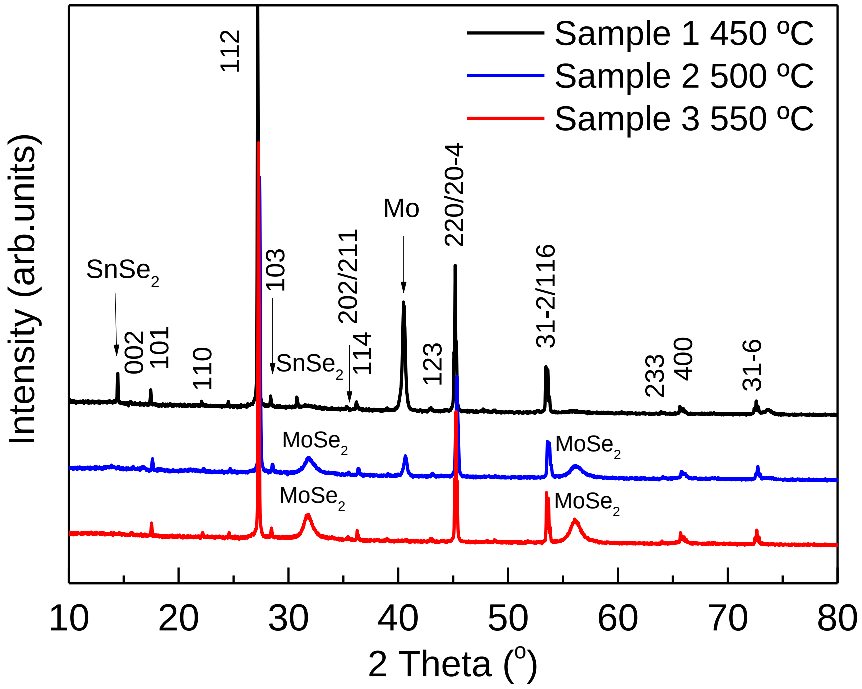

Figure 8.3 XRD patterns of CZTSe (phase indexed) films on Mo coated glass selenised at different temperatures.

8.3.3 Raman of the CZTSe absorbers

Figure 8.4 shows the normalised Raman spectra for the three films. All the peaks observed in the spectra, with the exception of a peak at 184 cm^{-1} observed for Sample 1, can be attributed to the CZTSe phase [116]. Different possible phases have been considered for assignment of the peak at 184 cm^{-1}. Marcano et al. reported Raman spectra of the monoclinic Cu_2SnSe_3 (CTSe) phase [134], with the most intense peak appearing at 180 cm^{-1}. The most intense Raman peak for $SnSe_2$ has been experimentally observed at 184 cm^{-1}. It was also theoretically predicted at 187 cm^{-1} [172] which in addition to the observations of this phase in the XRD pattern of this sample clarifies that the peak at 184 cm^{-1} appears to be due to the presence of $SnSe_2$. The inset of figure 8.4 shows the evolution of the FWHM value of the A mode at 197 cm^{-1} of CZTSe. A progressive decrease in the FWHM values is observed as the selenisation temperature is increased. This reduction is associated with an improvement of the crystal quality, which reduces the possible presence of phonon confinement effect and increases the phonon lifetime (reduction of the dispersion in the phonon energies) [173].

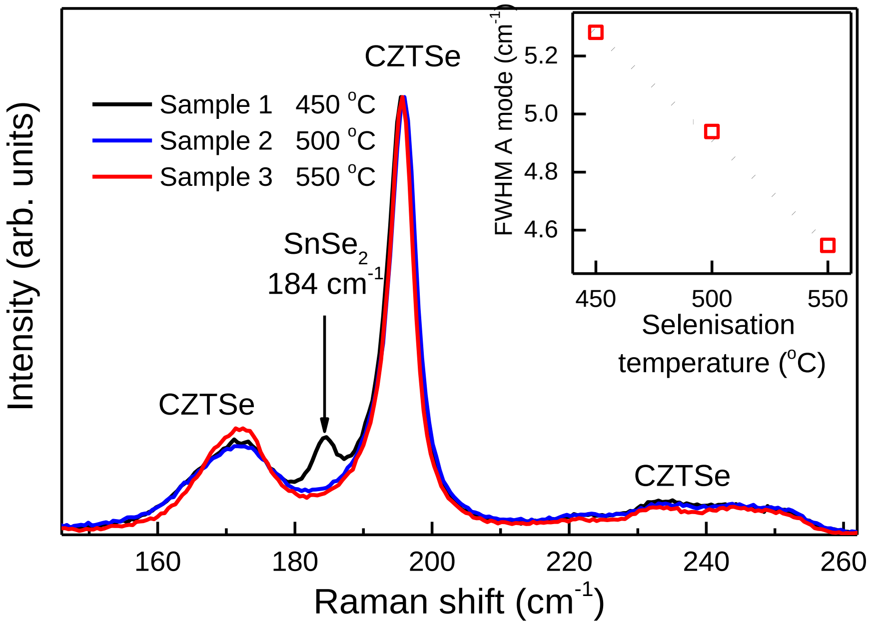

Figure 8.4 Raman spectra of the CZTSe samples selenised at ifferent temperatures. The inset shows the variation of FWHM of the most intense CZTSe mode.

8.3.4 Solar cell properties

Devices were produced with the CZTSe absorber layers selenised at different temperatures. The electrical parameters of the best solar cells prepared with the CZTSe absorber layers at 450°C and 500°C are also shown in table 8.2, with efficiencies up to 3.2% and 7.4% respectively. The best cell fabricated from Sample 2- 500^{o}C, yielded a V_{OC} value of 421 meV, which is similar to the one achieved for the best CZTSe solar cell reported in literature, but the J_{SC} is lower by about 10 mA cm^{-2} [16]. The smaller value of current density compared to the world record CZTSe solar cell is partly due to the use of a thick TCO layer of approximately 700 nm, in order to protect the solar cells during measurements, since no metallic grid was applied. In addition, no antireflection coating was used in the devices reported here which would be expected to increase the efficiency by about 1 % of the absolute value.

The efficiency, J_{SC}, V_{OC} and FF values obtained for Sample 2-500 are comparable and within the standard distribution bars of the values obtained for Sample 3 of chapter 7 (8.1%) suggesting that the selenisation process is reproducible.

Table 8.2 Electrical parameters of the solar cells prepared with the CZTSe films.

Sample	**Voc (mV)**	**Jsc (mA/cm^{2})**	**FF (%)**	**Eff (%)**
Sample 1-450	336	26.5	35.2	3.2
Sample 2-500	421	30.2	58	7.4
Sample 3-550	This sample could not be measured			

The J-V curves of the solar cells made with film 1-450^{o}C and film 2-500^{o}C are shown in figure 8.5. The J-V curves of Sample 3-550 could not be measured due to a total consumption of the metallic Mo used as back contact of the devices due to its conversion into $MoSe_2$ as evidenced in the XRD patterns. The clear increase in the performance observed for the sample selenised at 500 °C compared to 450°C may be due to the fact that, within the detection limits of the techniques used in this study, no secondary phases could be detected for that sample. In addition, an apparent grain growth with temperature, observed in the SEM top view images and the Raman results previously presented, indicated an increase of the crystalline quality.

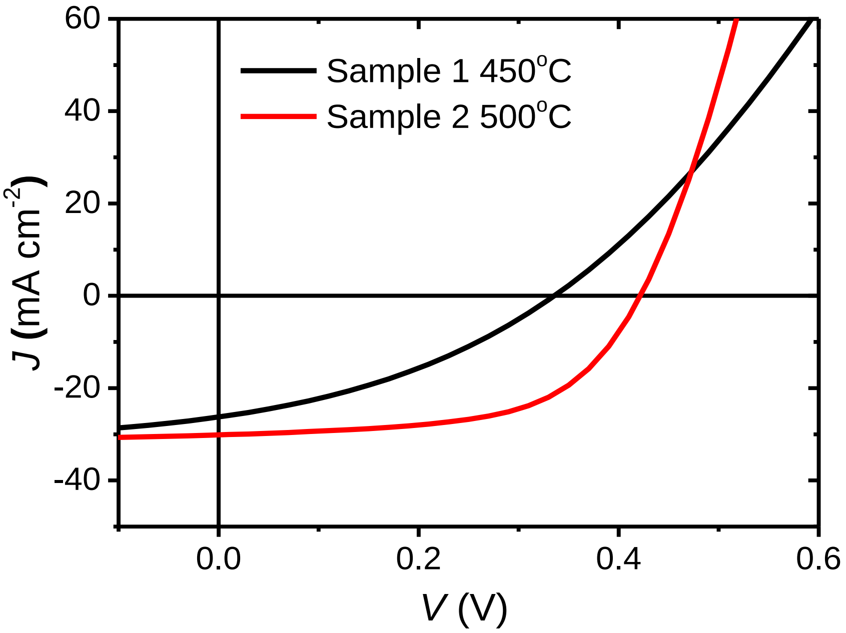

Figure 8.5. Current density – voltage (J-V) curves of the best solar cell made with Sample 1-450 and with Sample 2-500.

8.3.5 Analysis of the PL recombination mechanisms

The optical properties of the CZTSe absorbers synthesised at different selenisation temperature have been analysed by temperature depend PL spectroscopy. A detailed analysis of the PL recombination mechanisms of this series of samples has been published elsewhere [174]. This subsection will highlight the most relevant points, focusing on the PL at low temperature, to support the discussion of this chapter.

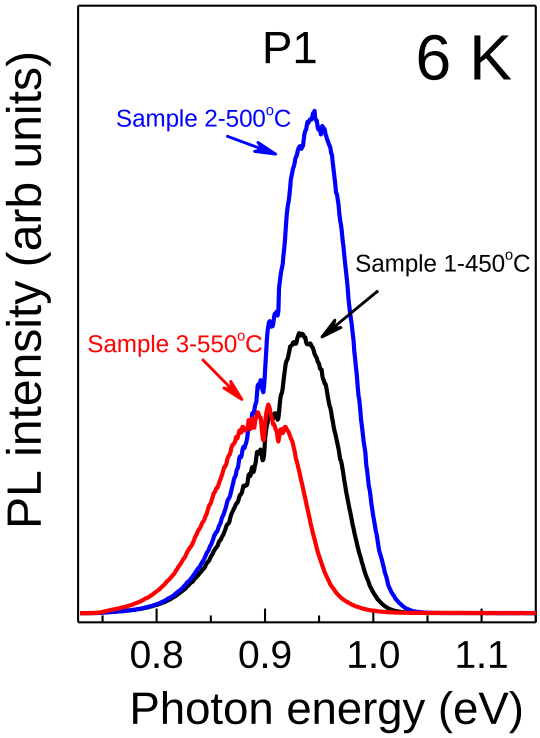

Figure 8.6 PL spectra from the films measured at 6 K, 0.053 W/cm^2 excitation and similar optical alignment for the CZTSe absorber layers converted at 450, 500 and 550 °C.

The PL spectra of the films, measured at a temperature of 6 K and at similar optical alignments and laser excitation energy and shown in figure 8.6, revealed a high intensity, broad asymmetrical band (P1) with a maximum at 0.934 eV (Sample 1-450), 0.944 eV (Sample 2-500) or 0.898 eV (Sample 3-550). The high energy slope of P1 has a higher gradient than the low energy slope. Features associated with water vapour absorption can also be seen at around 0.9 eV.

By increasing the selenisation temperature, from 450 ^{o}C to 500 ^{o}C, the band intensity is increased, and a blue shift of about 10 meV in the spectral position is observed whilst leaving the full width at half maximum (FWHM) unchanged, at 84 meV. Further temperature increase to 550 ^{o}C decreased the intensity to below that at 450^{o}C with an associated red shift in the spectral position by 46 meV with respect to that in Sample 2, and broadened the FWHM to 100 meV. Spectral positions and FWHM of the P1 bands in the films are shown in table 8.3.

Table 8.3 Spectral characteristics of the P1 PL band measured at 6 K, bandgaps E_g measured by PLE, average depths of potential fluctuations γ and activation energies E_a of the P1 band temperature quenching for the Samples 1, 2 and 3.

	Sample 1-450	**Sample 2-500**	**Sample 3-550**
P1 E_{max} (eV)	0.934	0.944	0.898
P1 FWHM (meV)	84	84	100
P1 *j*-shift (meV/decade)	11	12	15
E_g (eV) (PLE)	1.05	1.03	1.05

Excitation dependency analysis of the PL spectra measured at 6 K was also performed and is shown in figure 8.7. The j-shifts extracted from this analysis are also indicated in table 8.3. In all cases, the P1 band shows significant shifts to higher energies with laser power increase, whereas neither FWHM nor the asymmetric shape of the P1 band changes. The shift rate (*j* – shift) increases from 11 to 12 meV per laser power decade with selenisation temperature rise from 450 to 500^{o}C suggesting a slight increase in the compensation level in Sample 2. For further rise of the selenisation temperature, the *j*-shift increases to 15 meV per decade indicating a more significant increase in the compensation level.

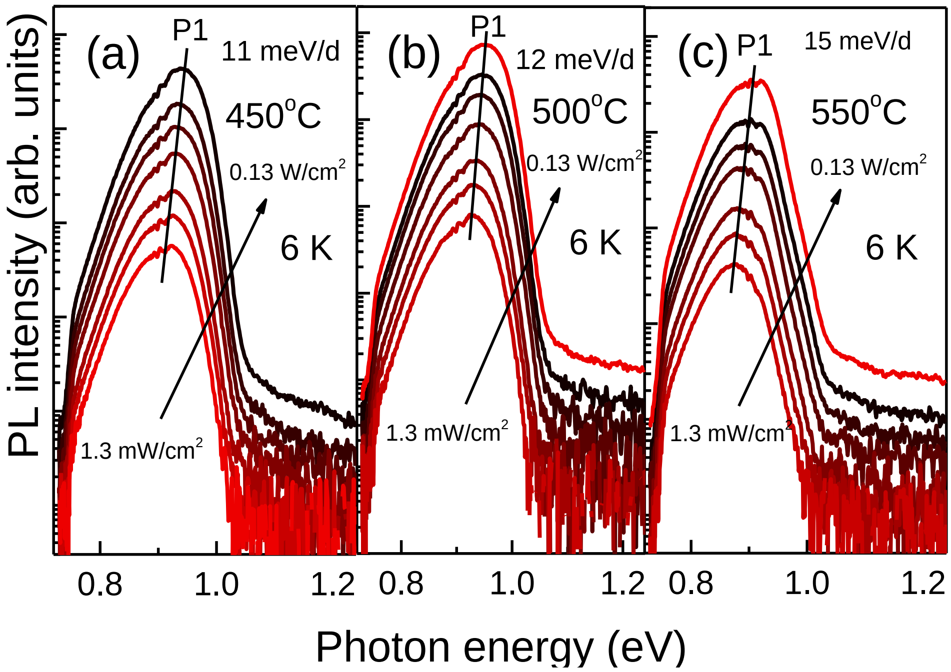

Figure 8.7 Excitation intensity dependencies of PL spectra in Sample 1 (a), Sample 2 (b) and Sample 3 (c) measured at 6 K.

Such significant *j*-shifts, observed for P1 along with its asymmetric shape at low temperatures are characteristic of band tail related recombination mechanisms [175, 176]. Tails in the electron and hole densities of states, at energies below the conduction band E_c, or above the valence band E_v, are formed in highly doped semiconductors by spatial potential fluctuations generated by high concentrations of randomly distributed charged defects [177].

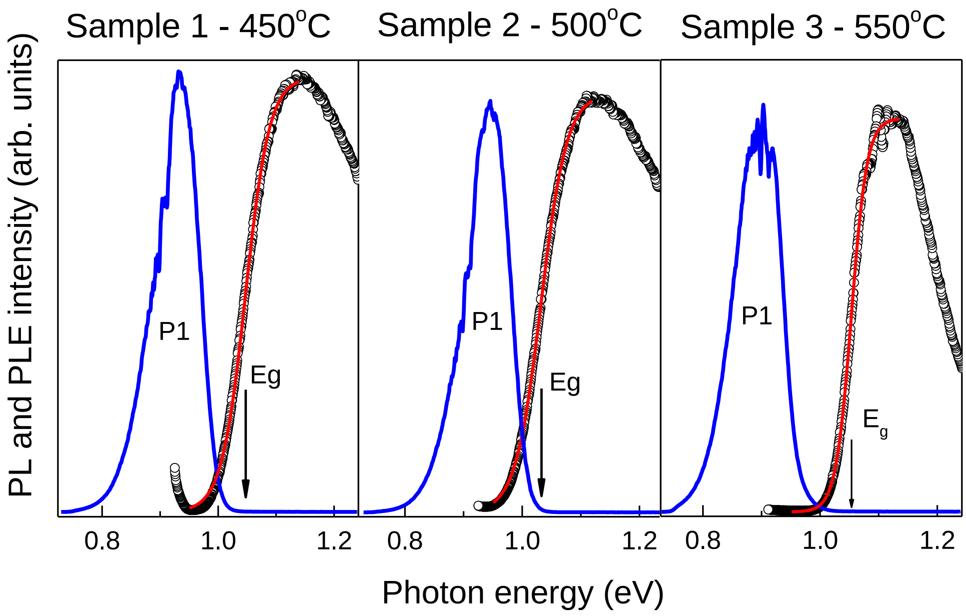

Figure 8.8 PLE spectra (measured at the maximum of the P1 band) and PL spectra of Sample 1 (a), Sample 2 (b) and Sample 3 (c) measured at 4.2 K. Red lines are the results of fitting.

The PLE spectra of the three samples are shown in figure 8.8, along with the normalised PL spectra of the samples and the fitting used to calculate the bandgap. The PLE spectra show broadening which suggests the presence of sub-bandgap absorption states associated with band tails. To take into account such a broadening the low energy sides of the PLE spectra, representing absorptance $\alpha(E)$, are fitted with sigmoidal shapes $\alpha(E)=\alpha_0/(1+\exp(E_g - E)/\Delta E)$, where E_g is the bandgap and ΔE is a broadening parameter equivalent to the Urbach tailing energy . The best fits for each film are shown in figure 8.8 by red lines. Further details of the model used to calculate the bandgap have been described elsewhere [174]. The bandgap values resulting from the calculations are shown in table 8.3.

8.4 Discussion

All the three films show significant copper deficiency with [Cu]/[Zn+Sn] below 0.8. It is possible to observe in table 8.1 that the Cu content in the samples increases and the Sn and Se content decrease as the selenisation temperature rises. The evolution of the Sn and Se content can be clearly seen in figure 8.2, where for Sample 1-450, the Sn and Se contents are the highest. For this film, the standard deviation is significantly larger than for the other samples. The presence of $SnSe_2$ near the surface of this sample might induce an increase of the Sn count in this analysis, giving an overestimated value of the atomic Sn concentration by this method. Within the limits of detection of the XRD and Raman techniques used in this study, no secondary phases were detected for these samples near the surface. Therefore, it is assumed that the average compositional values mainly come from the kesterite grains for Samples 2-500 and 3-550. As in the previous chapter, the off-stoichiometric CZTSe will be of the group A-type, where electrically neutral defect clusters V_{Cu}+Zn_{Cu} are expected to be present in high concentration [178] as was discussed in the previous chapter in detail.

Selenisation or annealing of CZTSe results in a loss of tin [150, 162]. This might be one of the reasons why a reduction of the Sn content is observed with increasing selenisation temperature (table 8.1 and figure 8.2). The decrease of Sn and Se content might be associated with an evaporation of Sn-Se binary phases. This is consistent with the changes shown in figure 8.3 and figure 8.4, for which the XRD patterns and Raman spectra show evidence of the presence of $SnSe_2$ in Sample 1-450 whereas in Samples 2-500 and 3-550 at higher selenisation temperatures this phase is not detected. After the selenisation step, no Se was visually found to be remaining in the crucibles in any of the processes. The decrease in the concentration of Se observed in figure 8.2 could be associated with the decomposition of the kesterite [179]. For the case of the pure sulphide kesterite, Scragg *et al.* reported that, if the vapour pressure of CZTS is higher than the partial pressure of S at the sample, then the kesterite decomposes into the binaries and gaseous sulphur [179]. The CZTSe vapour pressure increases with temperature meaning that, in order to stabilise the surface of the film, higher Se partial pressure should be needed with increasing temperature. Unfortunately, it is quite difficult to monitor the Se partial pressure at the surface of the film and its evolution with time. Qualitatively, it is possible to predict that, with increasing temperature and time, the Se vapour would tend to leave the reactor or be absorbed by the graphite. Bearing this in mind, it is expected a higher decomposition of the CZTSe film in this series as the temperature increases, since the time, and the amount of Se source have been kept constant.

Within the limits of detection of the characterisation techniques used in this study, the formation of binaries could not be detected for Sample 2-500^{o}C and Sample 3-550^{o}C. $SnSe_2$ has been detected in Sample 1-450^{o}C and it is possible to speculate that its formation is due to the off-stoichiometry of the sample rather than from the decomposition of CZTSe. V_{Se} and V_S have been reported to be isolated deep donor defects according to Chen *et al.* [11]. At high temperatures, normal for reactive annealing, it was reported for the sulphur case that the formation energy of V_S is low, making concentrations up to $2x10^{19}$ cm^{-3} possible [180]. It is therefore possible to conclude that formation of V_S and V_{Se} is likely to be prior to the decomposition of the CZTSe into the binary phases. The decrease of concentration of Se is observed in figure 8.2, which for the case of Sample 3 -550 goes below 50%, might be an indication of an increase of the concentration of V_{Se} as the temperature increases.

The Raman data also confirm the presence of $SnSe_2$ in Sample 1-450. The selenisation temperature increase from 450 to 500°C results in the disappearance of the $SnSe_2$ in Sample 2 leaving all the other features in the spectra almost unchanged. The further temperature rise from 500 to 550°C increases the intensity of the 172 cm^{-1} peak, which can be interpreted as a reduction of the probability to form the defect complexes V_{Cu}+Zn_{Cu} [116, 117]. This is consistent with the increase of Cu content shown in table 8.1.

The structural quality of semiconductors can be compared by the integrated PL intensity (IPLI) of their radiative photoemission measured at similar conditions [166]. The higher the intensity, the lower is the level of non-radiative recombination and scattering on defects of photo-excited electrons and holes. Such a criterion is also valid for semiconductors used in the solar cell absorber layer [162, 181]. This pattern can be seen in figure 8.6 where the solar cells of Sample 2 - 500 were 7.4% efficient, and show a significantly higher PL intensity at 6 K (by a factor of 1.8 in terms of IPLI ratios) than Sample 1 - 450. Sample 3 shows significantly lower PL intensity than Sample 2 (by a factor of 2.3 in terms of IPLI ratios). This trend suggests that a solar cell made from Sample 3, if the problem of contact is solved, would be less efficient than those made from Sample 1 and Sample 2. At first sight, considering a reduction of the FWHM of the mode at 197 cm^{-1} in Raman spectroscopy shown in figure 8.4 and an increase of the grain size with increasing temperature shown in figure 8.1, one would expect an increase of the PL intensity with increasing the selenisation temperature as observed from Sample 1-450°C to Sample 2-500°C. Since this behaviour is not observed for Sample 3-550°C, further considerations should be taken into account to explain the reduction of the PL intensity for this sample.

Non-radiative recombination can occur via deep defects in the bandgap limiting the PL yield [123]. An increase of the concentration of V_{Se}, predicted by a decrease of the Se content in this sample as the temperature increases from 500°C to 550°C, could explain the strong decrease of the PL intensity that was observed for the sample synthesised at the highest temperature. In fact, the same conversion conditions at 550 °C were tested with the same batch of precursors but using a more resistive Mo back contact, which was not fully selenised. As a result of this experiment, the devices fabricated had efficiencies below 2%, confirming the predictions based on IPLI analysis.

The bandgaps of the studied films, determined by PLE measurements, gives values over 1.00 eV. This increase of the bandgap might be due to the presence of high populations of the defect complex $V_{Cu}+Zn_{Cu}$ which is consistent with the reported restraining effect of such complexes on the Cu/Zn disorder [156], and also in agreement with the results shown in chapter 7. The PLE measurements give a value of the bandgap for Sample 2- 500 °C of 1.03 eV which is measured at 6K. From the inflection point of the EQE of the equivalent solar cell discussed in chapter 7 (Sample 3 of Ch. 7), which is measured at room temperature, a bandgap value of 1.07 eV was calculated. If it is assumed that the bandgap increases with the decrease of temperature, as reported for Cu-poor Zn-rich CZTSe [182], it can be concluded that the inflection point bandgap calculation method from the EQE might provide significantly overestimated values.

8.5 Concluding remarks

In this chapter, the temperature of the selenisation step has been reviewed after implementing the changes in the conversion process for the samples discussed in chapter 7. A progressive improvement in the crystal quality of the CZTSe phase was observed according to a decrease of the FWHM of the main A mode of the Raman spectra of the absorbers. This was supported by an observed increase in the grain size with increasing temperature as observed by SEM, in agreement with the results discussed in chapter 5. The films were used to fabricate solar cells with efficiencies of 3.2 % (selenisation at 450^{o}C) and 7.4% (selenisation at 500^{o}C). It was not possible to measure the solar cell with the absorber synthesised at 550 ^{o}C because the Mo back contact was fully converted into $MoSe_{2.}$ Analysis of the low temperature PL spectra of the samples suggests that the absorber with the best optical quality was the one synthesised at 500 ^{o}C. The PL spectrum of the absorber processed at 550 ^{o}C indicates that non-radiative recombination was greater in this sample, and this might affect the device performance. It has been tentatively attributed that the decrease of radiative recombination in the sample fabricated at 550 ^{o}C is due to an increased loss of Sn and Se that would be detrimental for the device performance.

The best sample fabricated for this chapter has been processed with the same conditions as the best CZTSe device (8.1% efficient) discussed in chapter 7, and the J-V parameter of this device are comparable, indicating a certain level of reproducibility of the synthesis process. These results suggest that careful control of the synthesis conditions needs to be performed to achieve high quality CZTSe absorber layers in terms of structural and optical properties.

9 Cu_2SnS_3 as absorber layer for thin film solar cells

In chapter 5, the synthesis of CTSe was reported as part of the study of the phase evolution of CZTSe. The experimental findings and the literature research to understanding the phase formation of CTSe, allowed the author to gain an interest in CTS and its potential as an earth abundant absorber layer. During the development of the experimental work for this thesis, particularly during my secondment at the Helmholtz-Zentrum in Berlin, under the supervision of Dr. Thomas Unold, the author of this thesis had opportunity to synthesise CTS films in a co-evaporation chamber that had been prepared for the synthesis of this material.

This chapter is based on the publication:

J.A. Marquez Prieto, S. Levcenko, J. Just, H. Hampel, I. Forbes, N.M. Pearsall, T. Unold, "Earth abundant thin film solar cells from co-evaporated Cu_2SnS_3 absorber layers", Journal of Alloys and Compounds, 689 (2016) 182-186.

9.1 Motivation and state of the art

Cu-Sn-S derived materials are gaining increasing interest as absorber layers produced from earth abundant elements for application in thin film solar cells. Efficiencies up to 4.6% have been already achieved using the same device architecture used for CIGS and for CZTSSe based materials [37]. In the Cu-Sn-S system, several compounds with different stoichiometry have been reported in literature, including Cu_2SnS_3 [41, 42, 47, 183-186], Cu_3SnS_4 [184, 186-189], Cu_4SnS_4 [183], $Cu_2Sn_3S_7$ [183] and $Cu_4Sn_7S_{16}$ [190]. Particularly, Cu_2SnS_3 is so far the ternary compound of the Cu-Sn-S system that has been studied most for making solar cells.

The similarity between Cu_2SnS_3 and CZTSSe allows the groups developing kesterite solar cells to be able to quickly adapt their facilities to investigate this ternary material, and is another reason for the rapid increase of the number of publications on this material. Several synthesis approaches have been proven to be suitable for producing Cu_2SnS_3 films including sputtering [186], reactive sputtering [191], electrodeposition [47, 49], pulsed laser deposition [46] and several non-vacuum routes [38, 192].

Cu_2SnS_3, has been reported to adopt several crystal structures including cubic zincblende type structure (*F*-43*m*) [184, 186], tetragonal stannite type structure (*I*-42*m*) [184, 186, 190] and monoclinic structure (*C*1*c*1) [41-43, 47, 185, 193] depending on the temperature used for the synthesis. With increasing temperature, a change in the crystal structure has been predicted to unit cells with higher symmetry, changing from monoclinic to orthorhombic, then tetragonal and cubic [194]. However experimental results in literature suggest that, when the synthesis process has a temperature below 550ºC, Cu_2SnS_3 normally adopts cubic or tetragonal structure [184, 186] and when the synthesis temperature is above 550ºC the monoclinic structure predominates [42, 193]. A large discrepancy in the value of the bandgap of Cu_2SnS_3 in its different crystal structures is also found in literature. For the monoclinic form, the presence of two bandgaps is found, one at 0.92-0.93 eV and a second one around 0.99 eV [42, 43, 47, 193]. Fernandes et al reported a bandgap of 1.35 eV for the tetragonal Cu_2SnS_3 and 0.96 eV for the cubic structure [184].

Most of the Cu_2SnS_3 absorber layers that have been used to produce solar cells have been synthesised in a two stage process with a reactive annealing step at temperatures higher than 550ºC under a sulphur or sulphur and tin atmosphere. This high temperature step resulted in Cu_2SnS_3 adopting the monoclinic structure.

However, for low temperature or moderate temperature process, it is difficult to find reports of solar cells in which the Cu_2SnS_3 is not monoclinic. In addition to the fact that in low temperature synthesis, the grain growth is more limited, the cubic CTS structure might present mid gap states and band tailing, making it difficult to make efficient solar cells out of this structure [195].

In the work reported in this chapter, the synthesis of Cu-Sn-S absorber layers used a single step co-evaporation method and a substrate temperature of 400 ºC. Microstructural analysis of the absorber layers based on SEM, Raman spectroscopy and X-Ray diffraction analyses is presented. It was found that for these experiments Cu_2SnS_3 crystallises in the cubic structure and the presence of other Cu-Sn-S phases in the absorber layers has been identified.

9.2 Specific experimental details

The synthesis of the CTS absorbers has been described in chapter 3, section 3.6. The optical transmission and reflectance spectra were acquired by Hannes Hempel from the Helmholtz Zentrum Berlin with a Perkin-Ellmer UV-Vis spectrometer. The absorbers were lifted-off from the Mo coated SLG substrates in order to perform this measurement.

9.3 Results and discussion

9.3.1 Composition and morphology

The absorber layers showed a Cu/Sn ratio of around 1.7 and S/(Cu+Sn) ratio around 1. Figure 9.1 shows an SEM cross sectional view of the solar cells processed for this study. The CTS absorber layer is about 1 μm thick and shows columnar-like morphology, suggesting that the films are highly textured. A similar morphology was also reported for CTS samples grown by RF sputtered from Cu_2S and SnS targets and deposited onto substrates heated to around 300º C [186], suggesting that this columnar type growth is typical for low temperature synthesis.

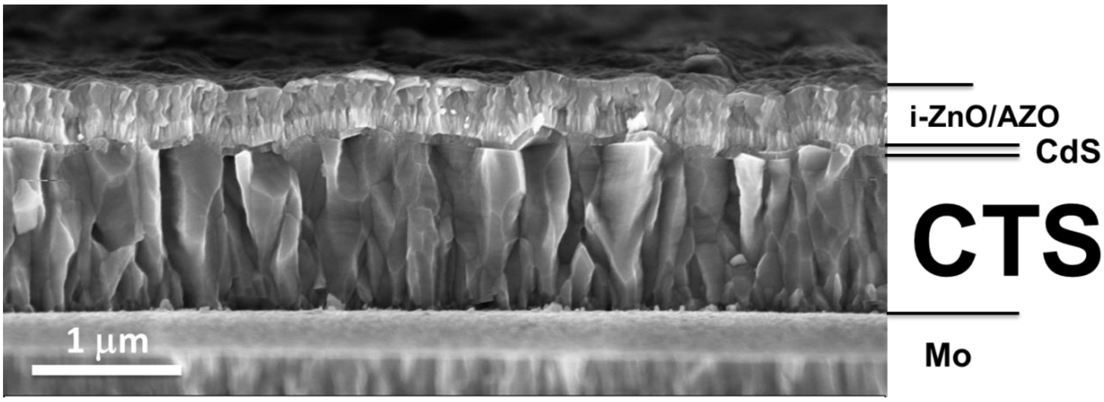

Figure 9.1 SEM cross section of a complete CTS device. The different layers are identified in the right hand side of the image.

9.3.2 XRD of the CTS absorbers

Figure 9.2 shows the X-Ray Diffraction (XRD) pattern of the CTS absorber layer acquired in Bragg-Brentano configuration. An intense peak observed at 28.3º can be attributed to Cu_2SnS_3 in the cubic (*F*-43*m*, ICSD 43532), the tetragonal (*I*-42*m*, ICSD 50965) or the monoclinic (*C*1*c*1, ICSD 91762) structure. No other peaks can be observed related to this phase. Therefore, it is difficult to determine the crystal structure based only on the information provided by the XRD pattern. The single peak suggests that the films are preferentially orientated, which is consistent with the columnar growth morphology observed for the cross sectional SEM images in figure 9.1. The inset of figure 9.2 shows a magnification of the XRD pattern between 20 and 50º. The diffractogram shows the presence of low intensity peaks at 27.4 and 30.7º that can be attributed to the presence of orthorhombic Cu_3SnS_4 [189]. The presence of Cu_3SnS_4 in films has been already reported to coexist with Cu_2SnS_3 [186, 195], however the relatively low intensity of these reflections in comparison with the strong peak attributed to Cu_2SnS_3 suggests that the amount of the Cu_3SnS_4 orthorhombic phase is low.

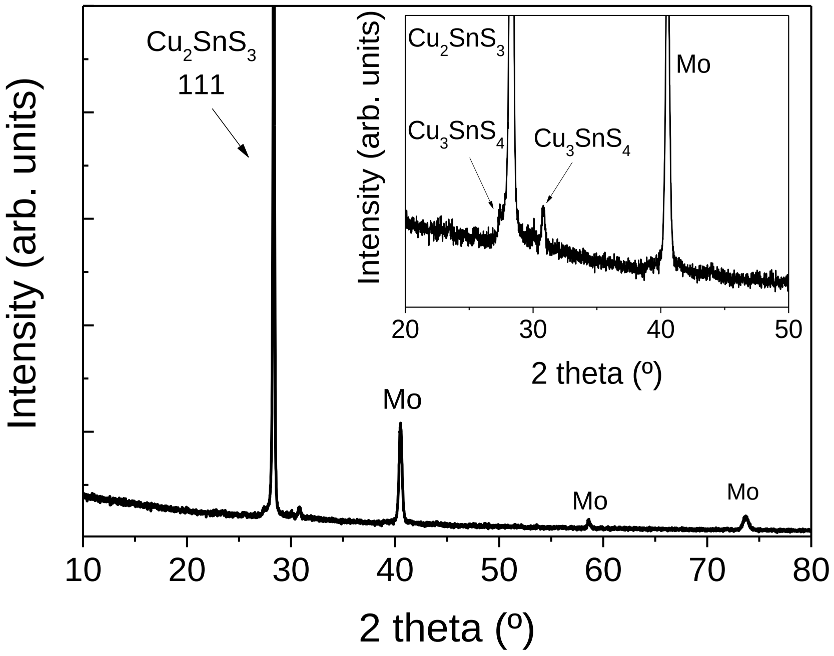

Figure 9.2 X-Ray diffraction pattern of the CTS absorber layer. The inset shows a magnification of low intensity range between 20 and 50º. The phases assigned to each peak are labelled in the plots.

9.3.3 Raman and optical transmission spectra

In order to confirm the crystal structure of the CTS absorber layers Raman spectroscopy was performed on the sample and it is shown in figure 9.3. The peaks observed in the spectrum have been qualitatively fitted with Lorentzian functions to determine the position of the observed Raman modes. Two high intensity peaks at 303 and 359 cm^{-1} suggest that Cu_2SnS_3 is mainly present in the cubic structure, in accordance with the studies reported by Fernandes et al. [52, 184]. Unfortunately, no calculations of the phonon spectra of the different crystal structures of Cu_2SnS_3 have been reported up to now and the assignments for the cubic Cu_2SnS_3 are made based on reported experimental data. In addition, lower intensity peaks at 319 cm^{-1} and 337-346 cm^{-1}can be observed. In the literature, peaks at these positions have been correlated with the presence of orthorhombic Cu_3SnS_4 [52, 189], which agrees with its identification by XRD presented in figure 9.2. The position of the modes for the orthorhombic Cu_3SnS_4 to perform the fitting for this phase was adjusted according to the phonon spectrum calculated by Dzhagan et al [189]. Raman measurements with λ_{exc} =633nm would potentially be very sensitive to the modes of Cu_3SnS_4, due to near resonant conditions [196], since a bandgap of 1.6 eV has been reported for this phase [184]. This would explain the fact that modes related to this phase are clearly observed even when its concentration in the film is low, as suggested by the low intensity peaks in the XRD patterns corresponding to Cu_3SnS_4. Also a Raman mode at 265 cm^{-1} is observed, which cannot be attributed to a specific phase. Although calculations have predicted Raman active modes close to this frequency [189], the experimental data in literature for orthorhombic Cu_3SnS_4 does not agree with this mode being the most intense for this phase [189].

A bandgap value of 1.02 eV was calculated form the Tauc plot generated with the optical transmission spectrum of a lifted-off CTS absorber as shown in figure 9.3. Strong sub-bandgap absorption can be observed up to 0.85 eV, in good agreement with theoretical calculations of the density of states for cubic disorder CTS that have shown strong band tails for this material [195].

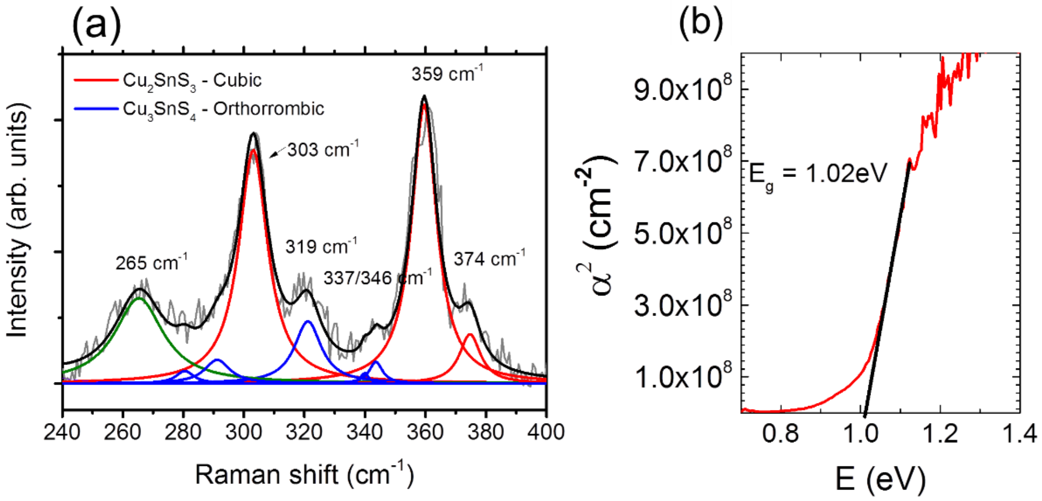

Figure 9.3 (a) Raman spectrum of the CTS absorber (dark grey). Lorentzian fitting of the Cu_2SnS_3 cubic modes (red), Cu_3SnS_4 (blue) and an unidentified mode (green). The black line shows the sum of the fits. (b) Tauc's plot generated from the optical transmission and reflection spectrum of a lifted-off CTS absorber.

9.3.4 Solar cell properties

The current-voltage (J-V) characteristic of the best performing device is shown in figure 9.4.a. The efficiency of the device was 1.8%, with a short circuit current density (J_{SC}) of 28 mA/cm^2, an open circuit voltage (V_{OC}) of 147 mV and a fill factor (FF) of 44% for a total cell area of 0.5 cm^2. The reason for the low value of V_{OC} is not well understood but several possibilities can be considered. The cubic structure of Cu_2SnS_3 has been reported to be highly disordered implying band tailing, compositional inhomogeneities at the nanometre scale and potential fluctuations [195]. Also, a cliff-like band offset has been reported for the CdS-CTS junction [197]. Assuming that this is the case for this device, a reduction of the interface bandgap would reduce V_{OC} and increase the recombination at the interface of the device [36]. In addition, the presence of other phases found in the absorber layer, such as Cu_3SnS_4, could contribute detrimentally, increasing the metallic character of the absorber layers and decreasing the performance of the solar cells due to an increase of shunting paths [186].

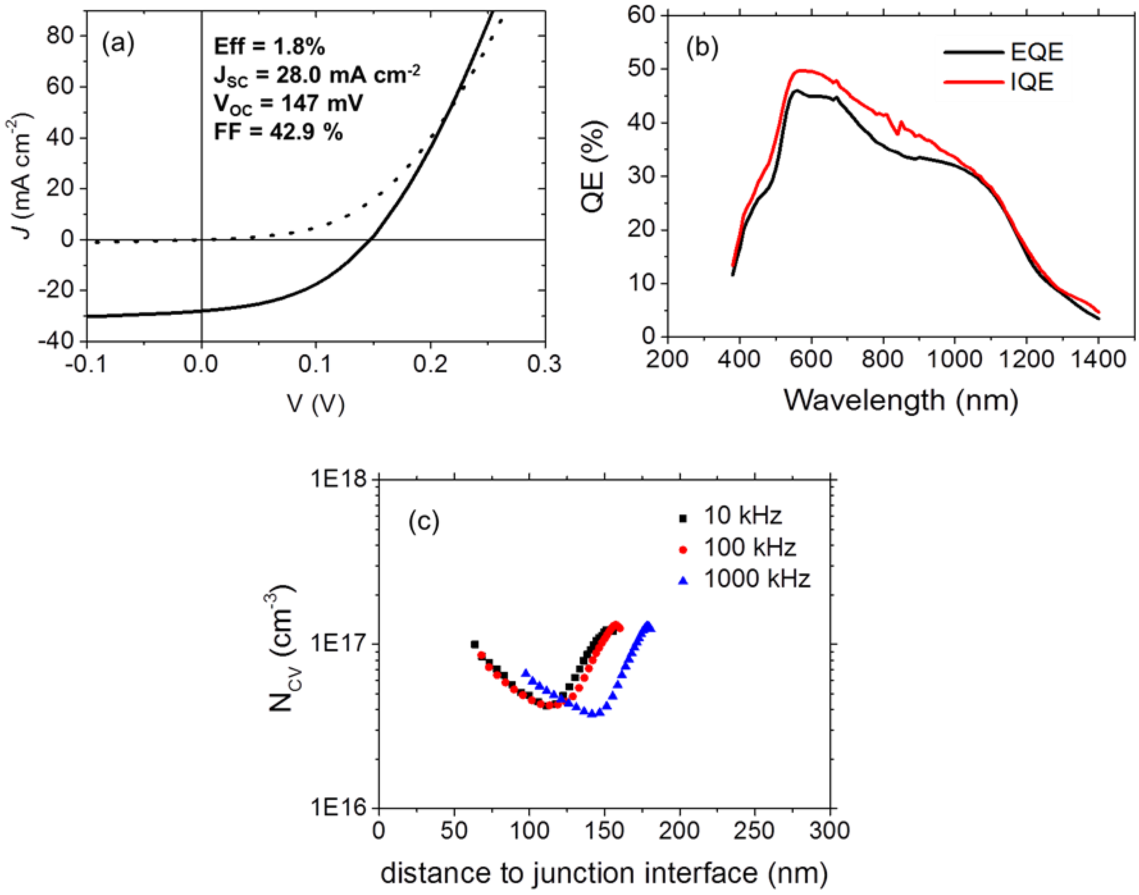

Figure 9.4 (a) Dark and illuminated JV curves of the best CTS cell. (b) External (black line) and internal (red line) quantum efficiency of the best solar cell. . (c) CV profiles measured at 10 kHz, 100 kHz and 1000 kHz

The External Quantum Efficiency (EQE) and the Internal Quantum Efficiency (IQE) are shown in figure 9.4.b. The IQE (λ) was calculated from the ratio of the EQE (λ) and the spectral absorbance of the device as IQE (λ) = EQE (λ) $/ [1 - $R ($\lambda$)] . A step between 650 and 800 nm is observed in the EQE, which is not evident in the IQE, suggesting that it is due to interferences of the device layers. At wavelengths above the bandgap of CdS (510-520nm) both, the EQE and IQE start to decay significantly, suggesting that a measurable contribution to the J_{SC} occurs from hole generation in the CdS. This contribution ceases for wavelengths with energies below the bandgap of CdS in agreement with a small collection function in the bulk of the absorber [5]. Nakashima et al. reported the appearance of the same decay when the EQE was measured without white light bias [37] as shown in figure 9.5, suggesting that the light intensity dependent properties of CTS solar cells should be further studied to contribute to the progress of this material.

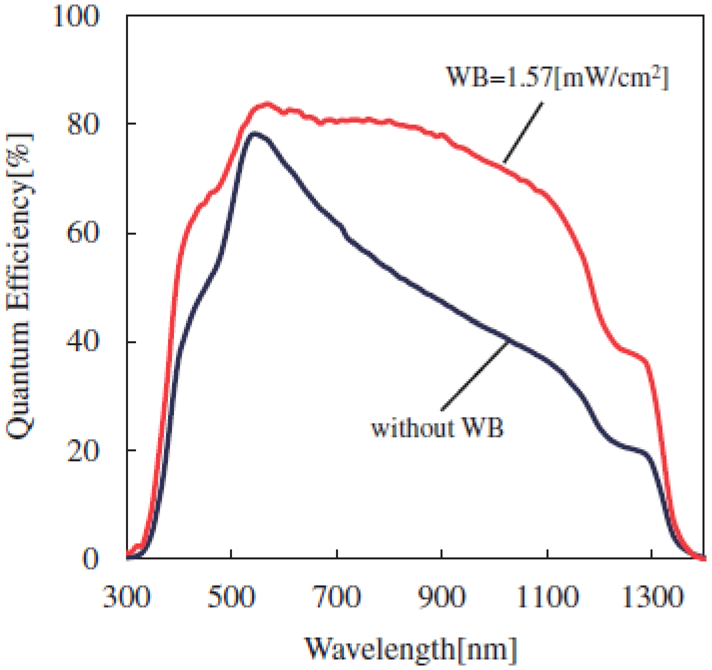

Figure 9.5 EQE spectra from the world record CTS solar cell. The plot shows the difference between the EQE acquired with (red line) and without (blue line) white light bias. Image taken from [37].

The bandgap was calculated from the inflection point of the EQE and IQE giving a value of approximately 1.06 eV. Strong band tailing is also observed in the QE, in agreement with the Tauc plot presented in figure 9.2.b and in accordance with previously reported theoretical calculations for the disorder cubic structure [195]. The presence of this strong band tailing could be a potential issue for the development of CTS solar cells when the absorber layer adopts the cubic structure. This band tail is not observed in the EQE of devices made out of the monoclinic Cu_2SnS_3 where two transitions are observed at around 0.93 and 0.99 eV [37] (see figure 9.5), suggesting that this crystal structure could be a better candidate for CTS solar cells.

J_{SC} has been calculated by integrating the EQE with the AM 1.5 solar spectrum yielding a value of $J_{SC\ (EQE)}$ =16.4 mA/cm^2 which is significantly lower than the value measured in the JV curve (28.0 mA/cm^2). This behaviour has been previously observed in other CTS solar cells found in literature when the EQE has been measured without white light bias [37], suggesting again that the optoelectronic properties of these CTS solar cells are affected by the light intensity.

CV measurements were performed on the CTS device and are shown in figure 9.4.c. Charge carrier concentrations of 3 - 5 x 10^{16} cm^{-3}and a depletion region width of around 120 nm were estimated for this solar cell by assuming a static dielectric constant ε_0=10. The charge carrier concentration values measured for this solar cell are significantly lower than has previously been reported for cubic CTS, where the lowest values were around 7 x 10^{17} cm^{-3} and 10^{21} cm^{-3} when Cu_3SnS_4 was present. These values are considered to be too high for a p-type absorber layer in a photovoltaic device [186].

9.4 Concluding remarks

In this chapter, the synthesis of CTS absorber layers by single step co-evaporation with a nominal substrate temperature of 400ºC has been described. A combination of Raman, SEM and XRD analysis leads to the conclusion that the Cu_2SnS_3 is highly textured and adopts a disordered cubic structure. The presence of Cu_3SnS_4 was detected in all the samples and SnS was detected when the absorbers were synthesised with a high Sn flux. A 1.8% efficient CTS/CdS/i-ZnO/Al:ZnO solar cell was obtained with J_{SC} of 28 mA cm^{-2}, V_{OC} of 147 mV and a FF of 42.9 %. A bandgap value of 1.06 eV was extracted from the inflection point of the EQE. The J_{SC} calculated by integrating the EQE with the AM 1.5 solar spectrum shows disagreement with the measured J_{SC} indicating that the devices are affected by changes in electronic properties that depend on the illumination intensity. A charge carrier concentration of 4 x 10^{16} cm^{-3} is extracted from C-V measurements with a depletion region of approximately 120 nm. The work presented in this chapter demonstrates for the first time the fabrication of CTS solar cells with absorbers synthesised at a moderate temperature of 400 ^{o}C. The limitations of the solar cells presented in this chapter has been discussed and it is suggested that although a low temperature depositions process can be used for the synthesis of CTS absorbers, the properties of higher temperature absorbers crystallising in a monoclinic structure might be more suitable for solar cells due to a significant reduction of sub-bandgap absorption.

10 Summary, Conclusions and recommendations for further studies

This chapter summarises the research performed in this thesis and presents the main conclusions. Then, insights are provided about the future of CZTSe and derived kesterite materials. The future of the use of Cu_2SnS_3 as an absorber layer for thin film PV is also discussed.

10.1 Development in CZTSe absorber layers and solar cells

In this thesis a synthesis process for depositing CZTSe thin film absorber layers has been developed by a two stage method consisting in the deposition of a Cu-Zn-Sn metallic precursor layer by sputtering followed by a selenisation step. Several conclusions have been made during the development of this synthesis process, as detailed below.

10.1.1 CZTSe absorbers growth

- The Cu-Zn-Sn metallic precursors are mainly composed of Cu-Zn and Cu-Sn alloys showing a uniform atomic distribution in depth. If the composition of the precursor is very Cu poor or very Sn rich, elemental Sn is also present in the precursor inducing a rougher morphology of the films as specified in section 6.3.1.
- The selenisation of Cu-Zn precursors resulted in the formation of $Cu_{2-x}Se$ and ZnSe phases that segregated forming large grains over a wide range of temperatures (380-550 ºC). In the same range of temperatures, the

selenisation of Cu-Sn precursors resulted in uniform polycrystalline thin films of Cu_2SnSe_3 crystallising in a monoclinic structure.

- The formation of the tetragonal CZTSe phase has been demonstrated for selenisation temperatures from 380 to 550 ºC. It has also been demonstrated that the microstrain in the films decreased with increasing selenisation temperature.
- The influence of the Cu content has also been explored, synthesising CZTSe thin films with compositions ranging from Cu-rich (Cu/(Zn+Sn)>1) to Cu-poor (Cu/(Zn+Sn)<1). It was concluded that the concentration of defects in Cu-rich and stoichiometric films was lower than in Cu-poor films. The grain sizes were larger in the Cu-rich films. A relative decrease in the intensity of the CZTSe modes in the Raman spectra appearing at 173 cm^{-1} has been correlated with Cu deficient compositions. This feature has been attributed to an increase of the concentration of the defect cluster (V_{Cu} + Zn_{Cu}) which is characteristic of the A-type CZTSe off-stoichiometry compositions.

10.1.2 CZTSe solar cells

- The influence of the Cu content of the CZTSe absorber layers on the device performance has been explored. The best devices were fabricated with absorber layers with very Cu-poor and Zn-rich compositions. These compositions led to CZTSe absorber layers with high concentration of (V_{Cu} + Zn_{Cu}) defect clusters as shown by Raman spectroscopy measurements. Bandgap widening and an increase of ordering in the Cu-Zn plane of the kesterite type structure of CZTSe was observed as the compositions of the films become more Cu poor. It was also identified that as the CZTSe absorbers become more Cu poor, the tetragonal deformation parameter (*c*/2*a*) of the CZTSe phase decreases, being in all cases below 1. The bandgap widening observed resulted in CZTSe solar cells with efficiencies over 8% and V_{OC} values even larger than the current world record for CZTSe devices.

- The selenisation step was also studied during the development of this thesis in order to maximise the solar cell performance. The conversion conditions leading to the best devices were identified using a high amount of Se in the reactor (~240 mg in pellets) with the following heating profile:

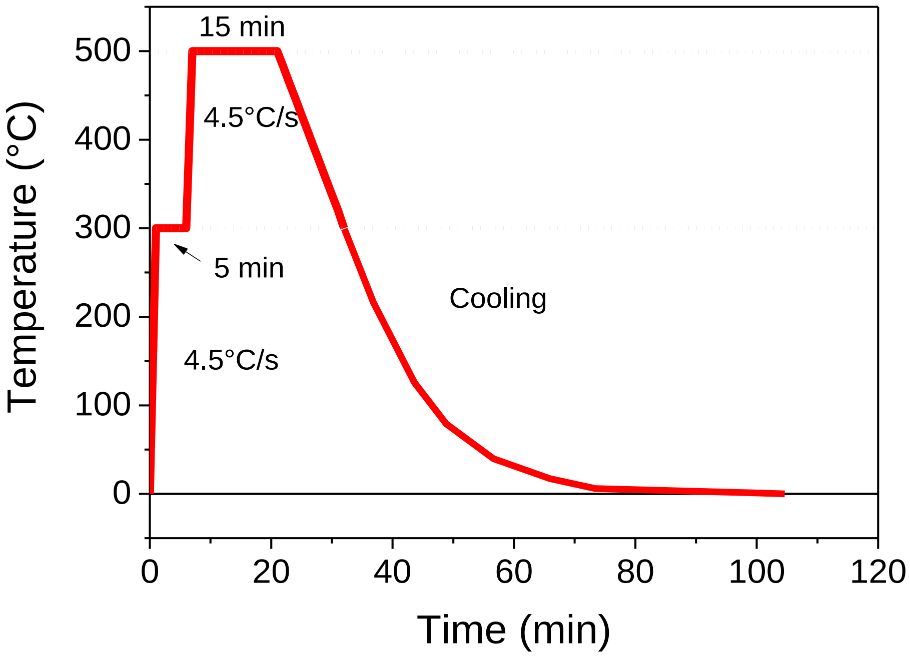

Figure 10.1 Heating profile used for the synthesis of the best solar cells of this thesis.

- Lower conversion temperatures (450 ºC) produced films with $SnSe_2$ secondary phases coexisting with the CZTSe phase. This resulted in devices showing shunting behaviour.

- Higher conversion temperatures (550 ºC) led to films where Sn and Se loss from the CZTSe becomes relevant, inducing defects in the film such as V_{Se}, which are detrimental for the device performance. Low temperature PL analysis of the absorbers synthesised at 550 ºC reveal high level of compensation and poorer optical properties compared to CZTSe absorbers synthesised at lower temperatures, suggesting that in the type of selenisation systems used in this thesis, moderate temperatures might help to prevent Se deficit in the films. For these films, the Mo layer was fully converted to $MoSe_2$. However, this problem could be assessed in future by varying the sputtering conditions of the Mo back contact in order to produce a layer less reactive with Se.
- As a final comment, it is important to clarify that the absolute values of the ideal selenisation conditions depend on many factors such as: the type of precursor, the composition of precursor, the chalcogen source used and the volume and geometry of the reactor. The conclusions presented in this section should therefore be interpreted qualitatively when different selenisation systems and types of precursors are being compared.

10.2 CTS absorber layers and devices

A low temperature co-evaporation process was demonstrated to be feasible to produce CTS absorber layers for PV applications. Devices with efficiencies up to 1.8% were fabricated with these absorbers. The solar cells are limited by a low V_{OC} and the possible origins of this have been discussed. The samples produced with this low temperature coevaporation process led to absorbers where Cu_2SnS_3 coexisted with small amounts of Cu_3SnS_4. Strong sub-bandgap absorption was observed in these absorbers, which will limit the applicability of this material for high efficiency solar cells if this issue is not resolved.

10.3 Revisiting goals of the project

In the first chapter, the general goals of this project were established:

- Synthesis and fabrication of CZTSe thin films with a potentially scalable method: sputtering of Cu-Zn-Sn metallic precursors followed by a reactive annealing step for the incorporation of Se and the optimisation of this process.
- Study of the phase evolution and formation of CZTSe by the synthesis approach described in this thesis.
- Study of the influence of the composition of the CZTSe absorber layers in its microstructural and optical properties
- Demonstration of the use of CZTSe absorbers in thin film PV devices and assessment of the conditions for maximising its performance.

The previous sections compiled the specific ways describing how these objectives have been accomplished, in which a synthesis route for efficient CZTSe devices has been proposed and the optimised conditions for this process have been defined. Variations of the composition of the CZTSe absorbers have also been studied. These variations resulted in the formation of defects on the CZTSe phase that were identified experimentally through the development of analysis techniques based on Raman spectroscopy and XRD. Correlations between the experimental findings of this project and the theoretical calculations related to defects found in the literature have been proposed.

10.4 Future of kesterites and closing recommendations

There is an important gap in record efficiencies between kesterite technologies (12.6%) [35] and the already commercialised CIGS (22.3%) [25] and CdTe (22.1%) [198] technologies. This gap makes clear that kesterites are in a continuing research and development period and their efficiencies need to be increased significantly to be able to become a competitive technology. In particular, the main difference in efficiency arises from a significantly lower value of V_{OC} of the kesterite solar cells in comparison to CdTe and CIGS. The difference between the optical bandgap of the absorbing material and the V_{OC} is commonly referred in literature as the V_{OC} deficit. This V_{OC} deficit is significantly higher for kesterites in comparison with CIGS and CdTe. The reasons of this high V_{OC} deficit in kesterites are still unclear. Recently, it has been concluded by several experts that the disorder of Cu/Zn atoms in the kesterite type structure does not have a major detrimental effect in this sense [198]. This was also discussed in chapter 7 where the increase in V_{OC} induced by a decrease of Cu content and disorder in the CZTSe was shown to be driven by a similar increase of the bandgap of the absorber material. Therefore, future work to close the gap in V_{OC} between kesterites and the parental technologies should be driven by testing the strategies that brought CdTe and particularly CIGS to overcome the 20% efficiency barrier.

Recent studies in single crystal CdTe devices demonstrated an increase of the V_{OC} of the solar cells of more than 100 mV compared to historical CdTe polycrystalline record devices [199]. This demonstrated that the bulk properties of CdTe should not limit the fabrication of solar cells with efficiencies above 25%. In the same study, group V elements were successfully used to dope the anion sites of the crystal structure [199], which is a technique that could also be explore for kesterites. Initial studies in single crystals are starting to be reported focused in structural, vibrational and optical properties [200-203]. Unfortunately, few studies can be found in the literature about single crystal kesterite materials which are focused in how the bulk properties could affect the solar cell performances. Hopefully, future reports on single crystals would help addressing if the bulk of kesterites will fundamentally limit the fabrication of devices with efficiencies above 20%.

For CIGS, two main research lines have been relevant in the development of this technology that have not yet been deeply explored for kesterites. The first one is the introduction of external dopants (particularly alkali elements). The second one is the fabrication of absorber layers with graded bandgaps.

In order to prove the relevance of alkali doping and post deposition treatments (PDT) in CIGS, solar cell data from Pianezzi's thesis is compared below to put in context the importance of these studies [96]. It was shown that without any alkali treatment their devices had an efficiency of 11.5% without antireflective coating (ARC), whereas with a controlled Na and K PDT the solar cells had efficiencies above 19% with ARC [96]. This is a clear demonstration of how important the control of the alkali doping led to massive improvements in the performance of this technology and therefore, they should be studied in depth for kesterites. In the case of alkali doping for CZTSSe materials, several reports concluded that Na induces some positive changes in kesterite solar cells as previously reported for CIGS:

- Increase of FF and V_{OC} [204]
- Increase of conductivity and carrier concentration [204]
- Accumulated at the grain boundaries [205]
- Improvement of grain growth [206]
- Increase of radiative recombination [207]

In the case of K, there are few reports in literature and this should also be explored for kesterites. Initial studies of the introduction of small quantities of other elements such as Li [76] and Ge [208] have been achieving promising results.

The bandgap grading, which has been a key in the success of CIGS solar cells has not been explored yet in depth in kesterites. Initial studies in the interface modifications by NREL reported that increasing the Zn content at the surface, induced an increase of the bandgap at the interface, increasing the V_{OC} of their CZTSe devices [85].

The bandgap of kesterite absorber layers can be tuned by changing the Selenium and Sulphur content from 1.0 eV to 1.5 eV respectively [164]. The record solar cells are made with the CZTSSe solid solution with an approximate bandgap of 1.1 eV [35]. In general terms, most groups report their best devices in the Se rich regime, either by making pure selenide kesterites or solid solutions with high Se content. However, the CZTSSe solar cells reported in literature shows a uniform distribution in depth of Se and S, therefore vertical bandgap gradient has not been clearly achieved with these elements.

Other strategies to change the bandgap of kesterite based devices have been successfully proved such as changes in the stoichiometry, as demonstrated in chapter 7, or the substitution of Sn by Ge [209]. Si could also be used for to replace Sn for bandgap widening. The introduction of Ag in the Cu positions of the kesterite type structure has also been tested and devices with efficiencies over 10% have been achieved [210]. All of these possible substitutions of elements should allow the implementation of strategies to grade the bandgap in kesterite absorbers in a similar way that helped the development of CIGS technology to increase the performance of the devices. It is also important to highlight that both, the substitutions of Ge and Ag induce an increase of the difference in stability between kesterite and stannite type structures [211]. This would reduce the probability of the presence of domains with stannite structure in polycrystalline films that might reduce the maximum achievable photovoltaic performance.

10.5 Future of CTS in PV

The future of CTS for photovoltaic applications remains uncertain. The results presented in this thesis demonstrate that devices can be synthesised with what has been reported as a disordered-cubic structure in literature [195]. It has also been proven that the absorber layers present a strong band tailing effect, which was predicted by theoretical calculations for this type of structure. The charge carrier concentration profiles extracted from C-V measurements suggest that the values are in a good range of values for efficient solar cells. This result does not agree with Baranowski et al. studies, which concluded that their CTS absorber layers had large values of carrier concentration and this was the main issue limiting the fabrication of solar cells with [186].

It also demonstrates that low temperature coevaporation could be a viable deposition route. And it is suggested that higher substrate temperatures are to be tested to prove that the monoclinic CTS can also be synthesised by this method. This material has been reported to have a sharper band edge and has led to the best device performance in literature [37].

The research in CTS still presents several unresolved questions that are needed to be answered to be able to provide a critical assessment of the future of this material. They can be summarised in the following points:

- Band alignment: few results can be found in literature about the alignment of bands between the CTS and the potential absorber layers. All of the devices reported in literature have been fabricated using CdS, and all of them show a low value of the V_{OC}. In order to understand if the CTS solar cell performance is strongly limited by interface recombination, more comprehensive studies of this need to be developed. This can be assessed by designing experiments to measure the band alignment between CTS and different candidates to be used as buffer layers. This would help finding appropriate materials to solve this issue.

- Light intensity performance dependence: the results reported in this thesis seem to point out that the devices perform differently when the light intensity is varied. This can be seen from the great difference in the J_{SC} values extracted from EQE without white light bias and the values measured in the solar simulator. A similar behaviour has been observed in the record device reported by Nakashima et al. [37], but it is the origin of this behaviour is not well understood as yet.
- Need of Ge addition: 6% efficient solar cells have been reported by introducing Germanium in the synthesis process of CTS [50]. It was reported that the main improvement was associated to a large increase in grain growth and bandgap widening. Unfortunately, it is not well understood how this affects the defect chemistry of the material, the band alignments and other properties, which have been demonstrated to be affected for the case of kesterite compounds [208, 209]. The use of Ge in the absorber layers has also the drawback of not being an earth abundant element.

Researchers studying the Cu-Sn-S family should try to answer the questions summarised above. This data would help determining if CTS has the potential to be used as an absorber layer fabricating solar cells with efficiencies over 10% in the next years.

Alternatively, some other new materials are starting to gain a great interest. Solar cells based on Sb_2Se_3 have been reported with efficiencies up to 5.6 %, this being a result that will guarantee more research in this material as an alternative inorganic absorber layer.

Fe_2SiS_4 and Fe_2GeS_4 have also been proposed as ideal alternative inorganic compounds containing earth abundant elements for photovoltaic applications [212]. This study was based on theoretical calculations and initial experimental results on powders [212]. However, there are no reports of solar cells fabricated out of these materials yet. The investigation of these materials is also expected to grow.

An increase of the number of materials available to be used in thin film PV will benefit the future development of these technologies. This would also help increasing their market share of thin film PV in future, particularly if the materials used are composed of earth abundant elements.

References

[1] A.E. Becquerel, Mémoire sur les effets électriques produits sous l'influence des rayons solaires, Comptes rendus de lÁcademie des sciences, 9 (1839) 145-149.

[2] W.G. Adams, R. Day, The Action of Light on Selenium, Proceedings of the Royal Society of London, 25 (1876) 113-117.

[3] D.M. Chapin, C. Fuller, G. Pearson, A new silicon p-n junction photocell for converting solar radiation into electrical power, Journal of Applied Physics, (1954) 676-677.

[4] IEA PVPS - Trends in Photovoltaic Applications (2015). [online] Available at: http://www.iea-pvps.org/index.php?id=trends0 [Accessed 21 Apr. 2016].

[5] R. Scheer, H.-W. Schock, Chalcogenide Photovoltaics: Physics, Technologies, and Thin Film Devices, Weinheim: Wiley-VCH., 2011.

[6] MIT Energy Initiative. (2016). The Future of Solar Energy. [online] Available at: http://mitei.mit.edu/futureofsolar [Accessed 21 Apr. 2016].

[7] R. Caballero, C.A. Kaufmann, T. Eisenbarth, T. Unold, R. Klenk, H.W. Schock, High efficiency low temperature grown Cu(In, Ga)Se_2 thin film solar cells on flexible substrates using NaF precursor layers, Progress in Photovoltaics: Research and Applications, 19 (2011) 547-551.

[8] A. Chirilă, P. Reinhard, F. Pianezzi, P. Bloesch, A.R. Uhl, C. Fella, L. Kranz, D. Keller, C. Gretener, H. Hagendorfer, D. Jaeger, R. Erni, S. Nishiwaki, S. Buecheler, A.N. Tiwari, Potassium-induced surface modification of Cu(In,Ga)Se_2 thin films for high-efficiency solar cells, Nat Mater, 12 (2013) 1107-1111.

[9] F. Pianezzi, A. Chirilă, P. Blösch, S. Seyrling, S. Buecheler, L. Kranz, C. Fella, A. Tiwari, Electronic properties of Cu(In, Ga)Se_2 solar cells on stainless steel foils without diffusion barrier, Progress in Photovoltaics: Research and Applications, 20 (2012) 253-259.

[10] S. López-Marino, M. Neuschitzer, Y. Sánchez, A. Fairbrother, M. Espindola-Rodriguez, J. López-García, M. Placidi, L. Calvo-Barrio, A. Pérez-Rodríguez, E. Saucedo, Earth-abundant absorber based solar cells onto low weight stainless steel substrate, Solar Energy Materials and Solar Cells, 130 (2014) 347-353.

[11] S. Chen, A. Walsh, X.G. Gong, S.H. Wei, Classification of lattice defects in the kesterite Cu_2ZnSnS_4 and $Cu_2ZnSnSe_4$ earth-abundant solar cell absorbers, Advanced materials, 25 (2013) 1522-1539.

[12] T.K. Todorov, K.B. Reuter, D.B. Mitzi, High-efficiency solar cell with Earth-abundant liquid-processed absorber, Advanced materials, 22 (2010) 156-159.

[13] B. Shin, O. Gunawan, Y. Zhu, N.A. Bojarczuk, S.J. Chey, S. Guha, Thin film solar cell with 8.4% power conversion efficiency using an earth-abundant Cu_2ZnSnS_4 absorber, Progress in Photovoltaics: Research and Applications, 21 (2013) 72-76.

[14] S. Delbos, Kësterite thin films for photovoltaics : a review, EPJ Photovoltaics, 3 (2012) 35004.

[15] J. Kim, H. Hiroi, T.K. Todorov, O. Gunawan, M. Kuwahara, T. Gokmen, D. Nair, M. Hopstaken, B. Shin, Y.S. Lee, W. Wang, H. Sugimoto, D.B. Mitzi, High efficiency $Cu_2ZnSn(S,Se)_4$ solar cells by applying a double In2S3/CdS emitter, Advanced materials, 26 (2014) 7427-7431.

[16] Y.S. Lee, T. Gershon, O. Gunawan, T.K. Todorov, T. Gokmen, Y. Virgus, S. Guha, $Cu_2ZnSnSe_4$ Thin-Film Solar Cells by Thermal Co-evaporation with 11.6% Efficiency and Improved Minority Carrier Diffusion Length, Advanced Energy Materials, 5 (2014) 1401362.

[17] A. Polizzotti, I.L. Repins, R. Noufi, S.-H. Wei, D.B. Mitzi, The state and future prospects of kesterite photovoltaics, Energy & Environmental Science, 6 (2013) 3171.

[18] T.M. Letcher, J.L. Scott, editors, Materials for a sustainable future, Royal Society of Chemistry, 2012.

[19] G. Zoppi, I. Forbes, R.W. Miles, P.J. Dale, J.J. Scragg, L.M. Peter, $Cu_2ZnSnSe_4$ thin film solar cells produced by selenisation of magnetron sputtered precursors, Progress in Photovoltaics: Research and Applications, 17 (2009) 315-319.

[20] J. Márquez-Prieto, M.V. Yakushev, I. Forbes, J. Krustok, P.R. Edwards, V.D. Zhivulko, O.M. Borodavchenko, A.V. Mudryi, M. Dimitrievska, V. Izquerdo-Roca, N.M. Pearsall, R.W. Martin, Impact of the selenisation temperature on the structural and optical properties of CZTSe absorbers, Solar Energy Materials and Solar Cells, 152 (2016) 42-50.

[21] A. Stanley, Cadmium sulfide solar cells, Applied Solid State Sciences, 5 (1975) 251.

[22] R. Hall, R. Birkmire, J. Phillips, J. Meakin, Thin-film polycrystalline $Cu_2S/Cd_{1-x}Zn_xS$ solar cells of 10% efficiency, Applied Physics Letters, 38 (1981) 925-926.

[23] A. Al-Dhafiri, G. Russell, J. Woods, Degradation in CdS-Cu_2S photovoltaic cells, Semiconductor science and technology, 7 (1992) 1052.

[24] L. Kazmerski, F. White, G. Morgan, Thin-film $CuInSe_2$/CdS heterojunction solar cells, Applied Physics Letters, 29 (1976) 268-270.

[25] Solar Frontier Achieves World Record Thin-Film Solar Cell Efficiency: 22.3%. (2015) [online] Available at: http://www.solar-frontier.com/eng/news/2015/C051171.html [Accessed 22 Apr. 2016].

[26] R. Caballero, M. Nichterwitz, A. Steigert, A. Eicke, I. Lauermann, H.W. Schock, C.A. Kaufmann, Impact of Na on $MoSe_2$ formation at the CIGSe/Mo interface in thin-film solar cells on polyimide foil at low process temperatures, Acta Materialia, 63 (2014) 54-62.

[27] R. Caballero, C.A. Kaufmann, T. Eisenbarth, T. Unold, S. Schorr, R. Hesse, R. Klenk, H.-W. Schock, The effect of NaF precursors on low temperature growth of CIGS thin film solar cells on polyimide substrates, physica status solidi (a), 206 (2009) 1049-1053.

[28] R. Caballero, C.A. Kaufmann, T. Eisenbarth, M. Cancela, R. Hesse, T. Unold, A. Eicke, R. Klenk, H.W. Schock, The influence of Na on low temperature growth of CIGS thin film solar cells on polyimide substrates, Thin Solid Films, 517 (2009) 2187-2190.

[29] P.T. Erslev, J.W. Lee, W.N. Shafarman, J.D. Cohen, The influence of Na on metastable defect kinetics in CIGS materials, Thin Solid Films, 517 (2009) 2277-2281.

[30] P. Jackson, D. Hariskos, R. Wuerz, O. Kiowski, A. Bauer, T.M. Friedlmeier, M. Powalla, Properties of Cu(In,Ga)Se_2 solar cells with new record efficiencies up to 21.7%, physica status solidi (RRL)-Rapid Research Letters, 9 (2015) 28-31.

[31] K. Ito, T. Nakazawa, Electrical and Optical Properties of Stannite-Type Quaternary Semiconductor Thin Films, Japanese Journal of Applied Physics, 27 (1988) 2094.

[32] T.M. Friedlmeier, N. Wieser, T. Walter, H. Dittrich, H. Schock, Heterojunctions based on Cu_2ZnSnS_4 and $Cu_2ZnSnSe_4$ thin films, in: 14th European PVSEC, (1997). 1242-1245

[33] H. Katagiri, N. Sasaguchi, S. Hando, S. Hoshino, J. Ohashi, T. Yokota, Preparation and evaluation of Cu_2ZnSnS_4 thin films by sulfurization of E ・ B evaporated precursors, Solar Energy Materials and Solar Cells, 49 (1997) 407-414.

[34] H. Katagiri, K. Jimbo, W.S. Maw, K. Oishi, M. Yamazaki, H. Araki, A. Takeuchi, Development of CZTS-based thin film solar cells, Thin Solid Films, 517 (2009) 2455-2460.

[35] W. Wang, M.T. Winkler, O. Gunawan, T. Gokmen, T.K. Todorov, Y. Zhu, D.B. Mitzi, Device Characteristics of CZTSSe Thin-Film Solar Cells with 12.6% Efficiency, Advanced Energy Materials, 5 (2014) 1401372.

[36] S. Siebentritt, Why are kesterite solar cells not 20% efficient?, Thin Solid Films, 535 (2013) 1-4.

[37] M. Nakashima, J. Fujimoto, T. Yamaguchi, M. Izaki, Cu_2SnS_3 thin-film solar cells fabricated by sulfurization from NaF/Cu/Sn stacked precursor, Applied Physics Express, 8 (2015) 042303.

[38] Q. Chen, X. Dou, Y. Ni, S. Cheng, S. Zhuang, Study and enhance the photovoltaic properties of narrow-bandgap Cu_2SnS_3 solar cell by p-n junction interface modification, Journal of colloid and interface science, 376 (2012) 327-330.

[39] N. Aihara, A. Kanai, K. Kimura, M. Yamada, K. Toyonaga, H. Araki, A. Takeuchi, H. Katagiri, Sulfurization temperature dependences of photovoltaic properties in Cu_2SnS_3-based thin-film solar cells, Japanese Journal of Applied Physics, 53 (2014) 05FW13.

[40] K. Ayaka, T. Kotoba, C. Kotaro, K. Hironori, A. Hideaki, Fabrication of Cu_2SnS_3 thin-film solar cells with power conversion efficiency of over 4%, Japanese Journal of Applied Physics, 54 (2015) 08KC06.

[41] T. Nomura, T. Maeda, T. Wada, Fabrication of Cu_2SnS_3 solar cells by screen-printing and high-pressure sintering process, Japanese Journal of Applied Physics, 53 (2014) 05FW01.

[42] A. Kanai, H. Araki, A. Takeuchi, H. Katagiri, Annealing temperature dependence of photovoltaic properties of solar cells containing Cu_2SnS_3 thin films produced by co-evaporation, physica status solidi (b), 252 (2015) 1239-1243.

[43] N. Aihara, H. Araki, A. Takeuchi, K. Jimbo, H. Katagiri, Fabrication of Cu_2SnS_3 thin films by sulfurization of evaporated Cu-Sn precursors for solar cells, physica status solidi (c), 10 (2013) 1086-1092.

[44] M. Nakashima, T. Yamaguchi, H. Itani, J. Sasano, M. Izaki, Cu_2SnS_3 thin film solar cells prepared by thermal crystallization of evaporated Cu/Sn precursors in sulfur and tin atmosphere, physica status solidi (c), 12 (2015) 761-764.

[45] J. Li, C. Xue, Y. Wang, G. Jiang, W. Liu, C. Zhu, Cu_2SnS_3 solar cells fabricated by chemical bath deposition–annealing of SnS/Cu stacked layers, Solar Energy Materials and Solar Cells, 144 (2016) 281-288.

[46] S.A. Vanalakar, G.L. Agawane, A.S. Kamble, C.W. Hong, P.S. Patil, J.H. Kim, Fabrication of Cu_2SnS_3 thin film solar cells using pulsed laser deposition technique, Solar Energy Materials and Solar Cells, 138 (2015) 1-8.

[47] D.M. Berg, R. Djemour, L. Gütay, G. Zoppi, S. Siebentritt, P.J. Dale, Thin film solar cells based on the ternary compound Cu_2SnS_3, Thin Solid Films, 520 (2012) 6291-6294.

[48] T.A. Kuku, O.A. Fakolujo, Photovoltaic characteristics of thin films of Cu_2SnS_3, Solar energy materials, 16 (1987) 199-204.

[49] J. Koike, K. Chino, N. Aihara, H. Araki, R. Nakamura, K. Jimbo, H. Katagiri, Cu_2SnS_3 Thin-Film Solar Cells from Electroplated Precursors, Japanese Journal of Applied Physics, 51 (2012) 10NC34.

[50] M. Umehara, Y. Takeda, T. Motohiro, T. Sakai, H. Awano, R. Maekawa, $Cu_2Sn_{1-x}Ge_xS_3$ (x= 0.17) thin-film solar cells with high conversion efficiency of 6.0%, Applied Physics Express, 6 (2013) 045501.

[51] P. Zawadzki, L.L. Baranowski, H. Peng, E.S. Toberer, D.S. Ginley, W. Tumas, A. Zakutayev, S. Lany, Evaluation of photovoltaic materials within the Cu-Sn-S family, Applied Physics Letters, 103 (2013) 253902.

[52] P. Fernandes, P. Salomé, A. Da Cunha, CuxSnSx+ 1 (x= 2, 3) thin films grown by sulfurization of metallic precursors deposited by dc magnetron sputtering, physica status solidi (c), 7 (2010) 901-904.

[53] G. Marcano, C. Rincón, L.M. de Chalbaud, D.B. Bracho, G.S.n. Pérez, Crystal growth and structure, electrical, and optical characterization of the semiconductor Cu_2SnSe_3, Journal of Applied Physics, 90 (2001) 1847.

[54] S.G. Choi, J. Kang, J. Li, H. Haneef, N.J. Podraza, C. Beall, S.H. Wei, S.T. Christensen, I.L. Repins, Optical function spectra and bandgap energy of Cu_2SnSe_3, Applied Physics Letters, 106 (2015) 043902.

[55] S. Schorr, The crystal structure of kesterite type compounds: A neutron and X-ray diffraction study, Solar Energy Materials and Solar Cells, 95 (2011) 1482-1488.

[56] S. Hall, J. Szymanski, J. Stewart, Kesterite, $Cu_2(Zn,Fe)SnS_4$, and stannite, $Cu_2(Fe,Zn)SnS_4$, structurally similar but distinct minerals, The Canadian Mineralogist, 16 (1978) 131-137.

[57] J. Paier, R. Asahi, A. Nagoya, G. Kresse, Cu_2ZnSnS_4 as a potential photovoltaic material: a hybrid Hartree-Fock density functional theory study, Physical Review B, 79 (2009) 115126.

[58] J.J.S. Scragg, L. Choubrac, A. Lafond, T. Ericson, C. Platzer-Björkman, A low-temperature order-disorder transition in Cu_2ZnSnS_4 thin films, Applied Physics Letters, 104 (2014) 041911.

[59] J.J.S. Scragg, J.K. Larsen, M. Kumar, C. Persson, J. Sendler, S. Siebentritt, C. Platzer Björkman, Cu-Zn disorder and band gap fluctuations in $Cu_2ZnSn(S,Se)_4$:

Theoretical and experimental investigations (Phys. Status Solidi B 2/2016), physica status solidi (b), 253 (2016) 189-189.

[60] G. Rey, A. Redinger, J. Sendler, T.P. Weiss, M. Thevenin, M. Guennou, B. El Adib, S. Siebentritt, The band gap of $Cu_2ZnSnSe_4$: Effect of order-disorder, Applied Physics Letters, 105 (2014) 112106.

[61] C. Krämmer, C. Huber, C. Zimmermann, M. Lang, T. Schnabel, T. Abzieher, E. Ahlswede, H. Kalt, M. Hetterich, Reversible order-disorder related band gap changes in $Cu_2ZnSn(S,Se)_4$ via post-annealing of solar cells measured by electroreflectance, Applied Physics Letters, 105 (2014) 262104.

[62] I.V. Dudchak, L.V. Piskach, Phase equilibria in the Cu_2SnSe_3–$SnSe_2$–ZnSe system, Journal of Alloys and Compounds, 351 (2002) 145-150.

[63] S. Temgoua, R. Bodeux, N. Naghavi, S. Delbos, Effects of $SnSe_2$ secondary phases on the efficiency of $Cu_2ZnSn(S_x,Se_{1-x})_4$ based solar cells, Thin Solid Films, 582 (2015) 215-219.

[64] S. Lopez-Marino, Y. Sanchez, M. Placidi, A. Fairbrother, M. Espindola-Rodriguez, X. Fontane, V. Izquierdo-Roca, J. Lopez-Garcia, L. Calvo-Barrio, A. Perez-Rodriguez, E. Saucedo, ZnSe etching of Zn-rich $Cu_2ZnSnSe_4$: an oxidation route for improved solar-cell efficiency, Chemistry, 19 (2013) 14814-14822.

[65] H. Xie, Y. Sanchez, S. Lopez-Marino, M. Espindola-Rodriguez, M. Neuschitzer, D. Sylla, A. Fairbrother, V. Izquierdo-Roca, A. Perez-Rodriguez, E. Saucedo, Impact of Sn(S,Se) secondary phases in $Cu_2ZnSn(S,Se)_4$ solar cells: a chemical route for their selective removal and absorber surface passivation, ACS applied materials & interfaces, 6 (2014) 12744-12751.

[66] S. Chen, L.-W. Wang, A. Walsh, X.G. Gong, S.-H. Wei, Abundance of $Cu_{Zn} + Sn_{Zn}$ and $2Cu_{Zn} + Sn_{Zn}$ defect clusters in kesterite solar cells, Applied Physics Letters, 101 (2012) 223901.

[67] L.E. Valle Rios, K. Neldner, G. Gurieva, S. Schorr, Existence of off-stoichiometric single phase kesterite, Journal of Alloys and Compounds, 657 (2016) 408-413.

[68] A. Lafond, L. Choubrac, C. Guillot-Deudon, P. Deniard, S. Jobic, Crystal Structures of Photovoltaic Chalcogenides, an Intricate Puzzle to Solve: the Cases of CIGSe and CZTS Materials, Zeitschrift Fur Anorganische Und Allgemeine Chemie, 638 (2012) 2571-2577.

[69] I. Repins, C. Beall, N. Vora, C. DeHart, D. Kuciauskas, P. Dippo, B. To, J. Mann, W.-C. Hsu, A. Goodrich, R. Noufi, Co-evaporated $Cu_2ZnSnSe_4$ films and devices, Solar Energy Materials and Solar Cells, 101 (2012) 154-159.

[70] M. Hála, S. Fujii, A. Redinger, Y. Inoue, G. Rey, M. Thevenin, V. Deprédurand, T.P. Weiss, T. Bertram, S. Siebentritt, Highly conductive ZnO films with high near infrared transparency, Progress in Photovoltaics: Research and Applications, 23 (2015) 1630-1641.

[71] M. Neuschitzer, Y. Sanchez, S. López-Marino, H. Xie, A. Fairbrother, M. Placidi, S. Haass, V. Izquierdo-Roca, A. Perez-Rodriguez, E. Saucedo, Optimization of CdS buffer layer for high-performance $Cu_2ZnSnSe_4$ solar cells and the effects of light soaking: elimination of crossover and red kink, Progress in Photovoltaics: Research and Applications, 23 (2015) 1660-1667.

[72] G. Zoppi, I. Forbes, R.W. Miles, P.J. Dale, J.J. Scragg, L.M. Peter, $Cu_2ZnSnSe_4$ thin film solar cells produced by selenisation of magnetron sputtered precursors, Progress in Photovoltaics: Research and Applications, 17 (2009) 315-319.

[73] J.J. Scragg, T. Kubart, J.T. Wätjen, T. Ericson, M.K. Linnarsson, C. Platzer-Björkman, Effects of Back Contact Instability on Cu_2ZnSnS_4 Devices and Processes, Chemistry of Materials, 25 (2013) 3162-3171.

[74] L. Vauche, L. Risch, Y. Sánchez, M. Dimitrievska, M. Pasquinelli, T. Goislard de Monsabert, P.-P. Grand, S. Jaime-Ferrer, E. Saucedo, 8.2% pure selenide kesterite thin-film solar cells from large-area electrodeposited precursors, Progress in Photovoltaics: Research and Applications, 24 (2016) 38-51.

[75] S.G. Haass, M. Diethelm, M. Werner, B. Bissig, Y.E. Romanyuk, A.N. Tiwari, 11.2% Efficient Solution Processed Kesterite Solar Cell with a Low Voltage Deficit, Advanced Energy Materials, 5 (2015) 1500712.

[76] H. Xin, S. Vorpahl, A. Collord, I. Braly, A. Uhl, B. Krueger, D. Ginger, H. Hillhouse, Lithium-doping inverts the nanoscale electric field at the grain boundaries in $Cu_2ZnSn(S,Se)_4$ and increases photovoltaic efficiency, Physical Chemistry Chemical Physics, 17 (2015) 23859-23866.

[77] T. Schnabel, T. Abzieher, T.M. Friedlmeier, E. Ahlswede, Solution-Based Preparation of $Cu_2ZnSn(S,Se)_4$ for Solar Cells—Comparison of $SnSe_2$ and Elemental Se as Chalcogen Source, Photovoltaics, IEEE Journal of, 5 (2015) 670-675.

[78] G. Larramona, S. Levcenko, S. Bourdais, A. Jacob, C. Choné, B. Delatouche, C. Moisan, J. Just, T. Unold, G. Dennler, Fine-Tuning the Sn Content in CZTSSe Thin Films to Achieve 10.8% Solar Cell Efficiency from Spray-Deposited Water-Ethanol-Based Colloidal Inks, Advanced Energy Materials, 5 (2015) 1501404.

[79] G. Rey, T. Weiss, J. Sendler, A. Finger, C. Spindler, F. Werner, M. Melchiorre, M. Hála, M. Guennou, S. Siebentritt, Ordering kesterite improves solar cells: A low temperature post-deposition annealing study, Solar Energy Materials and Solar Cells, 151 (2016) 131-138.

[80] G. Brammertz, Y. Ren, M. Buffière, S. Mertens, J. Hendrickx, H. Marko, A.E. Zaghi, N. Lenaers, C. Köble, J. Vleugels, M. Meuris, J. Poortmans, Electrical characterization of $Cu_2ZnSnSe_4$ solar cells from selenization of sputtered metal layers, Thin Solid Films, 535 (2013) 348-352.

[81] S. Oueslati, G. Brammertz, M. Buffière, H. ElAnzeery, O. Touayar, C. Köble, J. Bekaert, M. Meuris, J. Poortmans, Physical and electrical characterization of high-performance $Cu_2ZnSnSe_4$ based thin film solar cells, Thin Solid Films, 582 (2015) 224-228.

[82] G. Brammertz, M. Buffière, S. Oueslati, H. ElAnzeery, K. Ben Messaoud, S. Sahayaraj, C. Köble, M. Meuris, J. Poortmans, Characterization of defects in 9.7 % efficient $Cu_2ZnSnSe_4$-CdS-ZnO solar cells, Applied Physics Letters, 103 (2013) 163904.

[83] M. Kumar, A. Dubey, N. Adhikari, S. Venkatesan, Q. Qiao, Strategic review of secondary phases, defects and defect-complexes in kesterite CZTS–Se solar cells, Energy & Environmental Science, 8 (2015) 3134-3159.

[84] L. Vauche, Process development and scale-up for low-cost high-efficiency kesterite thin film photovoltaics, PhD Diss, in Université d'Aix Marseille, 2015.

[85] I.L. Repins, J.V. Li, A. Kanevce, C.L. Perkins, K.X. Steirer, J. Pankow, G. Teeter, D. Kuciauskas, C. Beall, C. Dehart, J. Carapella, B. Bob, J.S. Park, S.H. Wei, Effects of deposition termination on $Cu_2ZnSnSe_4$ device characteristics, Thin Solid Films, 582 (2015) 184-187.

[86] J. Li, Y. Zhang, W. Zhao, D. Nam, H. Cheong, L. Wu, Z. Zhou, Y. Sun, A Temporary Barrier Effect of the Alloy Layer During Selenization: Tailoring the Thickness of $MoSe_2$ for Efficient $Cu_2ZnSnSe_4$ Solar Cells, Advanced Energy Materials, 5 (2015) 1402178.

[87] M. Neuschitzer, Y. Sanchez, T. Olar, T. Thersleff, S. Lopez-Marino, F. Oliva, M. Espindola-Rodriguez, H. Xie, M. Placidi, V. Izquierdo-Roca, I. Lauermann, K. Leifer, A. Pérez-Rodriguez, E. Saucedo, Complex Surface Chemistry of Kesterites: Cu/Zn Reordering after Low Temperature Postdeposition Annealing and Its Role in High Performance Devices, Chemistry of Materials, 27 (2015) 5279-5287.

[88] R. Bodeux, F. Mollica, S. Delbos, Growth of $Cu_2ZnSnSe_4$ by cosputtering and reactive annealing atmosphere, Solar Energy Materials and Solar Cells, 132 (2015) 67-73.

[89] J.O. Jeon, K.D. Lee, L. Seul Oh, S.W. Seo, D.K. Lee, H. Kim, J.H. Jeong, M.J. Ko, B. Kim, H.J. Son, J.Y. Kim, Highly efficient copper-zinc-tin-selenide (CZTSe) solar cells by electrodeposition, ChemSusChem, 7 (2014) 1073-1077.

[90] J. Márquez, M. Neuschitzer, M. Dimitrievska, R. Gunder, S. Haass, M. Werner, Y.E. Romanyuk, S. Schorr, N.M. Pearsall, I. Forbes, Systematic compositional changes and their influence on lattice and optoelectronic properties of $Cu_2ZnSnSe_4$ kesterite solar cells, Solar Energy Materials and Solar Cells, 144 (2016) 579-585.

[91] J.J. Scragg, J.T. Watjen, M. Edoff, T. Ericson, T. Kubart, C. Platzer-Bjorkman, A detrimental reaction at the molybdenum back contact in Cu2ZnSn(S,Se)4 thin-film solar cells, Journal of the American Chemical Society, 134 (2012) 19330-19333.

[92] T. Ericson, J.J. Scragg, A. Hultqvist, J.T. Watjen, P. Szaniawski, T. Torndahl, C. Platzer-Bjorkman, Zn(O,S) Buffer Layers and Thickness Variations of CdS Buffer for Cu_2ZnSnS_4 Solar Cells, IEEE Journal of Photovoltaics, 4 (2014) 465-469.

[93] S.M. Sze, K.K. Ng, Physics of semiconductor devices, John wiley & sons, 2006.

[94] J. Nelson, The physics of solar cells. London: Imperial College Press, 2003.

[95] P. Würfel, U. Würfel, Physics of solar cells: from basic principles to advanced concepts, John Wiley & Sons, 2009.

[96] F.H. Pianezzi, Electronic transport and doping mechanisms in Cu(In,Ga)Se_2 thin film solar cells, in, PhD Diss., Eidgenössische Technische Hochschule ETH Zürich, Nr. 21812, 2014.

[97] F. Smits, Measurement of sheet resistivities with the four-point probe, Bell System Technical Journal, 37 (1958) 711-718.

[98] J. Lindahl, U. Zimmermann, P. Szaniawski, T. Torndahl, A. Hultqvist, P. Salomé, C. Platzer-Bjorkman, M. Edoff, Inline Cu(In,Ga)Se_2 Co-evaporation for High-Efficiency Solar Cells and Modules, Photovoltaics, IEEE Journal of, 3 (2013) 1100-1105.

[99] A. Chirilă, S. Buecheler, F. Pianezzi, P. Bloesch, C. Gretener, A.R. Uhl, C. Fella, L. Kranz, J. Perrenoud, S. Seyrling, R. Verma, S. Nishiwaki, Y.E. Romanyuk,

G. Bilger, A.N. Tiwari, Highly efficient Cu(In,Ga)Se_2 solar cells grown on flexible polymer films, Nat Mater, 10 (2011) 857-861.

[100] A. Weber, H. Krauth, S. Perlt, B. Schubert, I. Kötschau, S. Schorr, H.W. Schock, Multi-stage evaporation of Cu_2ZnSnS_4 thin films, Thin Solid Films, 517 (2009) 2524-2526.

[101] M. Mousel, T. Schwarz, R. Djemour, T.P. Weiss, J. Sendler, J.C. Malaquias, A. Redinger, O. Cojocaru-Mirédin, P.-P. Choi, S. Siebentritt, Cu-Rich Precursors Improve Kesterite Solar Cells, Advanced Energy Materials, 4 (2014) 1300543.

[102] T. Unold, J. Just, H.W. Schock, Coevaporation of CZTS Films and Solar Cells, Copper Zinc Tin Sulfide-Based Thin Film Solar Cells, (2014) 221.

[103] M. Birkholz, Thin film analysis by X-ray scattering, John Wiley & Sons, 2006.

[104] W.H. Bragg, W.L. Bragg, The reflection of X-rays by crystals, Proceedings of the Royal Society of London. Series A, Containing Papers of a Mathematical and Physical Character, 88 (1913) 428-438.

[105] R. Gunder, Microstructural Analysis of $Cu_2ZnSnSe_4$ Thin Films, Master's Thesis, in Freie Universität Berlin, 2014.

[106] A. Le Bail, H. Duroy, J. Fourquet, Ab-initio structure determination of LiSbWO 6 by X-ray powder diffraction, Materials Research Bulletin, 23 (1988) 447-452.

[107] B.H. Toby, R factors in Rietveld analysis: How good is good enough?, Powder Diffraction, 21 (2012) 67-70.

[108] J. Rodriguez-Carvajal, FULLPROF: a program for Rietveld refinement and pattern matching analysis, in: satellite meeting on powder diffraction of the XV congress of the IUCr, Toulouse, France, 1990.

[109] Inorganic Crystal Structure Database (ICSD) http://icsd.cds.rsc.org/ [Accessed 21 Apr. 2016].

[110] P. Scherrer, Estimation of the size and internal structure of colloidal particles by means of röntgen, Nachr. Ges. Wiss. Göttingen, 2 (1918) 96-100.

[111] G. Williamson, W. Hall, X-ray line broadening from filed aluminium and wolfram, Acta metallurgica, 1 (1953) 22-31.

[112] J. Álvarez-García, V. Izquierdo-Roca, A. Pérez-Rodríguez, Raman spectroscopy on thin films for solar cells, Advanced Characterization Techniques for Thin Film Solar Cells, (2011) 365-386.

[113] A. Fairbrother, X. Fontané, V. Izquierdo-Roca, M. Placidi, D. Sylla, M. Espindola-Rodriguez, S. López-Mariño, F.A. Pulgarín, O. Vigil-Galán, A. Pérez-Rodríguez, E. Saucedo, Secondary phase formation in Zn-rich $Cu_2ZnSnSe_4$-based solar cells annealed in low pressure and temperature conditions, Progress in Photovoltaics: Research and Applications, 22 (2014) 479-487.

[114] M. Dimitrievska, A. Fairbrother, X. Fontané, T. Jawhari, V. Izquierdo-Roca, E. Saucedo, A. Pérez-Rodríguez, Multiwavelength excitation Raman scattering study of polycrystalline kesterite Cu_2ZnSnS_4 thin films, Applied Physics Letters, 104 (2014) 021901.

[115] M. Dimitrievska, G. Gurieva, H. Xie, A. Carrete, A. Cabot, E. Saucedo, A. Pérez-Rodríguez, S. Schorr, V. Izquierdo-Roca, Raman scattering quantitative analysis of the anion chemical composition in kesterite $Cu_2ZnSn(S_xSe_{1-x})_4$ solid solutions, Journal of Alloys and Compounds, 628 (2015) 464-470.

[116] M. Dimitrievska, A. Fairbrother, E. Saucedo, A. Pérez-Rodríguez, V. Izquierdo-Roca, Influence of compositionally induced defects on the vibrational properties of device grade $Cu_2ZnSnSe_4$ absorbers for kesterite based solar cells, Applied Physics Letters, 106 (2015) 073903.

[117] J. Márquez-Prieto, Y. Ren, R.W. Miles, N. Pearsall, I. Forbes, The influence of precursor Cu content and two-stage processing conditions on the microstructure of $Cu_2ZnSnSe_4$, Thin Solid Films, 582 (2015) 220-223.

[118] D. Myers, S. Kurtz, K. Emery, C. Whitaker, T. Townsend, Outdoor meteorological broadband and spectral conditions for evaluating photovoltaic modules, in: Photovoltaic Specialists Conference, 2000. Conference Record of the Twenty-Eighth IEEE, (2000) 1202-1205.

[119] C.J. Hages, N.J. Carter, R. Agrawal, Generalized quantum efficiency analysis for non-ideal solar cells: Case of $Cu_2ZnSnSe_4$, Journal of Applied Physics, 119 (2016) 014505.

[120] S.S. Hegedus, W.N. Shafarman, Thin-film solar cells: device measurements and analysis, Progress in Photovoltaics: Research and Applications, 12 (2004) 155-176.

[121] T. Gokmen, O. Gunawan, T.K. Todorov, D.B. Mitzi, Band tailing and efficiency limitation in kesterite solar cells, Applied Physics Letters, 103 (2013) 103506.

[122] J. Heath, P. Zabierowski, Capacitance Spectroscopy of Thin-Film Solar Cells, Advanced Characterization Techniques for Thin Film Solar Cells, (2011) 81-105.

[123] T. Unold, L. Gütay, Photoluminescence Analysis of Thin-Film Solar Cells, in: Advanced Characterization Techniques for Thin Film Solar Cells, Wiley-VCH Verlag GmbH & Co. KGaA, 2011, pp. 151-175.

[124] I.D. Olekseyuk, I.V. Dudchak, L.V. Piskach, Phase equilibria in the Cu_2S–ZnS–SnS_2 system, Journal of Alloys and Compounds, 368 (2004) 135-143.

[125] A. Redinger, D.M. Berg, P.J. Dale, R. Djemour, L. Gütay, T. Eisenbarth, N. Valle, S. Siebentritt, Route Toward High-Efficiency Single-Phase $Cu_2ZnSn(S,Se)_4$ Thin-Film Solar Cells: Model Experiments and Literature Review, IEEE Journal of Photovoltaics, 1 (2011) 200-206.

[126] R.A. Wibowo, S.A. Moeckel, H. Yoo, C. Hetzner, A. Hoelzing, P. Wellmann, R. Hock, Intermetallic compounds dynamic formation during annealing of stacked elemental layers and its influences on the crystallization of $Cu_2ZnSnSe_4$ films, Materials Chemistry and Physics, 142 (2013) 311-317.

[127] R. Caballero, C. Guillén, M. Gutiérrez, C. Kaufmann, $CuIn_{1-x}Ga_xSe_2$-based thin-film solar cells by the selenization of sequentially evaporated metallic layers, Progress in Photovoltaics: Research and Applications, 14 (2006) 145-153.

[128] J. Timo Wätjen, J. Engman, M. Edoff, C. Platzer-Björkman, Direct evidence of current blocking by ZnSe in $Cu_2ZnSnSe_4$ solar cells, Applied Physics Letters, 100 (2012) 173510.

[129] W.-C. Hsu, I. Repins, C. Beall, C. DeHart, G. Teeter, B. To, Y. Yang, R. Noufi, The effect of Zn excess on kesterite solar cells, Solar Energy Materials and Solar Cells, 113 (2013) 160-164.

[130] D. Colombara, E.V.C. Robert, A. Crossay, A. Taylor, M. Guennou, M. Arasimowicz, J.C.B. Malaquias, R. Djemour, P.J. Dale, Quantification of surface

ZnSe in $Cu_2ZnSnSe_4$-based solar cells by analysis of the spectral response, Solar Energy Materials and Solar Cells, 123 (2014) 220-227.

[131] G.E. Delgado, A.J. Mora, G. Marcano, C. Rincón, Crystal structure refinement of the semiconducting compound Cu_2SnSe_3 from X-ray powder diffraction data, Materials Research Bulletin, 38 (2003) 1949-1955.

[132] L.D. Gulay, M. Daszkiewicz, T.A. Ostapyuk, O.S. Klymovych, O.F. Zmiy, Monoclinic Cu_2Se_3Sn, Acta crystallographica. Section C, Crystal structure communications, 66 (2010) i58-60.

[133] J. Fan, W. Carrillo-Cabrera, L. Akselrud, I. Antonyshyn, L. Chen, Y. Grin, New monoclinic phase at the composition Cu_2SnSe_3 and its thermoelectric properties, Inorganic chemistry, 52 (2013) 11067-11074.

[134] G. Marcano, C. Rincon, S.A. Lopez, G.S. Perez, J.L. Herrera-Perez, J.G. Mendoza-Alvarez, P. Rodriguez, Raman spectrum of monoclinic semiconductor Cu_2SnSe_3, Solid State Communications, 151 (2011) 84-86.

[135] M. Altosaar, J. Raudoja, K. Timmo, M. Danilson, M. Grossberg, J. Krustok, E. Mellikov, $Cu_2Zn_{1-x}Cd_xSn(Se_{1-y}S_y)_4$ solid solutions as absorber materials for solar cells, physica status solidi (a), 205 (2008) 167-170.

[136] N. Beigom Mortazavi Amiri, A. Postnikov, Secondary phase Cu2SnSe3 vs. kesterite $Cu_2ZnSnSe_4$: Similarities and differences in lattice vibration modes, Journal of Applied Physics, 112 (2012) 033719.

[137] M. Wojdyr, Fityk: a general-purpose peak fitting program, Journal of Applied Crystallography, 43 (2010) 1126-1128.

[138] P. Uday Bhaskar, G. Suresh Babu, Y.B. Kishore Kumar, V. Sundara Raja, Investigations on co-evaporated Cu_2SnSe_3 and Cu_2SnSe_3–ZnSe thin films, Applied Surface Science, 257 (2011) 8529-8534.

[139] M. Umehara, Y. Takeda, T. Motohiro, T. Sakai, H. Awano, R. Maekawa, $Cu_2Sn_{1-x}Ge_xS_3$(x= 0.17) Thin-Film Solar Cells with High Conversion Efficiency of 6.0%, Applied Physics Express, 6 (2013) 045501.

[140] K.M. Kim, H. Tampo, H. Shibata, S. Niki, Growth and characterization of coevaporated Cu_2SnSe_3 thin films for photovoltaic applications, Thin Solid Films, 536 (2013) 111-114.

[141] Y.-T. Zhai, S. Chen, J.-H. Yang, H.-J. Xiang, X.-G. Gong, A. Walsh, J. Kang, S.-H. Wei, Structural diversity and electronic properties of Cu_2SnX_3(X=S, Se): A first-principles investigation, Physical Review B, 84 (2011).

[142] K.M. Kim, H. Tampo, H. Shibata, S. Niki, Temperature induced phase transformation in coevaporated Cu_2SnSe_3 thin films, Materials Letters, 116 (2014) 61-63.

[143] X. Shi, L. Xi, J. Fan, W. Zhang, L. Chen, Cu−Se Bond Network and Thermoelectric Compounds with Complex Diamondlike Structure, Chemistry of Materials, 22 (2010) 6029-6031.

[144] S. Schorr, A. Weber, V. Honkimäki, H.-W. Schock, In-situ investigation of the kesterite formation from binary and ternary sulphides, Thin Solid Films, 517 (2009) 2461-2464.

[145] K.J. Hutchings, High throughput combinatorial screening of Cu-Zn-Sn-S thin film libraries for the application of Cu_2ZnSnS_4 photovoltaic cells, PhD Thesis, in Cranfield Univeristy, 2014.

[146] J.R. Tuttle, M. Contreras, M.H. Bode, D. Niles, D.S. Albin, R. Matson, A.M. Gabor, A. Tennant, A. Duda, R. Noufi, Structure, chemistry, and growth mechanisms of photovoltaic quality thin-film Cu(In,Ga)Se_2 grown from a mixed-phase precursor, Journal of Applied Physics, 77 (1995) 153.

[147] W.-C. Hsu, I. Repins, C. Beall, C. DeHart, B. To, W. Yang, Y. Yang, R. Noufi, Growth mechanisms of co-evaporated kesterite: a comparison of Cu-rich and Zn-rich composition paths, Progress in Photovoltaics: Research and Applications, 22 (2014) 35-43.

[148] H. Stange, S. Brunken, H. Hempel, H. Rodriguez-Alvarez, N. Schäfer, D. Greiner, A. Scheu, J. Lauche, C.A. Kaufmann, T. Unold, D. Abou-Ras, R. Mainz, Effect of Na presence during $CuInSe_2$ growth on stacking fault annihilation and electronic properties, Applied Physics Letters, 107 (2015) 152103.

[149] R. Djemour, A. Redinger, M. Mousel, L. Gutay, X. Fontane, V. Izquierdo-Roca, A. Perez-Rodriguez, S. Siebentritt, The three A symmetry Raman modes of kesterite in $Cu_2ZnSnSe_4$, Optics express, 21 Suppl 4 (2013) A695-703.

[150] J.J. Scragg, P.J. Dale, D. Colombara, L.M. Peter, Thermodynamic aspects of the synthesis of thin-film materials for solar cells, Chemphyschem : a European journal of chemical physics and physical chemistry, 13 (2012) 3035-3046.

[151] B. Shin, Y. Zhu, N.A. Bojarczuk, S. Jay Chey, S. Guha, Control of an interfacial $MoSe_2$ layer in $Cu_2ZnSnSe_4$ thin film solar cells: 8.9% power conversion efficiency with a TiN diffusion barrier, Applied Physics Letters, 101 (2012) 053903.

[152] M. Arasimowicz, Phase segregation in $Cu_2ZnSnSe_4$ thin films for photovoltaic applications, PhD Thesis, in Université du Luxembourg, 2014.

[153] A.J. Jackson, A. Walsh, Abinitio thermodynamic model of Cu_2ZnSnS_4, J. Mater. Chem. A, 2 (2014) 7829-7836.

[154] S. López-Marino, M. Placidi, A. Pérez-Tomás, J. Llobet, V. Izquierdo-Roca, X. Fontané, A. Fairbrother, M. Espíndola-Rodríguez, D. Sylla, A. Pérez-Rodríguez, E. Saucedo, Inhibiting the absorber/Mo-back contact decomposition reaction in $Cu_2ZnSnSe_4$ solar cells: the role of a ZnO intermediate nanolayer, Journal of Materials Chemistry A, 1 (2013) 8338.

[155] M. Grossberg, J. Krustok, T. Raadik, M. Kauk-Kuusik, J. Raudoja, Photoluminescence study of disordering in the cation sublattice of Cu_2ZnSnS_4, Current Applied Physics, 14 (2014) 1424-1427.

[156] M. Paris, L. Choubrac, A. Lafond, C. Guillot-Deudon, S. Jobic, Solid-state NMR and Raman spectroscopy to address the local structure of defects and the tricky issue of the Cu/Zn disorder in Cu-poor, Zn-rich CZTS materials, Inorganic chemistry, 53 (2014) 8646-8653.

[157] J. Márquez-Prieto, I. Forbes, Evolution of phases in two-stage vacuum processed thin film $Cu_2ZnSnSe_4$ absorber layers, Materials Research Innovations, 18 (2014) 515-518.

[158] N.B. Mortazavi Amiri, A. Postnikov, Electronic structure and lattice dynamics in kesterite-type $Cu_2ZnSnSe_2$ from first-principles calculations, Physical Review B, 82 (2010) 205204.

[159] J.M. Skelton, A.J. Jackson, M. Dimitrievska, S.K. Wallace, A. Walsh, Vibrational spectra and lattice thermal conductivity of kesterite-structured Cu_2ZnSnS_4 and $Cu_2ZnSnSe_4$, APL Materials, 3 (2015) 041102.

[160] R. Caballero, E. Garcia-Llamas, J.M. Merino, M. León, I. Babichuk, V. Dzhagan, V. Strelchuk, M. Valakh, Non-stoichiometry effect and disorder in Cu_2ZnSnS_4 thin films obtained by flash evaporation: Raman scattering investigation, Acta Materialia, 65 (2014) 412-417.

[161] M. Dimitrievska, H. Xie, A. Jackson, X. Fontané, M. Espíndola-Rodríguez, E. Saucedo, A. Pérez-Rodríguez, A. Walsh, V. Izquierdo-Roca, Resonant Raman scattering of ZnS_xSe_{1-x} solid solutions: the role of S and Se electronic states, Physical Chemistry Chemical Physics, (2016).

[162] A.D. Collord, H. Xin, H.W. Hillhouse, Combinatorial Exploration of the Effects of Intrinsic and Extrinsic Defects in $Cu_2ZnSn(S,Se)_4$, IEEE Journal of Photovoltaics, 5 (2015) 288-298.

[163] S. Chen, X.G. Gong, A. Walsh, S.-H. Wei, Crystal and electronic band structure of Cu_2ZnSnX_4 (X=S and Se) photovoltaic absorbers: First-principles insights, Applied Physics Letters, 94 (2009) 041903.

[164] C. Persson, Electronic and optical properties of Cu_2ZnSnS_4 and $Cu_2ZnSnSe_4$, Journal of Applied Physics, 107 (2010) 3710.

[165] S. Botti, D. Kammerlander, M.A.L. Marques, Band structures of Cu_2ZnSnS_4 and $Cu_2ZnSnSe_4$ from many-body methods, Applied Physics Letters, 98 (2011) 241915.

[166] H.B. Bebb, E. Williams, Semiconductors and Semimetals, Academic Press, New York, 8 (1972) 181.

[167] M. Dimitrievska, A. Fairbrother, V. Izquierdo-Roca, A. Pérez-Rodríguez, E. Saucedo, Two ideal compositions for kesterite-based solar cell devices, in: Photovoltaic Specialist Conference (PVSC), 2014 IEEE 40th, IEEE, 2014, pp. 2307-2309.

[168] M. Grossberg, J. Krustok, K. Timmo, M. Altosaar, Radiative recombination in $Cu_2ZnSnSe_4$ monograins studied by photoluminescence spectroscopy, Thin Solid Films, 517 (2009) 2489-2492.

[169] S. Oueslati, G. Brammertz, M. Buffière, C. Köble, T. Oualid, M. Meuris, J. Poortmans, Photoluminescence study and observation of unusual optical transitions in $Cu_2ZnSnSe_4$/CdS/ZnO solar cells, Solar Energy Materials and Solar Cells, 134 (2015) 340-345.

[170] A. Redinger, K. Hones, X. Fontane, V. Izquierdo-Roca, E. Saucedo, N. Valle, A. Perez-Rodriguez, S. Siebentritt, Detection of a ZnSe secondary phase in coevaporated $Cu_2ZnSnSe_4$ thin films, Applied Physics Letters, 98 (2011) 101907.

[171] L.Q. Phuong, M. Okano, Y. Yamada, G. Yamashita, T. Morimoto, M. Nagai, M. Ashida, A. Nagaoka, K. Yoshino, Y. Kanemitsu, Ultrafast free-carrier dynamics in Cu_2ZnSnS_4 single crystals studied using femtosecond time-resolved optical spectroscopy, Applied Physics Letters, 105 (2014) 231902.

[172] A.J. Smith, P.E. Meek, W.Y. Liang, Raman scattering studies of SnS_2 and $SnSe_2$, Journal of Physics C: Solid State Physics, 10 (1977) 1321.

[173] M. Dimitrievska, A. Fairbrother, A. Pérez-Rodríguez, E. Saucedo, V. Izquierdo-Roca, Raman scattering crystalline assessment of polycrystalline Cu_2ZnSnS_4 thin

films for sustainable photovoltaic technologies: Phonon confinement model, Acta Materialia, 70 (2014) 272-280.

[174] J. Márquez-Prieto, M.V. Yakushev, I. Forbes, J. Krustok, P.R. Edwards, V.D. Zhivulko, O.M. Borodavchenko, A.V. Mudryi, M. Dimitrievska, V. Izquerdo-Roca, N.M. Pearsall, R.W. Martin, Impact of the selenisation temperature on the structural and optical properties of CZTSe absorbers, Solar Energy Materials and Solar Cells, 152 (2016) 42-50.

[175] A.P. Levanyuk, V.V. Osipov, Edge luminescence of direct-gap semiconductors, Uspekhi Fizicheskih Nauk, 133 (1981) 427.

[176] J. Krustok, H. Collan, M. Yakushev, K. Hjelt, The Role of Spatial Potential Fluctuations in the Shape of the PL Bands of Multinary Semiconductor Compounds, Physica Scripta, T79 (1999) 179.

[177] B. Shklovskii, A. Efros, Electronic Properties of Doped Semiconductors. 1984, Springer, Berlin.

[178] A. Lafond, L. Choubrac, C. Guillot-Deudon, P. Deniard, S. Jobic, Crystal Structures of Photovoltaic Chalcogenides, an Intricate Puzzle to Solve: the Cases of CIGSe and CZTS Materials, Zeitschrift für anorganische und allgemeine Chemie, 638 (2012) 2571-2577.

[179] J.J. Scragg, T. Ericson, T. Kubart, M. Edoff, C. Platzer-Björkman, Chemical Insights into the Instability of Cu_2ZnSnS_4 Films during Annealing, Chemistry of Materials, 23 (2011) 4625-4633.

[180] V. Kosyak, N.B.M. Amiri, A.V. Postnikov, M.A. Scarpulla, Model of native point defect equilibrium in Cu_2ZnSnS_4 and application to one-zone annealing, Journal of Applied Physics, 114 (2013) 124501.

[181] W. Shockley, H.J. Queisser, Detailed Balance Limit of Efficiency of p-n Junction Solar Cells, Journal of Applied Physics, 32 (1961) 510.

[182] J. Krustok, T. Raadik, M. Grossberg, S. Giraldo, M. Neuschitzer, S. López-Marino, E. Saucedo, Temperature dependent electroreflectance study of $Cu_2ZnSnSe_4$ solar cells, Materials Science in Semiconductor Processing, 39 (2015) 251-254.

[183] S. Fiechter, M. Martinez, G. Schmidt, W. Henrion, Y. Tomm, Phase relations and optical properties of semiconducting ternary sulfides in the system Cu–Sn–S, Journal of Physics and Chemistry of Solids, 64 (2003) 1859-1862.

[184] P.A. Fernandes, P.M.P. Salomé, A.F.d. Cunha, A study of ternary Cu_2SnS_3 and Cu_3SnS_4 thin films prepared by sulfurizing stacked metal precursors, Journal of Physics D: Applied Physics, 43 (2010) 215403.

[185] D.M. Berg, R. Djemour, L. Gütay, S. Siebentritt, P.J. Dale, X. Fontane, V. Izquierdo-Roca, A. Pérez-Rodriguez, Raman analysis of monoclinic Cu_2SnS_3 thin films, Applied Physics Letters, 100 (2012) 192103.

[186] L.L. Baranowski, P. Zawadzki, S. Christensen, D. Nordlund, S. Lany, A.C. Tamboli, L. Gedvilas, D.S. Ginley, W. Tumas, E.S. Toberer, A. Zakutayev, Control of Doping in Cu_2SnS_3 through Defects and Alloying, Chemistry of Materials, 26 (2014) 4951-4959.

[187] M. Bouaziz, J. Ouerfelli, M. Amlouk, S. Belgacem, Structural and optical properties of Cu_3SnS_4 sprayed thin films, physica status solidi (a), 204 (2007) 3354-3360.

[188] V.A. Kovalenker, Kuramite, Cu_3SnS_4, a new mineral of the stannite group, International Geology Review, 23 (2010) 365-370.

[189] V.M. Dzhagan, A.P. Litvinchuk, M. Kruszynska, J. Kolny-Olesiak, M.Y. Valakh, D.R.T. Zahn, Raman Scattering Study of Cu_3SnS_4 Colloidal Nanocrystals, The Journal of Physical Chemistry C, 118 (2014) 27554-27558.

[190] X.-a. Chen, H. Wada, A. Sato, M. Mieno, Synthesis, Electrical Conductivity, and Crystal Structure of $Cu_4Sn_7S_{16}$ and Structure Refinement of Cu_2SnS_3, Journal of Solid State Chemistry, 139 (1998) 144-151.

[191] Y. Ren, J.J. Scragg, T. Ericson, T. Kubart, C. Platzer-Björkman, Reactively sputtered films in the Cu_xS–ZnS–SnS_y system: From metastability to equilibrium, Thin Solid Films, 582 (2015) 208-214.

[192] S.A. Vanalakar, G.L. Agawane, S.W. Shin, H.S. Yang, P.S. Patil, J.Y. Kim, J.H. Kim, Non-vacuum mechanochemical route to the synthesis of Cu_2SnS_3 nano-ink for solar cell applications, Acta Materialia, 85 (2015) 314-321.

[193] Y. Dong, J. He, L. Sun, Y. Chen, P. Yang, J. Chu, Effect of sulfurization temperature on properties of Cu2SnS3 thin films and solar cells prepared by sulfurization of stacked metallic precursors, Materials Science in Semiconductor Processing, 38 (2015) 171-176.

[194] A. Zakutayev, L.L. Baranowski, A.W. Welch, C.A. Wolden, E.S. Toberer, Comparison of Cu_2SnS_3 and $CuSbS_2$ as potential solar cell absorbers, in: Photovoltaic Specialist Conference (PVSC), 2014 IEEE 40th, 2014, pp. 2436-2438.

[195] L.L. Baranowski, K. McLaughlin, P. Zawadzki, S. Lany, A. Norman, H. Hempel, R. Eichberger, T. Unold, E.S. Toberer, A. Zakutayev, Effects of disorder on carrier transport in Cu_2SnS_3, Physical Review Applied, 4 (2015) 044017.

[196] A. Fairbrother, V. Izquierdo-Roca, X. Fontané, M. Ibáñez, A. Cabot, E. Saucedo, A. Pérez-Rodríguez, ZnS grain size effects on near-resonant Raman scattering: optical non-destructive grain size estimation, CrystEngComm, 16 (2014) 4120-4125.

[197] S. Sato, H. Sumi, G. Shi, M. Sugiyama, Investigation of the sulfurization process of Cu_2SnS_3 thin films and estimation of band offsets of Cu_2SnS_3-related solar cell structure, physica status solidi (c), 12 (2015) 757-760.

[198] S. Bourdais, C. Choné, B. Delatouche, A. Jacob, G. Larramona, C. Moisan, A. Lafond, F. Donatini, G. Rey, S. Siebentritt, A. Walsh, G. Dennler, Is the Cu/Zn Disorder the Main Culprit for the Voltage Deficit in Kesterite Solar Cells?, Advanced Energy Materials, (2016) 1502276.

[199] J.M. Burst, J.N. Duenow, D.S. Albin, E. Colegrove, M.O. Reese, J.A. Aguiar, C.-S. Jiang, M. Patel, M.M. Al-Jassim, D. Kuciauskas, CdTe solar cells with open-circuit voltage breaking the 1 V barrier, Nature Energy, 1 (2016) 16015.

[200] E. Garcia-Llamas, J.M. Merino, R. Serna, X. Fontané, I.A. Victorov, A. Pérez-Rodríguez, M. León, I.V. Bodnar, V. Izquierdo-Roca, R. Caballero, Wide band-gap tuning $Cu_2ZnSn_{1-x}Ge_xS_4$ single crystals: Optical and vibrational properties, Solar Energy Materials and Solar Cells, (2015) In press.

[201] S. Levcenco, D. Dumcenco, Y. Wang, Y. Huang, C.-H. Ho, E. Arushanov, V. Tezlevan, K. Tiong, Influence of anionic substitution on the electrolyte electroreflectance study of band edge transitions in single crystal $Cu_2ZnSn(S_xSe_{1-x})_4$ solid solutions, Optical Materials, 34 (2012) 1362-1365.

[202] A. Lafond, L. Choubrac, C. Guillot-Deudon, P. Fertey, M. Evain, S. Jobic, X-ray resonant single-crystal diffraction technique, a powerful tool to investigate the kesterite structure of the photovoltaic Cu_2ZnSnS_4 compound, Acta Crystallographica Section B: Structural Science, Crystal Engineering and Materials, 70 (2014) 390-394.

[203] D. Dumcenco, Y.-S. Huang, The vibrational properties study of kesterite Cu_2ZnSnS_4 single crystals by using polarization dependent Raman spectroscopy, Optical Materials, 35 (2013) 419-425.

[204] J.V. Li, D. Kuciauskas, M.R. Young, I.L. Repins, Effects of sodium incorporation in Co-evaporated $Cu_2ZnSnSe_4$ thin-film solar cells, Applied Physics Letters, 102 (2013) 163905.

[205] T. Schwarz, O. Cojocaru-Mirédin, P. Choi, M. Mousel, A. Redinger, S. Siebentritt, D. Raabe, Atom probe study of $Cu_2ZnSnSe_4$ thin-films prepared by co-evaporation and post-deposition annealing, Applied Physics Letters, 102 (2013) 042101.

[206] C.M. Sutter-Fella, J.A. Stückelberger, H. Hagendorfer, F. La Mattina, L. Kranz, S. Nishiwaki, A.R. Uhl, Y.E. Romanyuk, A.N. Tiwari, Sodium Assisted Sintering of Chalcogenides and Its Application to Solution Processed $Cu_2ZnSn(S,Se)_4$ Thin Film Solar Cells, Chemistry of Materials, 26 (2014) 1420-1425.

[207] B.T. Gershon, Y.S. Lee, R. Mankad, O. Gunawan, T. Gokmen, D. Bishop, B. McCandless, S. Guha, The impact of sodium on the sub-bandgap states in CZTSe and CZTS, Applied Physics Letters, 106 (2015) 123905.

[208] S. Giraldo, M. Neuschitzer, T. Thersleff, S. López-Marino, Y. Sánchez, H. Xie, M. Colina, M. Placidi, P. Pistor, V. Izquierdo-Roca, K. Leifer, A. Pérez-Rodríguez, E. Saucedo, Large Efficiency Improvement in $Cu_2ZnSnSe_4$ Solar Cells by Introducing a Superficial Ge Nanolayer, Advanced Energy Materials, 5 (2015) 1501070.

[209] M. Grossberg, K. Timmo, T. Raadik, E. Kärber, V. Mikli, J. Krustok, Study of structural and optoelectronic properties of $Cu_2Zn(Sn_{1-x}Ge_x)Se_4$ (x=0 to 1) alloy compounds, Thin Solid Films, 582 (2015) 176-179.

[210] T. Gershon, Y.S. Lee, P. Antunez, R. Mankad, S. Singh, D. Bishop, O. Gunawan, M. Hopstaken, R. Haight, Photovoltaic Materials and Devices Based on the Alloyed Kesterite Absorber $(Ag_xCu_{1-x})_2ZnSnSe_4$, Advanced Energy Materials, (2016) 1502468.

[211] S. Chen, A. Walsh, Y. Luo, J.-H. Yang, X.G. Gong, S.-H. Wei, Wurtzite-derived polytypes of kesterite and stannite quaternary chalcogenide semiconductors, Physical Review B, 82 (2010) 159904.

[212] L. Yu, S. Lany, R. Kykyneshi, V. Jieratum, R. Ravichandran, B. Pelatt, E. Altschul, H.A.S. Platt, J.F. Wager, D.A. Keszler, A. Zunger, Iron Chalcogenide Photovoltaic Absorbers, Advanced Energy Materials, 1 (2011) 748-753.